A Hybrid Plasmon-Solid-State Single-Photon Source

Martin Tobias Zeitlmair

München 2020

A Hybrid Plasmon-Solid-State Single-Photon Source

Martin Tobias Zeitlmair

Dissertation
an der Fakultät für Physik
der Ludwig–Maximilians–Universität
München

vorgelegt von
Martin Tobias Zeitlmair
aus Schrobenhausen

München, den 03.12.2020

Abstract

While the 20th century was shaped by the onset of information technology and the start of the Information Age, the 21th century might see a fundamental shift in information processing based on quantum science. In this regard, a main concept for future implementations of quantum information science is the encoding of information in single quanta of light, called photons. For this, the efficient and on-demand creation of single photons with high probability is essential.

This thesis investigates one approach for a hybrid single-photon source based on two components: A nonclassical light source, which emits single photons on demand and a nanophotonic or nanoplasmonic structure, which facilitates efficient collection of light. For creating single quanta of light, colour centers in nanodiamonds were employed. Due to their host matrix being a wide-bandgap semiconductor, localized optical states within the band gap are well shielded against thermal excitations, which allows for operation as a single-photon emitter at ambient temperatures. Additionally, due to their solid-state nature, they can be easily positioned and employed in other structures.

The second component for a single-photon source is a suitable nanostructure. For this thesis, plasmonic ring resonators were chosen, which promise strong redirection of light. Three main steps were taken for creating such structures: First, the envisioned system was analytically modeled and numerically simulated to determine optimized design parameters and investigate additional effects. After that, the structures were created by nanofabrication techniques. As the created systems are highly sensitive to fabrication deviations and uncertainties, strong emphasis was put on optimizing the single fabrication steps. Additionally, the envisioned hybrid single-photon source was realized by deterministically positioning diamond nanocrystals in the center of the metallic ring resonators using an atomic force microscopy based positioning technique. In a last step, the assembled light source was investigated experimentally. This involved the realization of an optical photoluminescence setup, its calibration and optimization for a tailored investigation of the emission properties of nanoscale light sources.

The results of the experimental investigation confirm the striking increase in collection efficiency expected by metallic ring resonators, especially when using collection optics with lower numerical aperture. Here, the amount of light being collected is boosted to a manifold compared to the quantum emitter without the plasmonic structure, which facilitates the collection of single photons with high probability. The investigated metallic bullseye resonator structures, therefore, enable the creation of robust and efficient on-demand single-photon sources. Due to their working principle in transmission, compact and cost-effective sources can be created. Additionally, the hybrid approach allows for utilizing other quantum emitters if they are better suited for the task at hand.

Zusammenfassung

Das 20. Jahrhundert war vom Einzug der elektronischen Informationstechnik geprägt, die das moderne Informationszeitalter einläutete. Im 21. Jahrhundert könnte ein umfassender Wandel hin zur quantenbasierten Informationsverarbeitung erfolgen, die vollkommen neuartige Möglichkeiten in der Informationstechnik bietet. Grundlegende Arbeitsweisen dieser neuartigen Technik basieren oftmals darauf, Information in einzelnen Lichtteilchen, den sogenannten Photonen, zu kodieren. Hieraus ergibt sich der Bedarf an neuartigen Lichtquellen mit hoher Präzision und Verlässlichkeit.

Die vorliegende Arbeit beschäftigt sich mit einem Ansatz zur Realisierung solch einer neuartigen Einzelphotonenquelle mittels eines hybriden Konzeptes, der aus zwei Komponenten besteht: Zum einen wird eine nichtklassische Lichtquelle benötigt, die Lichtteilchen nach Bedarf emittieren kann. Zum anderen werden nanophotonische oder nanoplasmonische Strukturen benötigt, um die Aufsammeleffizienz steigern. Als Quelle für Einzelphotonen wurden im Zuge dieser Arbeit Defektzentren in Diamant verwendet. Diese zeichnen sich dadurch aus, dass sie durch die große Bandlücke von Diamant thermisch isoliert sind, wodurch sie auch bei Raumtemperatur funktionieren. Außerdem können sie als Festkörperstrukturen einfach in andere Systeme integriert werden.

Neben den nichtklassischen Lichtquellen werden auch passende Nanobauteile benötigt. Für diese Arbeit wurde der Ansatz von plasmonischen Ringstrukturen gewählt, der mit Hilfe von drei Schritten realisiert wurde: Zuerst wurden optimierte Strukturparameter durch Modellierung und numerische Simulationen ermittelt. Zur Realisierung der Strukturen wurden Top-Down Techniken zur Nanofabrikation eingesetzt. Da die nanoplasmonischen Strukturen sehr sensitiv auf Fabrikationsungenauigkeiten sind, wurden hierbei die einzelnen Schritte des Fabrikationsprozesses für ein bestmögliches Ergebnis optimiert. Das finale hybride System, bestehend aus Nanodiamanten und plasmonischen Ringstrukturen, wurde anschließend mit Hilfe eines Rasterkraftmikroskop-basierten Verfahrens zur präzisen Platzierung von Nanostrukturen verwirklicht. Die experimentelle Untersuchung dieses hybriden Systems erfolgte mittels optischer Photolumineszenzmikroskopie. Hierfür wurde ein speziell konstruierter experimenteller Aufbau zur Vermessung der Emissionseigenschaften realisiert und optimiert.

Die Messungen zeigten eine beachtliche Verbesserung der Aufsammeleffizienz durch Anwendung der plasmonischen Ringresonatoren im Vergleich zu einer Lichtquelle ohne zusätzliche Nanostruktur. Speziell für optische Systeme mit niedriger Aufsammeleffizienz bedeutet dies eine Verbesserung der Lichtausbeute um mehrere Größenordnungen. Dies verdeutlicht, dass die untersuchte plasmonische Ringstruktur, die durch ihre Verwendung in Transmission sehr kompakte Bauweisen ermöglicht, im besonderen Maße für die Verwirklichung von effizienten und kostengünstigen Einzelphotonenquellen geeignet ist. Durch den gewählten hybriden Ansatz ist es außerdem möglich, andere Arten von nichtklassischen Lichtquellen zu integrieren.

Contents

List of Figures

List of Tables

Chapter 1.

Quantum Information as a Game Changer: Creating Single Quanta of Light

In the future, quantum physics developed in the 20th century and especially quantum information technology could be classified as one of the disruptive technologies of the 21st century. Although originally an economical term, disruptivity describes a technological discontinuity, a revolution of technology instead of an evolutionary one. Historically, processing information was performed by natural systems and mechanical devices only. This changed in the 1950s with the appearance of computation machines and marked the beginning of classical information processing, where information could be stored and processed in binary form. Through the decades, the amount of information handled in this manner grew exponentially and lead to what is now called the *Information Age* [1]. In this context, to this day the fundamental unit of information is the *bit*, which has two defined states, e.g. high and low DC voltage levels or light and no light.

In contrast to this classical information processing, where data is represented strictly in a binary manner, quantum mechanics offers a fundamentally different way to represent information. Here, data can be stored in so-called *qubits* representing a two-state system, which can be zero or one, like a classical bit, but also a coherent superposition of both [2]. Various physical systems can be employed for creating qubit states like the spin of an electron or nucleus [3, 4], atoms in an optical lattice [5] or solid-state phase qubits formed by Josephson junctions [6, 7]. However, the probably most widely used one are the various properties of a single quanta of light, a single *photon*, where the two-state system can be formed by polarization, the number of photons as a Fock state or time-bin encoding [8, 9, 10].

A fundamental requirement for employing single photons as nonclassical carriers of information is their availability on demand and with well-defined physical properties. Ideally, they would have a distinct emission time and emission frequency to ensure that different single quanta of light are intrinsically indistinguishable from one another. For more complex quantum information applications, this indistinguishability should also be provided for photons emitted from different light sources.

Emitting single photons is a feat not possible with traditional light sources as their distribution of emitted photons over time adheres to statistical laws, which in turn make it impossible to obtain one single photon with certainty. Instead, they can be classified as *thermal light* sources or *coherent light* sources, resulting in *super-Poissonian* and *Poissonian* photon-detection statistics, respectively [8]. Thermal light is produced by the thermal motion of particles in matter, e.g. glow discharge in a plasma. The archetype of coherent light is

provided by stimulated emission in lasers. In the context of quantum information, they are often employed in pulsed operation for creating weak coherent pulses, which are then attenuated to a level, where on average less then one photon is emitted per pulse [11]. Still, for Poissonian statistics the number of photons in a pulse is not fixed but will vary. For some applications like quantum cryptography, special protocols like decoy-state QKD counteract this uncertainty, however, at the price of complicating the underlying protocol and thus the complexity on the experiment [12].

For real single-photon sources, *sub-Poissonian* photon statistics is needed, which cannot be described by classical electromagnetic theory [13]. While this type of light source was first demonstrated only in the 1970s by anti-correlation measurements [14], a variety of different types of single-photon emitters and sources were investigated in the last decades [15]. Apart from parametric processes and second-harmonic generation, for linear optical quantum information processing and quantum cryptography mainly sources based on fluorescence are employed, e.g. single atoms in a trap [16], semiconductor structures like quantum dots [17], organic dye molecules [18] or dopant sites in a solid-state host material [19, 20].

The main aim of this thesis was creating efficient, simple single-photon sources based on single dopant sites in diamond, so-called *defect centers* or *colour centers* in diamond. With their ability to emit single photons at room temperature and their sturdy solid-state composition, they are ideal for creating easy-to-use and robust sources. In this context, a complete single-photon source requires two components: the quantum emitter acting as a nonclassical light source and a nanophotonic or nanoplasmonic device to enhance and channel the collection of the emitter. Both single components and their combined behavior were investigated in the course of this thesis. For this, several key steps were necessary: Firstly, nanoscale structures were created by means of electron-beam lithography. For optical investigations of both the employed colour centers in diamond and the created structures, an optical photoluminescence setup was constructed. Additionally, the envisioned hybrid systems were modeled and simulated. In a final step, the quantum emitter was coupled to the nanostructure and the properties of the resulting final light source were investigated.

In the following chapters, the different aspects of this work are presented. The next chapter 2 presents the basic theory of electromagnetic waves and their interaction with matter. In particular, the interplay of light and a metallic surface in form of a plasmonic wave is illustrated. Chapter 3 deals with the simulation and modeling of dielectric waveguiding structures and concentric plasmonic ring structures using both numerical as well as analytical models. In the subsequent chapter 4, the main experimental techniques are presented, in particular the optical photoluminescence experiments and their evaluation. Chapter 5 illustrates the principal properties of colour centers in diamond by example of two different systems, the *nitrogen-vacancy* and the *silicon-vacancy* center, which were both employed for this thesis. The main results of experiments with hybrid systems consisting of bullseye resonator structures and colour centers in a nanodiamond are presented thereafter in chapter 6 with emphasis on both the findings and the conclusions drawn thereof. Subsequently, chapter 7 summarizes the main results of this thesis and provides an outlook for possible further improvements and experimental studies. Finally, the appendix provides details about the realization of the employed hybrid structures by describing both the creation of nanophotonic and -plasmonic structures by state-of-the-art fabrication techniques and the deterministic placement of nanocrystals on fabricated structures with high accuracy.

Chapter 2.

Theory of Light and Matter

The foundation for a reasonable physical description of a system is a sound and consistent theory. Therefore, this chapter provides a collection of the main theoretical aspects relevant for this work, which are later on used to predict, describe and interpret the experimental results. As nearly all the experiments involve electromagnetic radiation and its interaction with physical matter, this chapter starts with a short introduction to the omnipresent *Maxwell's Equations* and then introduces two different types of interaction between light and matter: the guiding of light by dielectric structures, in particular planar waveguides, and coupling light to an interface of a metallic and a dielectric surface, which is the field of plasmonics. Naturally, such a presentation in the framework of a thesis cannot be exhaustive and illustrates the main concepts only. The interested reader may find further and more detailed information in the mentioned sources.

2.1. Maxwell's Equations and Basic Properties of Light and Matter

The classical description of phenomena involving electromagnetic (EM) waves and their interaction with the surrounding medium is provided by a set of equations called the *Maxwell's equations*, named after James Clerk Maxwell, who derived them in the mid-1800s. Even though many of the underlying physical principles were already known by that time, the idea that light is a phenomenon involving both an *electric field* $\mathcal{E}$ and a *magnetic field* $\mathcal{H}$, which are themselves linked together, was revolutionary at that time. In differential form, the Maxwell equations are (see also e.g. [8])

$$
\begin{aligned}
\nabla \cdot \mathcal{D} &= \varrho \\
\nabla \cdot \mathcal{B} &= 0 \\
\nabla \times \mathcal{E} &= -\frac{\partial \mathcal{B}}{\partial t} \\
\nabla \times \mathcal{H} &= \boldsymbol{j} + \frac{\partial \mathcal{D}}{\partial t}
\end{aligned}
\tag{2.1}
$$

Here, ϱ is the *free charge density* and $\boldsymbol{j}$ represents the *free current density*. Two other, related fields were used in the equations, namely the *electric displacement* $\mathcal{D}$ and the *magnetic flux*

density $\boldsymbol{\mathcal{B}}$. Here, the electric displacement describes the response of a medium to the presence of an electromagnetic wave, which is described by the *polarization* $\boldsymbol{\mathcal{P}}$. One finds that

$$\boldsymbol{\mathcal{D}} = \epsilon_0 \boldsymbol{\mathcal{E}} + \boldsymbol{\mathcal{P}} \tag{2.2}$$

with ϵ_0 being the *electric permittivity of free space*. For isotropic media, the relationship between $\boldsymbol{\mathcal{E}}$ and $\boldsymbol{\mathcal{P}}$ can be expressed as

$$\boldsymbol{\mathcal{P}} = \epsilon_0 \chi \boldsymbol{\mathcal{E}} \tag{2.3}$$

with the *electric susceptibility* χ. This only describes the linear dependence for small electric field strengths, which can be expanded to higher orders for nonlinear effects. However, many scenarios in linear optics and all the cases dealt with in this thesis can be well approximated by the linear correlation. Defining the *relative permittivity* of the medium ϵ_r as $\epsilon_r = 1 + \chi$, it follows that

$$\boldsymbol{\mathcal{D}} = \epsilon_0 \epsilon_r \boldsymbol{\mathcal{P}} \tag{2.4}$$

In general, ϵ_r is a complex function with $\epsilon_r = \epsilon_1 + i\epsilon_2$, where the real part ϵ_1 and the imaginary part ϵ_2 are related to the physical phenomena of diffraction and absorption, respectively.

Similar to the relations for the electric field, the fields describing magnetic fields are linked too. Here, on finds that the response of the medium to the presence of an electromagnetic wave can be described by a *magnetization* $\boldsymbol{\mathcal{M}}$ as

$$\boldsymbol{\mathcal{H}} = \frac{1}{\mu_0} \boldsymbol{\mathcal{B}} - \boldsymbol{\mathcal{M}} \tag{2.5}$$

In this context, μ_0 is the *magnetic permeability of the vacuum*. Again assuming an isotropic medium, the magnetization can be defined as

$$\boldsymbol{\mathcal{M}} = \chi_M \boldsymbol{\mathcal{H}} \tag{2.6}$$

with the *magnetic susceptibility* χ_M. Similar to the electric case, one can define a *relative magnetic permeability* μ_r as $\mu_r = 1 + \chi_M$, which leads to

$$\boldsymbol{\mathcal{B}} = \mu_0 \mu_r \boldsymbol{\mathcal{H}} \tag{2.7}$$

Typically, the magnetic response of the system described by χ_M is much weaker than the electric response. Because of this, one can neglect the relative magnetic permeability ($\mu_r = 1$). In this case, the magnetic field and the magnetic flux density can be directly linked via the magnetic permeability as

$$\boldsymbol{\mathcal{B}} = \mu_0 \boldsymbol{\mathcal{H}} \tag{2.8}$$

From these basic equations describing the interaction of electromagnetic fields with its surrounding, the following wave equations can be derived [8]

$$
\begin{aligned}
\nabla \times (\nabla \times \boldsymbol{\mathcal{E}}) + \frac{\epsilon_r}{c^2}\frac{\partial^2}{\partial t^2}\boldsymbol{\mathcal{E}} &= 0 \\
\nabla \times \left(\frac{1}{\epsilon_r}\nabla \times \boldsymbol{\mathcal{H}}\right) + \frac{1}{c^2}\frac{\partial^2}{\partial t^2}\boldsymbol{\mathcal{H}} &= 0
\end{aligned}
\tag{2.9}
$$

Here, $c = c_0/\sqrt{\epsilon_r \mu_r}$ is the propagation speed of the electromagnetic wave and $c_0 = 1/\sqrt{\epsilon_0 \mu_0}$ is the speed of light in vacuum. The proportionality factor $n = c_0/c$ is called the *refractive index* and is a well-known figure for describing the influence of a material on the propagation of an electromagnetic wave.

In complex form, the refractive index can be written as $n = n_r + i \cdot n_i$ and incorporates both information about the speed, with which an EM wave propagates through a medium, as n_r and information about the absorption strength of the material as n_i. These two numbers n_r and n_i are, therefore, sufficient to fully describe the (linear) optical properties of a material for a specific wavelength. For many materials, the dispersion of the complex refractive index is published and can be directly employed for numerical simulations in e.g. dispersive models for metals, which are described in the subsequent section 2.3.1.

2.2. Photonic Waveguiding Structures

The basic wave equations in 2.9 describe the propagation of an electromagnetic wave in an arbitrary material. In many applications, the goal of shaping the material composition is to guide an EM wave and shape its mode structure. For this, typically dielectric waveguiding structures, for example optical fibers, are used. Their basic working principle is based on a difference in the refractive index and the boundary conditions for electromagnetic waves at a dielectric interface.

Imagine an interface between two materials 1 and 2. If an electromagnetic wave interacts with this interface, its electric field components have to abide the interface conditions

$$
\begin{aligned}
\hat{\boldsymbol{e}}_n \times (\boldsymbol{\mathcal{E}}_2 - \boldsymbol{\mathcal{E}}_1) &= 0 \\
\hat{\boldsymbol{e}}_n \cdot (\boldsymbol{\mathcal{D}}_2 - \boldsymbol{\mathcal{D}}_1) &= \varrho_s
\end{aligned}
\tag{2.10}
$$

Here, $\hat{\boldsymbol{e}}_n$ is the normal vector to the interface and ϱ_s is the surface charge density. A fundamental consequence from these interface conditions is the fact that the electric field component normal to the interface exhibits a discontinuity, which scales with the refractive indices of the two materials. The same effect occurs for the parallel magnetic field components [8].

The law of refraction and the interface conditions are the main inputs to obtain the shape of bound modes in dielectric waveguiding structures. They are typically formed by surrounding a material with high refractive index with a second material with lower refractive index. By using the spatial information about the refractive index within the wave equations, the electromagnetic field distribution, here called the *mode structure*, can be calculated. However,

analytical solutions for such eigenmode problems can be found only for systems with high symmetry, e.g. optical fibers with cylindrical symmetry or slab waveguides [21].

(a) Eigenmode TE0

(b) cuts through (a)

(c) Eigenmode TM0

(d) cuts through (c)
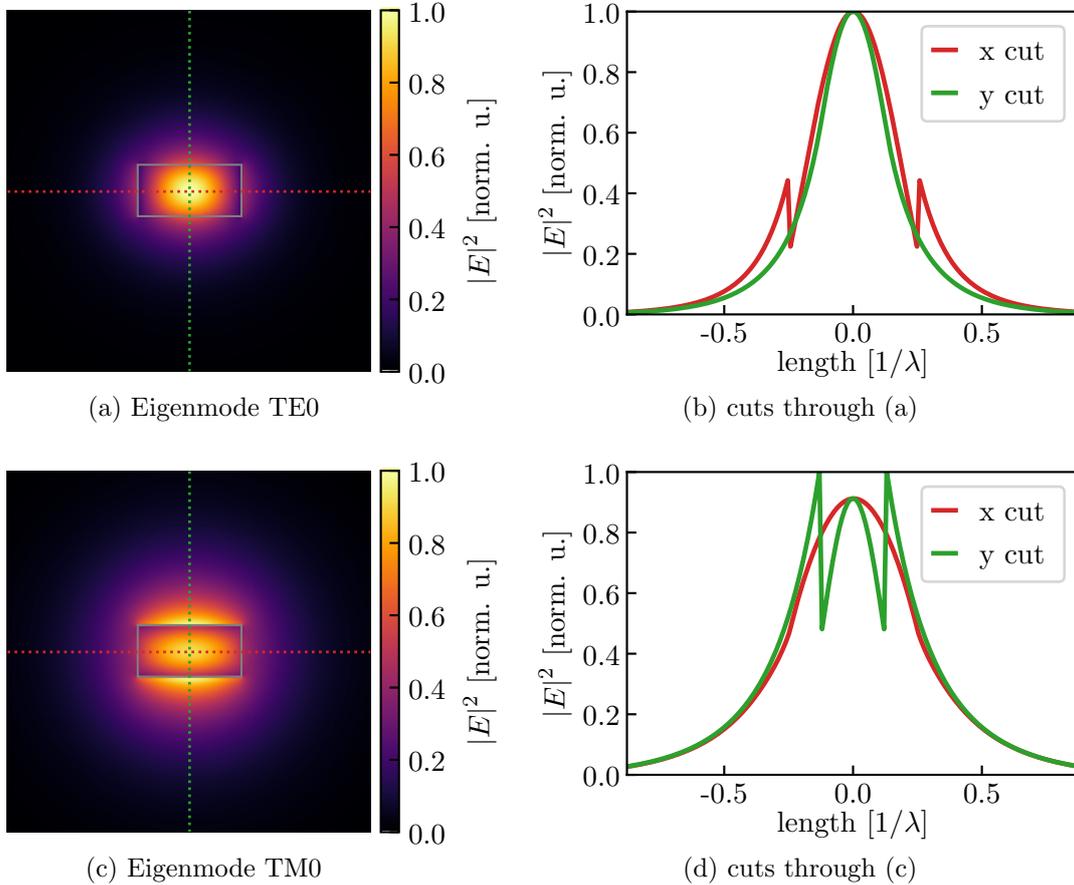
Figure 2.1.: The typical mode structure of a dielectric strip waveguide with a width of $0.5\,\lambda$ and a height of $0.25\,\lambda$. The waveguide has a refractive index of $n = 1.5$ and is surrounded by air ($n = 1$). (a) and (b): Fundamental transverse-electric (TE) mode structure and corresponding horizontal and vertical cuts. A discontinuity of the electric field can be seen for the horizontal direction while the vertical direction is continuous. (c) and (d) illustrate the same effect for the fundamental transverse-magnetic (TM) mode, where the discontinuity occurs in vertical direction.

Even for the very simple case of a straight waveguide with rectangular cross-section, which is a typical form for planar waveguides, approximations are necessary for an analytical solution [22]. Section 3.1.1 discusses numerical methods for calculating eigenmodes for waveguides with arbitrary geometrical cross-sections. A very simple example for the typical mode structure is given in figure 2.1, which shows the electric field intensity for the two fundamental modes of a rectangular strip waveguide. Here, the direction of propagation points into the image plane. The width of the waveguide is half of the assumed wavelength λ and the height amounts to a quarter of λ. For both eigenmodes, horizontal and vertical cuts illustrating the course of the electric field strength through the center of the waveguide are shown.

Similar to the case of *Hermite-Gaussian* modes, which are also called *transverse-electromagnetic* (TEM) modes as both the electric and magnetic field are strictly perpendicular to the direction of propagation, the bound modes of a waveguide can be classified as (quasi) *transverse electric* (TE) modes (or H modes) and (quasi) *transverse magnetic* (TM) modes (or V modes). For TE modes (TM modes), the electric (magnetic) field is perpendicular to the direction of propagation. Note that strictly speaking, only in the case of a slab waveguide with one dimensional mode confinement, pure TE and TM modes exist [23].

For the two modes in figure 2.1, the discontinuity imposed by the interface conditions from equations 2.10 are clearly visible: For a predominately horizontally polarized TE mode, the electric field intensity, which is mainly oriented perpendicular with respect to the sides of the waveguides, shows a sharp increase in intensity before decaying into the lower refractive index parts. For the mainly vertically polarized TM mode, the corresponding effect occurs with a discontinuity of the field intensity in vertical direction. This discontinuity behavior can play a pivotal role in creating specially designed modes like those of dielectric slot waveguides, which are presented in detail in section 3.2.

2.3. Plasmonics

Plasmonics can be described as the study of the interaction between an electromagnetic wave and a metallic material. The resulting phenomena, which appear due to this interaction, have been known long before a theoretical framework, now known as *plasmonics*, was developed. In essence, plasmonics describes the effect of collective plasma oscillations in a metal [24]. As this collective movement is of bosonic nature and quantized, the quasi-particle is called a *plasmon*. Nowadays, plasmonics is a very active field of study as it promises a novel approach for many questions in nanophysics and offers a way to confine light to spaces much smaller than limited by the classical refraction limit [25, 26].

This section presents some key aspects of plasmonics, in particular the interaction of light and metals in the form of *surface plasmon polaritons* (SPPs). For this, first a theoretical model for describing metallic materials is presented. This model is also of great importance for numerical simulation techniques (compare chapter 3 for further information, which presents simulations of nanophotonic and -plasmonic devices). After that, the main concepts of surface plasmon polaritons are presented, which are used for calculating key figures of SPPs in different materials.

2.3.1. Theory of Metals: The Lorentz-Drude Model

By the late 1800s, many basic laws of electrical transport in metals like *Ohm's law* were derived and experimentally confirmed. However, an underlying theory for the rather peculiar behavior of metals was still missing. This changed in 1900, when Paul Drude published his paper *Zur Elektronentheorie der Metalle* (On the theory of electrons in metals). In there, a purely classical model was described assuming an ideal free electron gas, which propagates in a matrix of fixed positive nuclei. While propagating e.g. due to an external electric field, the electrons loose kinetic energy due to scattering at the nuclei, which themselves start to

oscillate. By analyzing this kinetic motion of the electrons and the nuclei, Paul Drude could derive equations for the electric permittivity $\varepsilon(\omega)$ of metals (compare also 2.1), which can be written as

$$\varepsilon_r(\omega) = 1 - \frac{\omega_p^2}{\omega^2 + i\gamma_D(\omega)\omega} \quad \text{with} \quad \omega_p = \sqrt{\frac{ne^2}{\epsilon_0 m_e^*}} \tag{2.11}$$

Here, the two important parameters are the factor $\gamma_D(\omega)$, which characterizes the damping of the nuclei oscillation, and the *plasma frequency* ω_p, which depends on the density n of electrons in the metal and their effective mass m_e^*. Below the plasma frequency, an impinging electromagnetic wave is subject to scattering and absorption, while the material seems transparent for frequencies above ω_p.

While the original model proposed by Paul Drude worked well for describing basic electron transport properties in metals like Ohm's law and absorption phenomena based on interband transitions, it incorporated some major assumptions like the electrons moving collectively and unbound from the nucleus in the presence of an electromagnetic wave and a constant electron velocity. These assumptions were later on dropped and more defined models were constructed. One major contribution to this was provided by Hendrick Antoon Lorentz in 1905, who took the Boltzmann distribution of the electron velocity into account as well as the binding of electrons to the atom nucleus (described by Lorentz oscillators). This lead to the generalized form of equation 2.11, which is often labeled the *Lorentz-Drude model* [27]:

$$\varepsilon_r(\omega) = 1 - \frac{\omega_p^2}{\omega^2 + i\gamma_D(\omega)\omega} + \sum_{j=1}^{K} \frac{f_j\omega_j^2}{\omega_j^2 - \omega^2 - i\gamma_j(\omega)\omega} \tag{2.12}$$

Equation 2.12 incorporates both the Drude contributions describing interband transitions as well as K additional oscillator terms, each with its own resonance frequency ω_j, damping factor γ_j and weighting factor f_j, which models additional resonances like intraband transitions. For example, the dispersion curves of gold and aluminium in figure 2.2, which are calculated from experimental data taken from [28], show such an additional resonance in the electric permittivity at about 800 nm for aluminium stemming from an interband transition, which can be modeled accurately by a Lorentz-Drude model [29].

In practical use, equation 2.12 is often used in a slightly modified way by defining a relative permittivity ϵ_∞ at infinite frequency, a convention in which many experimental results are published [28, 30].

2.3.2. Light at a Metal-Dielectric Interface

In general, plasmons come in two flavors: Bulk plasmons, which propagate through a metallic material and plasmonic effects at the interface between a metal and a dielectric material, e.g. air [25]. At such an interface, a joint state of light and matter can occur, which consists of the collective movement of the electron density on the metallic side and a propagating electromagnetic wave on the dielectric side, a so-called *polariton*. The combined effect of an
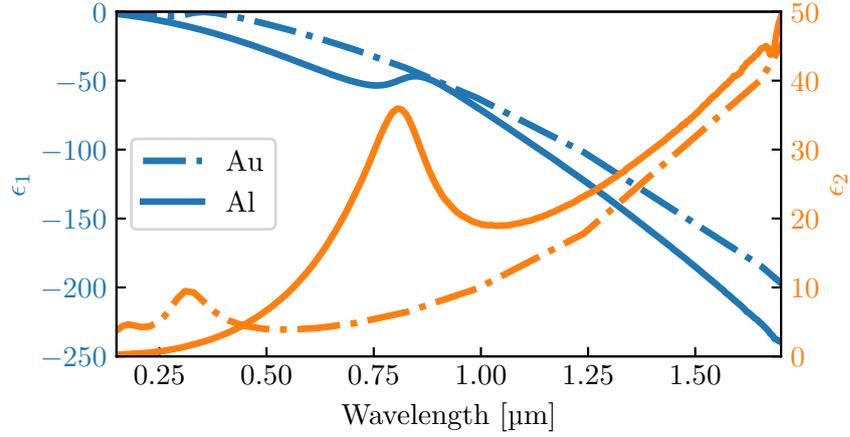
Figure 2.2.: Real part ϵ_1 and imaginary part ϵ_2 of the electric permittivity for gold and aluminium, data taken from [30].

EM wave propagating along this interface is then called the previously mentioned *surface plasmon polariton* (SPP).

Disperison curve of surface plasmon polaritons

The derivation of the dispersion relation for surface plasmon polaritons is a typical textbook calculation and, therefore, only the end result is presented here. For a metal-dielectric interface it is given by

$$k_{SP}(\omega) = k'_{SP} + i \cdot k''_{SP} = k_0(\omega) \sqrt{\frac{\epsilon_m(\omega)\epsilon_d(\omega)}{\epsilon_m(\omega) + \epsilon_d(\omega)}} = \frac{\omega}{c} \sqrt{\frac{\epsilon_m(\omega)\epsilon_d(\omega)}{\epsilon_m(\omega) + \epsilon_d(\omega)}} = \beta \qquad (2.13)$$

Here, $\epsilon_m = \epsilon'_m + i \cdot \epsilon''_m$ and $\epsilon_d = \epsilon'_d + i \cdot \epsilon''_d$ are the complex electric permittivity for the metal and the dielectric with $k_0 = \omega/c$ as the light wave number in vacuum and the corresponding wavelength $\lambda = 2\pi/k_0$. Often, this dispersion curve is simply called β. An in-depth derivation of this formula can be found in e.g. [25].

Inserting the complex definitions of ϵ into k_{SP}, one finds expressions for the real and imaginary parts of the wave vector k'_{SP} and k''_{SP}:

$$k'_{SP} = \frac{\omega}{c} \left(\frac{\epsilon'_m \cdot \epsilon_d}{\epsilon'_m + \epsilon_d} \right)^{1/2} \qquad (2.14)$$

$$k''_{SP} = \frac{\omega}{c} \left(\frac{\epsilon'_m \cdot \epsilon_d}{\epsilon'_m + \epsilon_d} \right)^{3/2} \cdot \frac{\epsilon''_m}{2(\epsilon'_m)^2} \qquad (2.15)$$
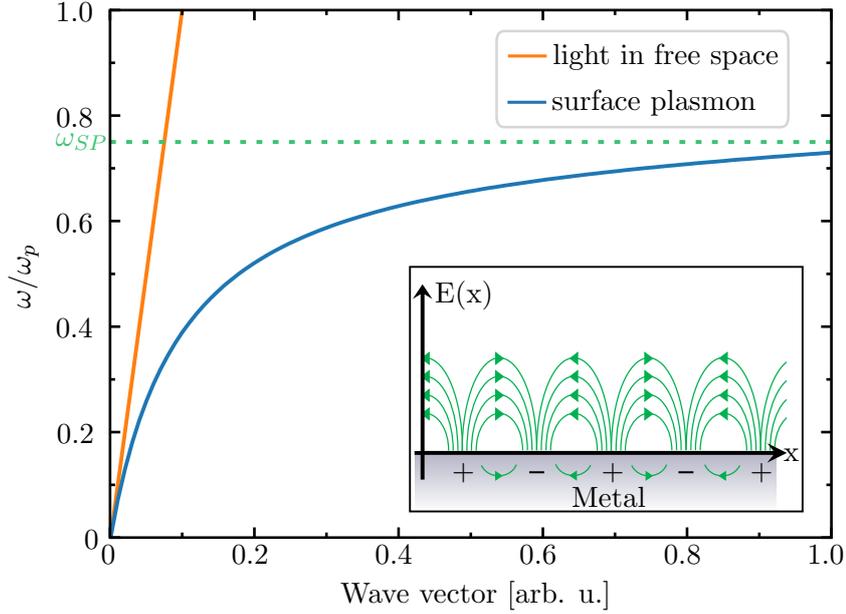
Figure 2.3.: The typical dispersion curve for surface plasmon polaritons (SPPs). Below the surface plasma frequency ω_{SP}, SPPs can propagate along the metal-dielectric interface. The insert illustrates the electric field distribution and charge oscillation for propagating SPPs.

The real part of the dispersion relation in equation 2.14 can be plotted relative to the dispersion of light in free space. Both are illustrated in figure 2.3. Light in free space follows the simple $k_{FS}(\omega) = (\omega \cdot n)/c$ relation with the refractive index n of the material as the slope, whereas the dispersion curve of SPPs converges towards the surface plasmon frequency ω_{SP}, which can be written as

$$\omega_{SP} = \omega_p \sqrt{\frac{1}{1 + \epsilon_d}} \tag{2.16}$$

and depends on both the material properties of the dielectric and the plasma frequency ω_p of the metal.

By comparing the two dispersion curves, the momentum mismatch between light propagating in free space and light bound to the metal-dielectric interface as an SPP is easily visible. For efficient incoupling of light to bound SPP modes at the interface, this momentum mismatch $\hbar \cdot (k_{SP} - k_{FS})$ has to be overcome. Besides prism-based approaches as in the *Kretschmann* and *Otto* configuration [25], also optical gratings provide the means for scattering light from free space modes to to SPP modes or vice versa. This mechanism is crucial for the working principle of plasmonic bullseye resonators, which are simulated and modeled in section 3.3.

Starting with the dispersion relation of surface plasmon polaritons in equation 2.13, different key figures like the propagation speed or oscillation wavelength, which characterize surface plasmon polaritons at a metal-dielectric interface, can be calculated. The main ones are

presented in the following and employed for comparing typical metals for their possible usage in plasmonic applications.

Wavelength and propagation length of surface plasmon polaritons

Two important constants can be calculated directly via β in equation 2.13, the SPP wavelength λ_{SPP} and the propagation length of surface plasmon polaritons L_{SPP}. They correspond to the real and imaginary parts of the dispersion relation $k_{SP}(\omega)$.

λ_{SPP} depends on the real part of β and is calculated via

$$\lambda_{SPP} = \frac{2\pi}{Re(\beta)} = \frac{2\pi}{k'_{SP}} \tag{2.17}$$

Similarly, L_{SPP} is defined as

$$L_{SPP} = \frac{1}{2Im(\beta)} = \frac{1}{2k''_{SP}} \tag{2.18}$$

and measures the propagation length of a SPP excitation before its intensity decays by a factor of $1/e$.

Group velocity calculation

An important and very influential parameter for the interference condition between different surface plasmon polariton excitations in nanoplasmonic devices like metallic gratings or bullseye resonators is the propagation speed of the surface plasmon polariton v_{SPP} along the interface. In particular, one has to distinguish between the phase velocity v_{ph} and the group velocity v_{gr}, which are classically defined as [31]

$$\begin{aligned} v_{ph} &= \frac{\omega}{k} \\ v_{gr} &= \frac{\partial \omega}{\partial k_{SP}(\omega)} = \frac{1}{\frac{\partial k}{\partial \omega}} = \frac{c}{n_{SP}(\lambda) - \lambda \frac{dn_{SP}}{d\lambda}} \end{aligned} \tag{2.19}$$

with ω being the light frequency and k being the wave vector. The group velocity v_{gr} can be calculated analytically from measured dispersion relations of metallic materials. Here, also an effective surface plasmon refractive index n_{SP} is introduced. This index can be calculated as

$$n_{SP} = \frac{k'_{SP}}{k_0} \tag{2.20}$$

Metals suitable for plasmonic applications

For plasmonic devices operating in the visible or near-infrared, typically two metals are considered: silver and gold. As discussed in section 6.1, an interesting alternative material is aluminium, which shows strong plasmonic resonances from the ultraviolet to the near-infrared. For a quantitative comparison of these materials, the presented figures of merit for SPP propagation can be calculated from published experimental data. For silver and aluminium, the data is taken from [30], the data used for gold is taken from [28].

The expected strength of a SPP resonance can already be qualitatively estimated by comparing the electrical conductivity σ of the different metals. For the three investigated metals, these are $\sigma_{Ag} = 6.30 \cdot 10^7$ S/m, $\sigma_{Au} = 4.11 \cdot 10^7$ S/m and $\sigma_{Al} = 3.77 \cdot 10^7$ S/m [32]. The electrical conductivity for silver is much larger as compared to the other two materials, which indicates higher electron mobility in the metal and, therefore, lower propagation losses of propagating electron-density waves. The propagation length for SPPs at a silver-dielectric interface should, therefore, be much larger than for gold or aluminium.

This assumption can be further validated by directly calculating the previously introduced performance parameters for SPPs from the published data. They can be employed for quantitatively classifying the suitability of a material for plasmonic applications. Figure 2.4 shows the calculated values for the propagation length L_{SPP}, the SPP wavelength λ_{SPP} and the group velocity v_{gr} for the three materials depending on the free space wavelength.

At first glance, a striking difference in the achievable propagation length between silver and the other two materials becomes visible. As already deduced from the much higher electrical conductivity for this material, its propagation length is nearly one order of magnitude larger than that of gold or aluminium. The latter two show similar achievable propagation lengths for the visible and near-infrared, while aluminium has high suitability in UV plasmonics.

For the emission wavelength of silicon-vacancy centers at 738 nm, which is the design wavelength for plasmonic bullseye resonators, the parameter values for the three investigated materials are summarized in table 2.1. When comparing gold and aluminium, the calculated values are comparable, which hints that both materials could be employed for plasmonic devices. An experimental investigation of those two materials for their possible usage in metallic bullseye resonator structures is presented in section 6.1.

	silver	gold	aluminium
SPP propagation length L_{SPP} [µm]	130.1	21.7	14.8
SPP wavelength λ_{SPP} [nm]	724	726	733
SPP group velocity v_{gr} [c]	0.939	0.942	0.977

Table 2.1.: Extracted surface plasmon polariton parameters from figure 2.4 for a free space wavelength of 738 nm.
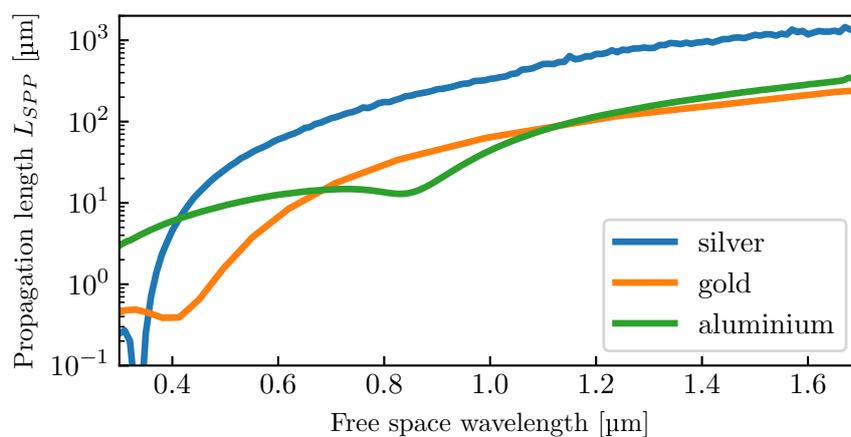
(a) Propagation length of SPPs for different metals
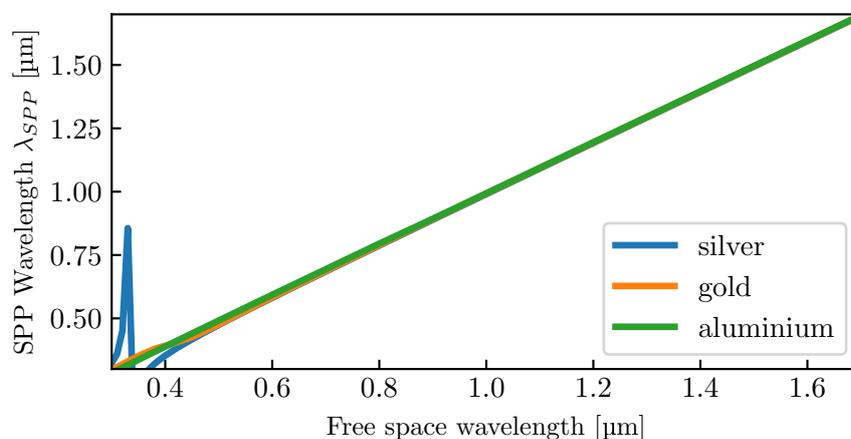
(b) SPP wavelength for different metals
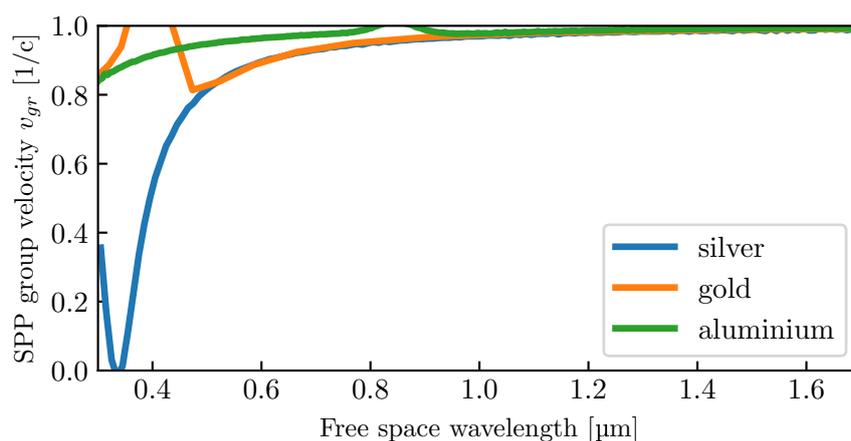
(c) Group velocity of propagating SPPs for different metals

Figure 2.4.: Comparison of (a) the propagation length, (b) the SPP wavelength and (c) the group velocity of surface plasmon polaritons (SPPs) propagating along a metal-air interface for silver (blue), gold (orange) and aluminium (green) calculated from experimental data.

Chapter 3.

Simulation and Modeling of Photonic and Plasmonic Nanodevices

The theory described in chapter 2 provides the basis for understanding nanooptical devices investigated and realized during this thesis. However, for a deeper understanding of real devices, their actual design philosophy and practical subtleties, a reduced view provided by assumptions and simplifications is not enough. For the purpose of designing photonic and plasmonic structures, other means of investigation have to be employed. Thus, simulations were performed and physical models of real devices were formed by means of numerical computation. In particular, simulations offer a comprehensive and useful tool for designing and understanding nanophotonic devices. In the context of optical devices, these simulation techniques are condensed in the term *computational electrodynamics* and describe the interaction of electromagnetic fields with their physical environment.

The computational methods of this technique are presented in the following sections and focus on two different types of simulation, each with its distinct simulation goal: finding the intrinsic eigenstates of an optical system, in this context called the *eigenmodes*, and analyzing the dynamics of real systems by directly simulating Maxwell's equations. The subsequent sections focus on two different approaches for efficient single-photon sources. First, a dielectric waveguide approach is discussed, which aims to create efficient single-photon emitters directly embedded in a planar waveguiding structure. The second approach uses plasmonics and aims to directly influence the emission characteristics of employed quantum emitters in order to maximize the collection efficiency of emitted light. Both approaches are investigated for their ability to harvest the light emitted by point-like quantum emitters and are analyzed in terms of practical limitations.

3.1. The Finite Element Method: Solving Maxwell's Equations in a Discrete Way

The classical physical explanation for the interaction of light and matter are summarized by the Maxwell's equations, which provide a complete classical description of electromagnetic phenomena. Described in detail in section 2.1, they form a set of differential equations, which need to be solved. For simple cases, which typically include a high degree of symmetry, this can be done analytically. However, the solution for more complex systems with phenomenological

effects like the dispersion properties of real materials cannot be expressed in a closed form. Instead, their solution has to be found numerically.

Numerical evaluation of differential equations like the Maxwell's equations, both in their differential as well as their integral form, are based on discretization. For electromagnetic simulations, this leads to dividing the investigated geometrical space into finite elements, often called the *mesh* [33]. For a complete description of this discretized space elements, it is essential to describe all relevant material properties of each chosen point, e.g. the refractive index, absorption properties or polarizability. As these properties vary with frequency, a dispersive description or approximation is necessary. One very often used dispersive model is the Lorentz-Drude model for metals, which is already described in section 2.3.1, or the *Sellmeier equation* for non-absorbing materials [34].

The remaining question is what kind of algorithm one uses for the meshed space. In general, two approaches are very common for electromagnetic problems: Either one wants to find the eigenstates or eigenmodes of an optical system or one wants to investigate the temporal dynamics of a chosen or given electromagnetic distribution. Both approaches are employed for this thesis and are shortly discussed in the following sections.

3.1.1. The Finite-Difference Eigenmode Method

The finite-difference eigenmode method is tailored towards a specific question: what is the eigenmode/eigenstate of an optical system if the geometrical parameters and the physical properties are given? This kind of question is typical for systems, which can guide electromagnetic waves like optical fibers or have resonance frequencies like radio antennas. In its essence, finite-difference eigenmode solvers start with a discretized geometrical space and assume a random distribution of the electromagnetic fields. Typically, this is done in two dimensions with the third being assumed infinite. Using Maxwell's equations, they then minimize the energy in the system, which corresponds with one eigenmode of the investigated structure. In mathematical terms, this procedure can be described as solving a linear algebraic equation. By repeating this process several times, all supported eigenmodes can be found [35].

Of particular importance for these kind of simulations is the type of boundary conditions on the edges of the investigated geometry. A typical example of such a boundary condition is a periodic one, which makes use of the Bloch theorem [36]. This type of simulation is especially useful for investigating repetitive crystal-like structures like photonic crystals [37]. The finite-difference eigenmode package employed in this thesis is called *MIT Photonic Bands* (MPB) [36] and specifically designed for investigating optical band properties of periodic structures. MPB is mainly chosen as the simulation package of choice for its scripting capability using the popular Python programming language and its open-source availability, which makes its usage free from licensing restrictions. The only drawback is the lack of non-periodic boundary conditions, which are necessary for analyzing single waveguiding structures like the dielectric slot waveguides investigated in section 3.2. However, this limitation can be circumvented by a *supercell* approach[34, 36]: The general idea for finding eigenmodes of single, isolated geometries like waveguiding structures is to increase the simulation space to such an extent, where the found bound modes have decayed before reaching the boundaries of the simulation.

3.1.2. The Finite-Difference Time-Domain Method

Apart from the search for supported eigenmodes of an optical system, very often the numerical investigation aims towards finding the response of the system to an external electromagnetic input. In most cases, this analysis is performed in the time domain and directly simulates the dynamics of the system. This *finite-difference time-domain* (FDTD) method is a major working horse for the investigation of optical phenomena at the micro- and nanoscale as it offers many advantages and feasibilities. In particular, for modeling optical devices at the nano- or microscale, these might be the freedom to investigate any desired geometry without further knowledge about the device response or the direct monitoring of the optical response of a system for the calculation of scattering, absorption or transmission/reflection properties. As mentioned earlier, the investigated geometry can be made up from arbitrary materials, as long as their optical properties are known and well approximated by dispersive models.

Basic Principle of FDTD simulations

The basic working principle of FDTD algorithms is based on discretized versions of Maxwell's equations, which act on a discrete grid of points representing the investigated geometry. For the direct numerical integration of partial differential equations like the Maxwell's equations, this can be achieved with the *Yee algorithm*. Figure 3.1 illustrates the basic geometrical setup for the numerical calculations.

(a) TE field   (b) TM field   (c) 3D Yee cell
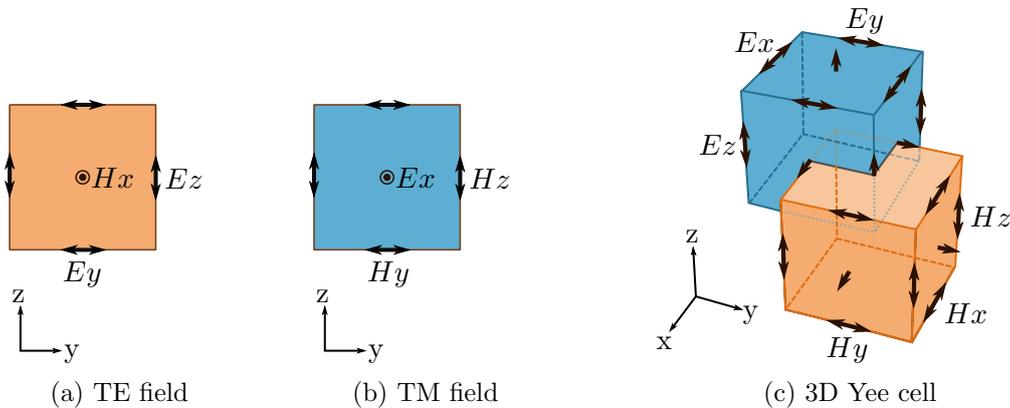
Figure 3.1.: Fundamental grid setup for FDTD simulations using the Yee algorithm for (a) transverse-electric (TE) and (b) transverse-magnetic (TM) fields. (c) shows the complete three-dimensional Yee cell.

In its essence, the Yee algorithm in computational electrodynamics divides the investigated space into a discrete grid of unitary cells, the *Yee cells*. They are positioned such that the grid points of electric field are shifted from the grid points for the magnetic field by a half cell. This arrangement of two shifted grids for the two fields is chosen because for each time step, the electric (magnetic) field strength of a grid point can be calculated by the curl of the surrounding magnetic (electric) field points and vice versa. With this setting, the propagation of electromagnetic fields can, therefore, be calculated efficiently and accurately. In modern days, where multi-core processors are the norm, most FDTD software packages make use of

multiprocessing, i.e. they distribute the computational load on all available computer cores. This can decrease the computation time considerably.

The only crucial factor for this calculation is choosing the spacing distance for the investigated geometry. This spacing has to be small enough for accurate results but should not be too small as the computation amount scales to the grid distance with the fourth power for three-dimensional investigations. Additionally, all mesh points have to be held in memory, which can quickly accumulate to a few tens of gigabytes for larger simulations. In order to determine sufficiently small mesh sizes, convergence tests were performed, in which the spacing was gradually lowered until the experimental results converged to a steady result. Apart from the three geometrical dimensions, also the time stepping is linked to the mesh size and scales directly proportional to it. Here, the scaling factor between the two, commonly known as the *Courant factor* [37], can be freely chosen and should be sufficiently small. Especially when describing dispersive materials by models like the Lorentz-Drude model (see also section 2.3.1), the Courant factor has to be chosen small enough in order to accurately sample the assumed oscillators for the dispersive behaviour.

Finite-difference time-domain studies are nearly omnipresent in nanophotonic or nanoplasmonic studies as they are able to answer many different design and optimization questions [38]. For this reason, many different software algorithms and packages are available. Two different open source FDTD simulation packages were employed for this thesis, *MEEP* [39] and *openEMS* [40] as well as the commercial package *Lumerical FDTD Solution* [41]. The latter served mostly as a tool to triple check the simulation results obtained with the two free software packages. The choice for open source solutions is mainly based on two reasons: First, due to the lack of licensing restrictions, the packages could be run on many different computers and Linux clusters. Most notably, for high resolution simulations, which require a large amount of computing power, the high-performance Linux cluster *CoolMuc2* operated by the Leibnitz Supercomputing Center (LRZ) was used [42]. The second reason is the possibility to check or adapt the underlying code itself. This was of particular importance for using openEMS, which was developed mainly for radio-frequency applications and had to be expanded with some features necessary for simulations in the optical regime.

The reason for employing openEMS alongside the well-established de facto standard free FDTD software package MEEP lies mostly in its ability to perform simulations on non-uniform grids. While MEEP necessitates geometrical grids, which are evenly spaced within the simulation region, openEMS employs a FDTD method known as the *equivalent circuit* (EC) method [40]. In its essence, the EC method performs a coordinate transformation from the electric/magnetic field strengths of the Yee cell to edge voltages and currents by multiplying the field strength of a grid point with the length of the cell. This procedure has the advantage of making the variables independent of the chosen size of the Yee cell. Consequently, one can choose different grid sizes for different parts of the investigated geometry and, therefore, reduce the computational amount significantly.

Calculation of the Emission farfield

One advantage of FDTD techniques is the fact that one can observe the field properties at a certain point at any time and determine their evolution. This is particularly useful for

directly investigating nearfield properties like field enhancements or cavity quality factors [34]. However, some investigations are more interested in the resulting emission pattern of a nanosystem far away from the structure, i.e. in the farfield of the simulated geometry. Observing field properties at a point far away from the actual simulation domain causes a major problem: Naively, the simulated space would have to be extended to the observation point and both simulation time and computational demand would scale accordingly with the distance. It becomes immediately apparent that this approach is not feasible for small spacing distances. Instead, FDTD simulations typically involve a separate calculation step for obtaining the field properties in the farfield of the structure.

In its essence, transforming a numerically obtained field distribution from the nearfield to some point in the farfield of the structure is based on the *(surface) equivalence principle* [43]: When investigating a light emitting structure, one can define an arbitrarily shaped (closed) surface around that structure and find suitable equivalent electric and magnetic surface currents such that the fields inside the closed surface equal to zero. Using this procedure, all information about the electromagnetic fields emitted by the arbitrarily shaped structure in the surface is contained in the electric and magnetic surface currents. Finding the field properties at a chosen point far away from the investigated structure can be, therefore, calculated solely by employing the found surface currents and *Huygens' principle* [44].

In order to perform nearfield-to-farfield projections, FDTD packages can directly record and accumulate the electromagnetic field properties at a chosen surface, e.g. the edge of the simulation cell, for all time steps in one simulation run and employ Fourier transforms to obtain field properties for chosen frequencies. From these accumulated fields, the electric and magnetic equivalent currents can be derived and the field properties at a chosen point far away from the simulation space can be calculated [43]. The computational load necessary for nearfield-to-farfield computations depends heavily on the size of the chosen surface and can lead to computation times comparable to those of the FDTD simulation itself.

3.2. Dielectric Slot Waveguides

In this section, the design and optimization of planar waveguide structures offering large collection efficiencies for incorporated nanoemitters is presented. For many applications, especially in quantum information sciences, planar waveguiding structures are of particular interest as they offer the possibility to combine different building blocks for a nanophotonic circuit on a single carrier chip [45]. Ideally, all constituent elements of such an *on-chip* experiment can be directly realized on the carrier substrate. Here, the fundamental element of the circuit is the light source, i.e. the part which creates photons with high yield and reliability. One approach for this is to directly integrate the light source in the waveguiding structure by coupling the emitter to the guided mode of the waveguide. This mode of operation is the working principle of a *slot waveguide*, which allows for high coupling efficiencies of a pre-chosen nanoemitter to the guided waveguide mode. In the following, the basic design principles and the optimization of such a waveguiding structure are presented. The basics for the experimental realization of such a structure is described in appendix A.

3.2.1. Evanescent Coupling of Nanoemitters to Dielectric Waveguide Structures

One approach to couple light emitted by a point-like nanoemitter to some light guiding structure like an optical fiber or a waveguide is the usage of evanescent coupling. Here, the emitter is positioned at a region of the structure, where part of one or more guided eigenmodes are located, which means that there is some field overlap between the light field emitted by the emitter and the guided light field from the waveguide structure. For a point-like source with dipole orientation $\hat{\boldsymbol{\mu}}$ positioned at a position $\mathbf{r}_0$, the coupling can be expressed in terms of the *emission enhancement factor* α. It describes the emission rate into the guided mode Γ_{wg} of the waveguide normalized by the emission rate Γ_{iso} of the emitter without any structure. With the help of Fermi's Golden Rule, α can be described in terms of the scattering cross-section of a dipole $\sigma_A = 3\lambda_0^2/\left(2\pi n^2\right)$ and the group index $n_{gr} = c/v_{gr}$ of the investigated mode as

$$\alpha = \frac{\Gamma_{wg}}{\Gamma_{iso}} = \frac{1}{2}\frac{n_{gr}}{n\left(\boldsymbol{r}_0\right)}\frac{\sigma_A}{A_{eff}\left(\boldsymbol{r}_0, \hat{\boldsymbol{\mu}}\right)}\langle\hat{\boldsymbol{e}} \cdot \hat{\boldsymbol{\mu}}\rangle^2 \tag{3.1}$$

Here, $\hat{\boldsymbol{e}}$ is the unit vector of the electric field, $n\left(\boldsymbol{r}_0\right)$ is the refractive index at position $\boldsymbol{r}_0$ and A_{eff} is the *effective mode area*, whose properties are discussed later on. A detailed derivation can be found in [46].

Another figure of merit for the coupling of light from a dipolar emitter to a waveguide structure is β, which is a measure of the flux Γ_{wg} coupled to the waveguide mode normalized by the overall emitted flux Γ_{rad}, which combines the coupled flux and the emission into free space modes Γ_{free}:

$$\beta = \frac{\Gamma_{wg}}{\Gamma_{rad}} = \frac{\Gamma_{wg}}{\Gamma_{wg} + \Gamma_{free}} \tag{3.2}$$

Assuming the properties of the point-like dipole emitter being fixed, equations 3.1 and 3.2 mainly depend on the effective mode area A_{eff}. For a guided electromagnetic mode with propagation in z direction, which is characterized by the electric field $\mathbf{E}\left(x, y\right)$ and the magnetic field $\mathbf{H}\left(x, y\right)$ in the xy-plane, the effective mode area can be calculated in vector notation as [47]

$$A_{eff} = \frac{\left(\iint_{-\infty}^{\infty} \mathbf{S_z}\left(x, y\right)\,dxdy\right)^2}{\iint_{-\infty}^{\infty} \left(\mathbf{S_z}\left(x, y\right)\right)^2\,dxdy} \tag{3.3}$$

Here, the integrand $\mathbf{S_z}\left(x, y\right) = \left(\mathbf{E} \times \mathbf{H}^*\right) \cdot \hat{\mathbf{e}}_z$ is the z component (i.e. the axis along the waveguide) of the time-averaged Poynting vector, which is also called the *power flow*. A thorough derivation of this formula starting from the nonlinear Schrödinger equation can be found in [48].

The effective mode area A_{eff} can be interpreted as a measure for the confinement of the guided mode, to which the dipole emitter should couple to. For large coupling efficiencies, the electromagnetic field of the waveguide mode should, therefore, be well confined to the area of

the emitter. One realization of such a confined mode are nanophotonic cavity structures with small mode volumes [49, 50]. However, the strong concentration of the optical mode to the inside of the cavity comes at the cost of very limited bandwidth [51]. For solid-state emitters, which are normally not purely Fourier-limited in their spectral emission width, this correlates to the loss of emission, which is not in resonance with the nanocavity. In order to overcome the limited bandwidth, for some applications purely dielectric waveguiding structures can be advantageous. They also offer the possibility to engineer their optical mode structure by optimizing the waveguide cross-section.

The possibly simplest case of a planar waveguiding structure on a substrate material is that of the strip waveguide, which consists of a rectangular dielectric strip of a high refractive index material on a substrate with lower refractive index. By choosing an appropriate geometry, the guided modes of strip waveguides can carry large evanescent field tails reaching into the surrounding of the waveguide.

(a) Eigenmode TE0   (b) Eigenmode TE1
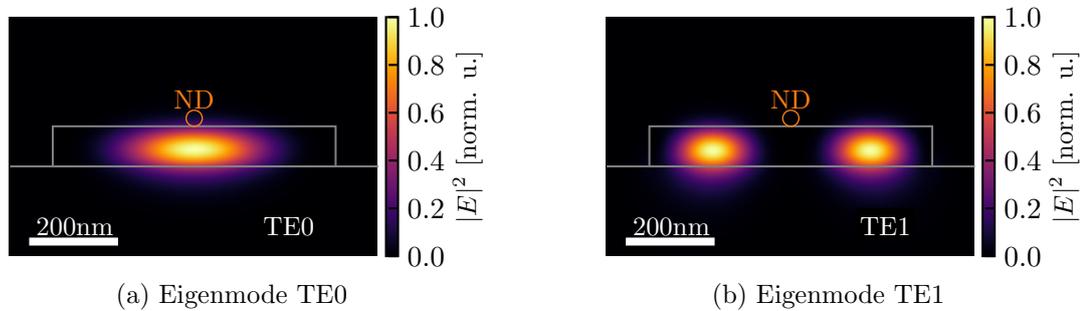
Figure 3.2.: Guided fundamental modes of a dielectric strip waveguide made from Ta_2O_5 on a planar fused silica substrate with waveguide dimensions of 700 nm in width and 100 nm in height at a wavelength of 630 nm, which is shortly before the mode cutoff of the TE1 mode. (a) Fundamental transverse-electric mode and (b) first higher TE mode. The orange circle indicates a quantum emitter ND positioned on top of the waveguide at the evanescent field of the guided modes.

Figure 3.2 presents the first two transverse-electric eigenmodes of a dielectric strip waveguide made from Ta_2O_5 (refractive index $n_{wg} \approx 2.1$) on a planar fused silica substrate (refractive index $n_{sub} \approx 1.45$) for a wavelength of 630 nm. The width of 700 nm and the height of 100 nm were optimized for two purposes: On the one hand, the cutoff wavelength for the TE1 mode is shortly below the zero-phonon line for the negative charge state of the nitrogen-vacancy center at 637 nm (compare section 5.2) so that only one guided mode is supported. On the other hand, the remaining fundamental transverse-electric mode features a strong evanescent tail reaching into vacuum above the waveguide. As indicated by the orange circle in the picture, evanescent coupling for an emitting particle located at this position can occur. More detailed investigations of this geometry (compare [46]) indicate a possible relative coupling efficiency β for correctly oriented dipolar emitters of about 30%. Additionally, this high coupling efficiency can be expected over a broad spectral region due to the fact that the shape of the guided modes, which are determined by both the geometry and the corresponding refractive indices, varies slowly with changing wavelength. This behaviour is especially useful for quantum emitters with broad emission spectra like the nitrogen-vacancy center.

One further optimization for the coupling to dielectric strip waveguides is to embed the waveguide in a homogeneous surrounding, a configuration, which is called a *buried waveguide*. This symmetrification of the geometry also results in a symmetric waveguide mode, which is more suitably localized on the upper waveguide edge [46]. However, in practical cases, this would necessitate a two-step process of first placing the nanoemitter on the structure and a subsequent covering of the waveguide with e.g. sputtered fused silica (compare appendix A), which would severely lower the success probability for creating the envisioned combined structure. Additionally, this symmetric dielectric configuration would allow the formation of a guided fundamental transverse-magnetic mode, which counteracts the design goal of a single-mode waveguide.

3.2.2. Basic Idea of Dielectric Slot Waveguides

While a simple dielectric strip guide works well enough up to a certain point, its performance in terms of the coupling efficiency β is limited as most of the guided mode is still trapped inside the waveguide. For higher coupling efficiencies, the waveguide structure has to be modified such that it traps the guided mode to a higher degree in an air region leading to very small effective mode areas and, consequently, higher coupling efficiencies. One approach to boost β further is that of a dielectric slot waveguide, which is known for providing very confined modes in a small empty region of space [52, 53, 54]. Similar to the case of the strip waveguide, this very special property is preserved for a large spectral region as it - again - relies mainly on the refractive index properties of the geometry, whose dispersion is rather small for dielectrics in the visible and near-infrared.
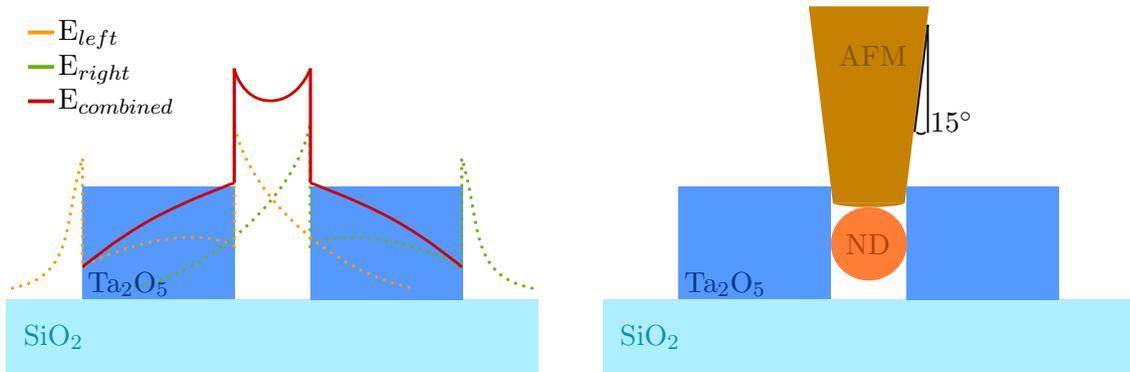
(a) Electric field combination of two part waveguides.

(b) Limitation on the height of the waveguide: need for accessibility by an AFM tip.

Figure 3.3.: Basic principles and ideas of investigated slot waveguide structures. (a) Scheme of the electric fields of the two waveguide parts, which form a combined optical mode concentrated in the slot region between the two waveguide parts. (b) Scheme of the limitation on the waveguide height as the slot region should be accessible for AFM cantilever tips with an attached nanodiamond (ND).

Figure 3.3(a) shows the basic working principle of a dielectric slot waveguide, which consists of two part waveguides separated by a central slotted region (hence the name). For the modes of a normal strip waveguide like the one presented in figure 3.2, the electric fields don't

abruptly end at the outer edges of the waveguide but extend as evanescent tails into the lower refractive index material. The interface conditions of electromagnetic fields (compare section 2.1) demand that the electric field component normal to any interface scales on both sides inversely with the refractive index, whereby a sudden increase in field intensity before the evanescent tail occurs. This behaviour is employed in dielectric slot waveguides: Looking at the electric field of the transverse-electric modes for both part waveguides separately in figure 3.3(a), both of them show the increase in field strength at the interfaces. The principle of slot waveguides now is to place two of those interfaces close to each other, by which the evanescent field tails of both waveguide parts add up and form an overall mode, which is concentrated in the empty region in between the two dielectric strips.

The strength of the electric field confinement inside the slot depends mainly on the distance between the two part waveguides: the narrower the slit, the larger the field strength, which directly relates to an increase in coupling efficiency. Additionally, increasing the waveguide height further improves confinement. However, two facts limit the minimally usable slot width and the corresponding waveguide height: The employed quantum emitter, which is often hosted in a material shell, has to fit inside the slotted region. Moreover, the procedure for actually placing the emitter in the slotted region has to be geometrically possible. Figure 3.3(b) illustrates these limitations in the framework of this work. Typically, the employed nanodiamonds have a size of several tens of nm for NV-centers and are placed by an ablated AFM cantilever tip with an typical tip angle of about $15°$. Compare section A.2.2 for further details about the positioning procedure. When combining both factors, the optimal slot width amounts to $40\,$nm for a corresponding waveguide height of 180-$200\,$nm.

3.2.3. Mode Structure of Ta_2O_5 Slot Waveguides

For a dielectric slot waveguide made from Ta_2O_5 placed on top of a planar fused silica substrate, the typical mode structure obtained for wavelengths below the mode-cutoffs looks like those presented in figure 3.4. The optical modes were simulated using the free and open-source software package *MIT Photonic Bands* (MPB), which is already described in section 3.1.1.

The first two eigenmodes for both transverse-electric (TE) as well as transverse-magnetic (TM) polarized light is shown in figure 3.4 for a wavelength of $600\,$nm. The assumed waveguide is located on top of a planar fused silica substrate and has a height of $180\,$nm with a slot width of $40\,$nm and an overall waveguide width of $550\,$nm. For this chosen geometry and wavelength combination, only the four presented modes are supported. For the TE0 mode, the desired trapping of the guided mode inside the slot region occurs, so the evanescent coupling mechanism should perform well also for transverse-electric polarized quantum emitters located in the middle of the waveguide structure.

The other three waveguide modes do not show reasonable evanescent field tails between the waveguide parts. Consequently, one would not expect reasonable coupling for those modes, a fact which is clearly visible in the FDTD simulations for the coupling efficiency in section 3.2.4. As a light source positioned inside the waveguiding structure would couple to all available modes (assuming sufficient field overlap), the overall observed coupling efficiency for a slot waveguide with higher-order modes would be small. Additionally, for many applications one single defined guided mode is needed. To fulfill all requirements, therefore, requires optimizing

(a) Eigenmode TE0

(b) Eigenmode TM0

(c) Eigenmode TE1

(d) Eigenmode TM1
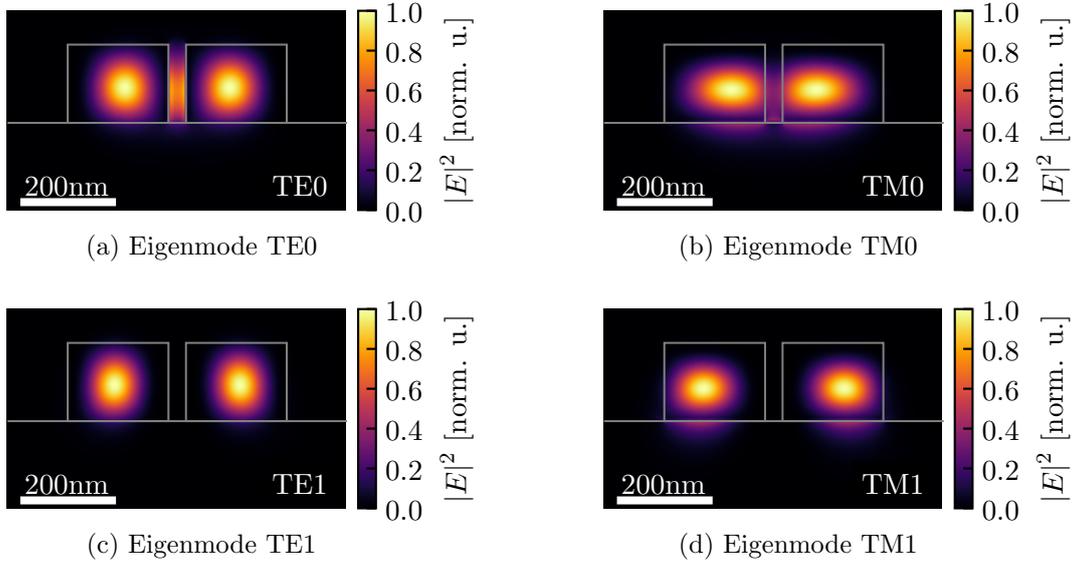
Figure 3.4.: The typical mode structure of Ta_2O_5 slot waveguides with height $180\,\mathrm{nm}$, slot width $40\,\mathrm{nm}$ and overall waveguide width $500\,\mathrm{nm}$ calculated for a wavelength of $600\,\mathrm{nm}$, which is shortly before the mode-cutoffs for the higher order modes occur. (a) and (c) show the 0th and 1st order transverse-electric modes, (b) and (d) present the corresponding transverse-magnetic modes. Strong field concentration in the slot region is visible for the TE0 mode in (a), which promises large coupling efficiency for emitters located in this region of the waveguide.

the optical mode profile of the waveguide. In particular, the waveguide design should have a geometry such that the mode cutoffs for all TM modes as well as the TE1 mode should occur at a wavelength slightly shorter than the part of the optical spectrum, for which the waveguide should collect light efficiently.

Most parameters of the waveguide design are fixed by various constraints: the slot width at the minimal reasonable value of $40\,\mathrm{nm}$, the height of the structure at $180\,\mathrm{nm}$ and the material properties. In contrast to that, the waveguide width and the assumed emission wavelength can be freely chosen. Sweeping both over realistic values allows for calculating important parameters, which help choosing the final design. For this, both eigenmode simulations and dynamic FDTD simulations for wavelengths between $500\,\mathrm{nm}$ and $800\,\mathrm{nm}$ and waveguide widths between $400\,\mathrm{nm}$ and $550\,\mathrm{nm}$ were performed. They are presented in the next section.

3.2.4. FDTD Simulations of the Coupling Efficiency

Analyzing the finite-element simulations as described in the previous section gives valuable insight in the eigenmode structure of the envisioned dielectric slot waveguide and allows for identifying points, where mode-cutoffs occur. However, for directly analyzing the coupling efficiency one can expect for a point-like quantum emitter positioned in the center of the slot region, additional FDTD simulations have to be performed. They can be also used for

analyzing related questions like the influence of the orientation of the emitting dipole on the coupling efficiency.

A scheme of the geometrical setup for simulating the coupling efficiency β of nanodiamonds positioned in the center of a Ta_2O_5 slot waveguide is shown in figure 3.5(a). The slot waveguide is modeled with a fixed slot width of 40 nm and waveguide height of 180 nm and contains a diamond sphere (ND) with a width of 40 nm and a point-dipole emitter in the center. To obtain β according to equation 3.2, the transmitted power flux through both waveguide ends as well as the overall power emitted by the point source is calculated. In order to ensure that only light guided by the bound waveguide mode is taken into account, the simulation region along the waveguide axis has thus to be chosen long enough. Other important free parameters for the simulation were the cross-sectional dimensions of the simulation and the grid spacing. In order to choose those parameters appropriately, independent simulation tests were performed. Firstly, the mode structure reaching the waveguide ends was evaluated to ensure that it only contains the guided modes and not scattered light. Additionally, by analyzing the propagation of waveguide eigenmodes, a minimal simulation cross section was found, which ensured that also the evanescent tails of the guided mode can propagate and are not altered by the chosen boundary condition. Furthermore, the grid spacing was gradually lowered until the results converged. In the end, the simulation region was chosen to be of size 3 µm by 3 µm by 30 µm with a spatial grid spacing of 5 nm putting the memory demand in the range of some 100 GB. For this reason, simple stationary computers weren't powerful enough, instead the simulations were performed on the Linux-Cluster CoolMuc2 run by the *Leibniz Supercomputing Centre*. More information can be found in [42].

Ideally, the mode structure of dielectric slot waveguides would be similar to that of the optimized dielectric strip waveguide and consists of only one single guided mode. As illustrated in figure 3.3, the slot width should be chosen reasonably small to allow for strong field confinement but large enough to allow the positioning of a nanodiamond with an AFM cantilever in the slot region. This demand puts limitations on both the slot width and the waveguide height. Using the typical tilt angle of AFM cantilevers, which are about 15°, a compromise for the two parameters was selected: The width the slot was chosen to be 40 nm and the height was fixed to 180 nm. The remaining free parameter for an optimized geometry is then, assuming that the material composition and the substrate are fixed, the overall width w of the waveguide. In this context, w is defined as the width, which is spanned by the two part waveguide strips.

A series of FDTD simulations of the coupling efficiency for varying values w and the emission wavelength were performed for the three orientations of the emitting dipole, namely transverse-electric (TE), transverse-magnetic (TM) and transverse-longitudinal (TL) orientation. Figures 3.5(b) to 3.5(d) summarize the resulting calculated coupling efficiencies β for the three dipole orientations using 130 individual simulation runs each. Superimposed in the 2D plots are the approximated mode-cutoffs for the first higher-order TE- and TM-modes, which were determined in independent eigenmode simulations. In this context, higher order waveguide modes appear for decreasing wavelengths and/or increasing waveguide widths.

As one would expect from the eigenmode structure presented in figure 3.4, high coupling efficiencies should be possible for modes confined in the slot region, which occurs for the fundamental TE mode. This is clearly reflected in the simulated coupling efficiency in figure

(a) Scheme of the FDTD simulation geometry

(b) β for TE polarized emission

(c) β for TM polarized emission

(d) β for TL polarized emission
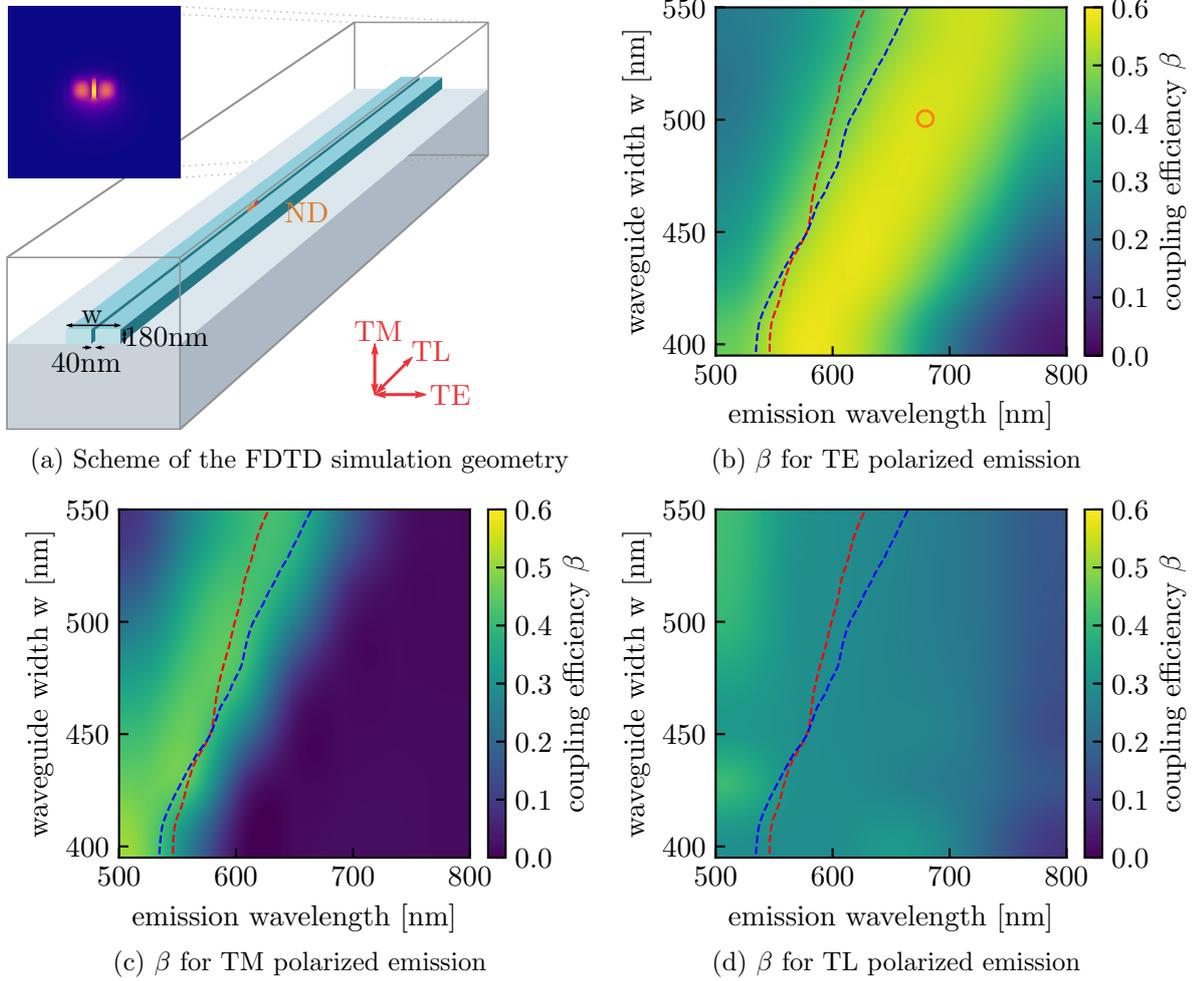
Figure 3.5.: Simulated coupling efficiency of quantum emitters in a nanodiamond (ND) to dielectric slot waveguides. (a) Scheme of the geometry used in FDTD simulations with varying waveguide widths w for calculating the coupling efficiency β for different orientations and emission wavelengths. (b)-(d) Simulated coupling efficiency β for a dipole emitter with (b) TE-, (c) TM- and (d) TL-polarization to a Ta_2O_5 waveguide with a fixed slot width of $40\,nm$, a height of $180\,nm$ and varying overall width in dependence of the emission wavelength. Mode-cutoffs of the first higher TE- and TM-mode determined by independent eigenmode calculations are depicted by a red and blue dashed line respectively. The orange circle in (b) marks the point for further analysis of the influence of position offsets of the point source on the coupling efficiency presented in figure 3.6.

3.5(b): For a point-source emitting transverse-electrically polarized light, high coupling efficiencies of about 60% of the overall emission can be expected for a spectrally broad region of about 100 nm. A clear boundary to this region of large β are the mode-cutoffs for the higher-order modes. This behaviour is a direct result of the mode structure: If the first higher-order TE1 and TM1 modes of the slot waveguide are present, the overall mode structure of all available modes aren't confined to the slot region anymore and, therefore, the overall evanescent coupling to the guided modes is strongly reduced. On the other hand, for very large emission wavelengths, which are spectrally far away from the mode-cutoffs, the fundamental TE0 mode is not well-localized in the slot region, which also results in weak coupling efficiencies.

For TM- and TL-polarized emission, the situation changes drastically. Transverse-magnetic polarized light only couples to the higher-order TM modes as the fundamental TM0 mode does not provide mode confinement in the slot region. Consequently, the achievable coupling efficiencies are rather low. TL-polarized light, which emits along the waveguide long axis, can couple to the guided modes to some degree, however this behaviour is limited to low β values and is nearly independent of the actual waveguide width and the emission wavelength.

Comparing the simulation results in figure 3.5 clearly shows that high evanescent coupling efficiencies are only possible when employing quantum emitters, which provide transverse-electric polarized light. Consequently, accurate positioning of the quantum emitter is essential. This high degree of position control can be provided by the presented pick-and-place technique to position pre-selected nanodiamonds with the possibility for in situ observation and control of the diamond position using photoluminescence measurements. Compare section A.2.2 for a detailed explanation of this technique.
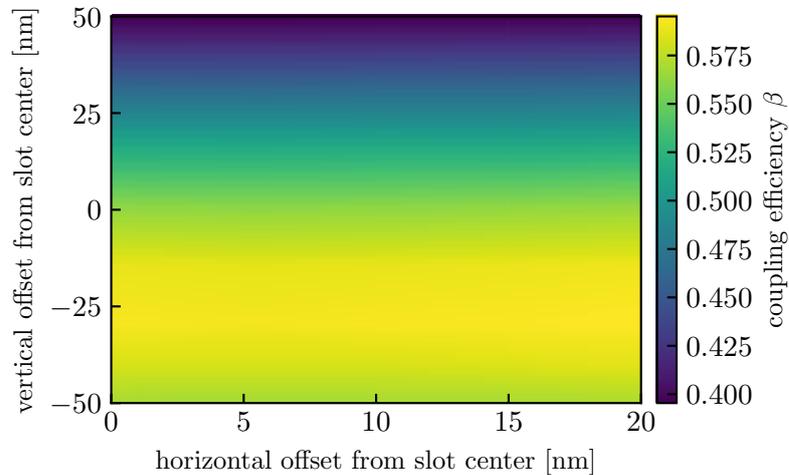
Figure 3.6.: Influence of position offsets on the coupling efficiency of quantum emitters coupled to dielectric slot waveguides. The simulation setup is identical to that presented in figure 3.5 with a fixed waveguide width of 500 nm and TE-polarized emission at 680 nm. Horizontal and vertical offsets of the point of emission are defined relative to the center of the slot waveguide.

Apart from precise control of the emission polarization, also accurate positioning of the nanodiamond inside the slot is essential for high coupling efficiencies. In figure 3.5, the quantum emitter was assumed to be positioned in the center of the slot structure as this represents the

maximum depth possible for the AFM cantilevers currently used in the pick-and-place procedure (compare figure 3.3(b)). In order to investigate the influence of position offsets from the slot center on the coupling efficiency β, further FDTD simulations with varying emitter positions were conducted. They are summarized in figure 3.6 and show a negligible dependence of the coupling efficiency to horizontal offsets but a strong dependence on displacements in the vertical direction. This behaviour can be attributed to the mode structure inside the slot region (compare also the mode structure in figure 3.4): For the horizontal direction, the fundamental TE mode varies only slightly between the two waveguide parts, yet it does not stretch evenly for the full waveguide height. Here in vertical direction, the mode maximum is slightly off-centered towards the substrate, which has a higher refractive index compared to the surrounding air. This localization is reflected in the calculated coupling efficiencies, which show a maximum at 25nm below the slot center.

3.2.5. Further Details on the Proposed Structure

While the evanescent coupling mechanism for nanoemitters like defect centers hosted in nanodiamonds to slot waveguides promises high light collection efficiency, for an operational device some further design elements have to be integrated and investigated. Especially for real-life applications, this involves solving two main challenges: One is to achieve easy and reliable optical access to the nanoemitter, the other is to increase the durability of the device for practical applications. Additionally, the propagation losses of light traveling along the waveguide should be minimized. Strategies for solving these requirements are illustrated in figure 3.7, which shows a schematic of the envisioned final device, and are presented in the following paragraphs.
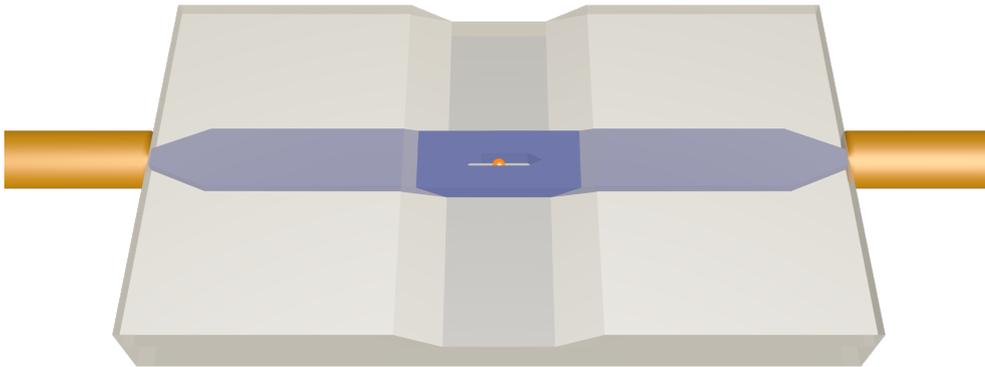
Figure 3.7.: Schematic for the proposed design of the final slot waveguide device. Apart from the central region, which includes the slotted region, the structure is capped with sputtered fused silica and the waveguide is tapered on either ends to allow for efficient coupling to and from attached single-mode optical fibers.

The main cause for propagation losses in strip waveguides is their uneven structure. Due to limitations in the fabrication process, their geometrical cross-section is subject to deviations. In waveguide structures fabricated in a top-down lithography-based process with subsequent etching of the structure from a solid layer (compare section A.1), this roughness is mainly confined to the sides of the waveguide. The strength of light being scattered into unbound

modes is then determined by the confinement of the guided waveguide mode to the rough sidewalls [55, 56]. For normal strip waveguides like the one presented in figure 3.2, the majority of light is confined to the inside of the structure, which results in low propagation losses well below $1\,dB/mm$. See [57] for propagation measurements of waveguide structures fabricated during this thesis. In contrast, by design the TE-polarized fundamental mode in figure 3.4(a) is strongly confined to the inner sidewalls of the slot region and therefore highly susceptible to any roughness there. Hence, for long waveguide structures, which are typical for dielectric waveguides, it is beneficial to keep the slot region short and perform the remainder of the propagation path in a normal strip waveguide. Coupling from the slot waveguide mode to the strip waveguide mode was investigated by FDTD simulations and showed very good coupling efficiencies of above 80% [58]. However, the reverse process of coupling light from a strip waveguide to the slot region is unfavorable as the much larger strip waveguide mode has to be converted to the confined slot waveguide mode and can be estimated to only 12%. Nevertheless, for many applications, i.e. exciting the nanoemitter by coupling in excitation light, this value is large enough. Additionally, by gradually decreasing the width of the taper in an adiabatic manner, efficient coupling from the strip to the slot waveguide can be also achieved [59].

Increasing the durability of the device and efficient optical coupling to and from the waveguide can be solved simultaneously by capping the waveguide structure with a layer of fused silica. The capping layer firstly serves as a protective layer against mechanical effects like scratching of the surface. As the substrate is also made from fused silica, both layers have the same refractive index. This means that the waveguide mode of the buried waveguide is symmetrical and differs from the one for the strip waveguide without capping. In order to prevent scattering due to a sudden change in the eigenmode profile, the capping layer thickness has to be gradually increased. This technique is known as *adiabatic tapering* and uses the fact that a gradual change in the mode profile over several 10s of µm allows for (nearly) loss-free mode conversion [60].

The same tapering technique can be employed for coupling the waveguide mode to an optical single-mode fiber. For many applications, optical access to the waveguide structure is easiest realized by a fiber-based setup. Planar waveguides can be easily coupled to optical fibers by so-called *butt coupling* [61]. Here, the optical fiber is brought in direct contact with the nanostructure. The resulting coupling efficiency for the fiber-nanostructure interface is then determined by the mode overlap between the two systems. For the single-mode strip waveguides presented here, the typical mode size is in the order of a few hundred nanometer, which is much smaller than the typical mode size of a standard single-mode fiber measuring several micrometers [62]. Hence, the strip waveguide mode has to be mode-matched for efficient coupling. Approximating the cylindrical symmetry of the optical fiber mode is already performed by the capping layer. Additionally, the size mismatch can be resolved by employing adiabatic tapering of the strip waveguide. By gradually decreasing the width of the waveguide to a width of about $80\,nm$ over a length of several tens of µm, the waveguide mode extends to a size comparable to that of the single-mode fiber. FDTD simulations predict a power coupling efficiency at the fiber-waveguide interface above 80% for the fundamental TE mode [58].

3.3. Modeling of Plasmonic Bullseye Resonators

The main task for the nanostructures presented in this thesis is, as already explained in the introduction, the efficient collection of light emitted by point-like nanoemitters. Apart from the direct integration into light guiding structures like dielectric slot waveguides, which was presented in the previous section 3.2, reshaping the emission of the nanoemitter by changing their surrounding is a promising approach. One type of nanophotonic structure capable of reshaping the farfield emission are concentric metallic ring structures, so-called *plasmonic bullseye resonators*. Their basic properties and working principle shall be investigated in detail in the following sections.

3.3.1. Basic Working Principle of Bullseye Structures

For a more detailed understanding of the working principle, let's first examine the basic ideas behind plasmonic bullseye structures and start by looking at a physics textbook like experiment: interference induced by a multi-slit. In this experiment treated in most of the standard textbooks in physics (e.g. [44]), a plane wave propagates towards a barrier, which has small regularly spaced gaps. As these openings in the barrier are tiny and their size is much smaller than the wavelength of light, Huygens–Fresnel's principle tells that each opening acts as a secondary point source and the overall emission pattern observed at a distance far away (i.e. the *farfield*) is the well-known regular interference pattern of emission maxima and minima. This type of experiment can be directly transferred to nanophotonics by replacing the slits with nonclassical point-like dipolar emitters.

Figure 3.8 shows the results of FDTD simulations of simple point-like isotropic emitters above a perfectly reflecting mirror surface in three settings. For each of the three cases, both a figure presenting a sketch of the geometry and the emitted nearfield power pattern calculated as $\mathbf{E}^* \times \mathbf{D}/2$ as well as a figure plotting the emitted farfield for different emission wavelengths are given. The simulations themselves were performed in two dimensions and the simulation region was surrounded by absorbing boundaries to avoid reflections. Additionally, the electric and magnetic fields were recorded at the boundaries of the simulated space in order to perform a subsequent nearfield-to-farfield transformation calculation (compare also section 3.1.2).

The first case examined is that of a simple emitting point on top of a reflecting surface in figures 3.8(a) and 3.8(b). Due to the perfect mirror in the vicinity of the isotropic emitter, its emitted field is reshaped to that of a broad cone pointing in upward directions. As one would expect, this behaviour is nearly completely independent of the chosen emission wavelength. The remaining, very small wavelength-dependence stems from the fact that the point emitter is located some nanometers above the perfectly reflecting mirror, which causes interference between the directly upwards emitted light and light, which is first reflected at the mirror plane.

Figures 3.8(c) and 3.8(d) treat the case of several emitters separated by a regular distance of one *pitch* size, which corresponds to the case of the multi-slit experiment mentioned earlier. The pitch spacing was chosen to be slightly smaller than the emission wavelength λ and was fixed to $\lambda/1.1$. Here, all emitting sites emit in phase and form a constructive interference pattern at zero degree, i.e. the normal direction relative to the mirror. This constructive

(a) Single point source on a planar mirror

(b) Wavelength-dependent farfield profile of (a)

(c) Multiple point sources emitting in phase

(d) Wavelength-dependent farfield profile of (c)

(e) Multiple point sources with varying phase

(f) Wavelength-dependent farfield profile of (e)
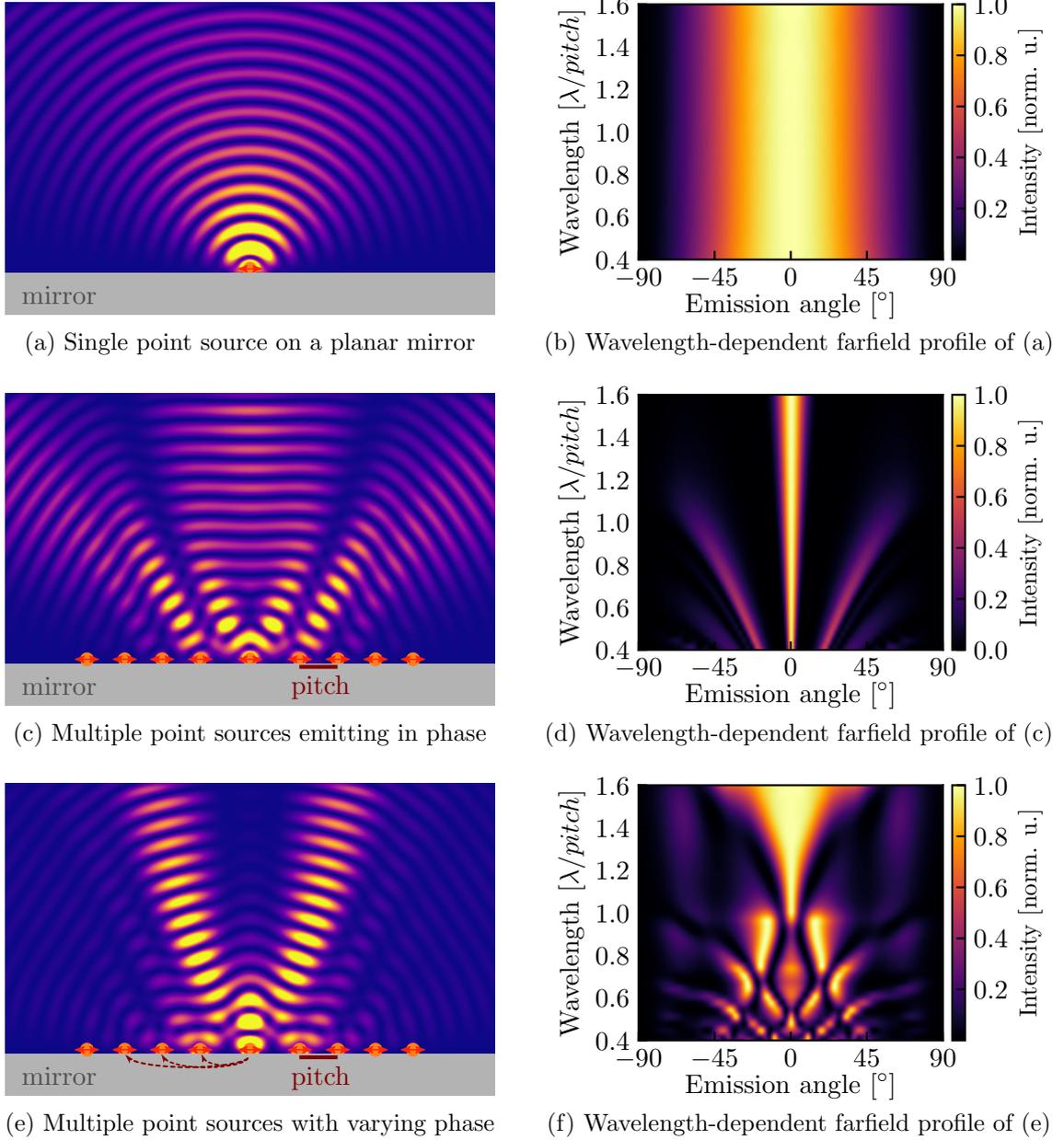
Figure 3.8.: Simple 2D models of isotropic point sources on a perfectly reflecting mirror motivating the basic working principle of plasmonic bullseye resonators. For each geometry, both the nearfield pattern of the emitted power $\mathbf{E}^* \times \mathbf{D}/2$ at a chosen wavelength of $\lambda = 1.1 \cdot pitch$ and the corresponding wavelength-dependent farfield emission pattern is shown. (a) and (b): Single point source on a planar mirror. (c) and (d): Multiple point sources with distances of one pitch size to each other emitting in phase. (e) and (f): Multiple point sources with distances of one pitch size to each other emitting with a relative emission onset corresponding to the propagation time from the central emitter.

interference, which forms a very sharp emission cone for the 0th interference order, is nearly independent of the employed wavelength. Instead, constructive interference is ensured by the point sources emitting in phase and their symmetric arrangement. For smaller λ, the first and second order constructive interference is visible too. The emitted farfield pattern would be perfect for efficient light extraction as the collection optics could be restricted to small emission angles and, therefore, small numerical apertures. Additionally, the performance of such a device would be nearly independent of the emission wavelength of the nanoemitter.

Finally, figures 3.8(e) and 3.8(f) illustrate the case of point sources arranged in a regular pattern but with varying emission onset times. These onsets of the emission were chosen such that they correspond to the traveling time of light from the central emission point to the point of the emission. The idea behind this reflects the main goals of designing and creating nanophotonic or -plasmonic devices: light from a single emitter should be collected and redirected into small emission angles as this allows for efficient collection of the emitted light. One way to achieve this emission reshaping is by using the previously discussed multi-point interference, which induces redirection of the emission by interference of regularly spaced emission sites. However, applying multiple quantum emitters in a real experiment would contradict the purpose of a single-photon source. Instead, the emission of one single site has to suffice for this effect. In other words this means that part of the emission has to be shuffled to emission points at a regular distance to the central "real" emitter.

In this simulation, this is mimicked by the relative phases of the emitting sites. Additionally, in the simulation their relative emission strength gradually decreases for larger distances to the center. Similar to the case of the emitting sites being in sync, the resulting farfield pattern shows a region of constructive interference into the zeroth interference order for wavelengths slightly higher than the chosen pitch size of the emitter array. Here, nearly all of the emission is redirected into a very narrow emission cone. This gradually decreases when the wavelength increases and moves further away from the chosen lattice pitch.

3.3.2. Toy Model for Bullseye Structures

While the idea of reshuffling part of the emission from a central emitting site to well-defined places proves very capable for reshaping the emission of a point-like emitter, some physical process is necessary to provide this feature. For bullseye resonator structures, this mechanism is plasmonics, which in essence describes the interaction between light and a metallic material. The fundamentals of plasmonics and especially plasmonic effects on a metal-dielectric interface are described in section 2.3. This section aims to illustrate an easy-to-use phenomenological model for the working principle of plasmonic bullseye structures, which can provide some fundamental design rules for real devices. While the employed toy model simplifies many physical processes or omits them altogether, it nonetheless serves as a robust tool to explain many effects of real planar plasmonic ring structures.

For this simplified model, we restrict the analysis to the two-dimensional case. Figure 3.9 illustrates the main concept of the analysis: Starting from a defined point depicted in orange with height d above the ring structure, the interference conditions for constructive interference in the upward direction is investigated by comparing the optical path length differences. Apart from the direct propagation of light in upward direction, it can also be either reflected from
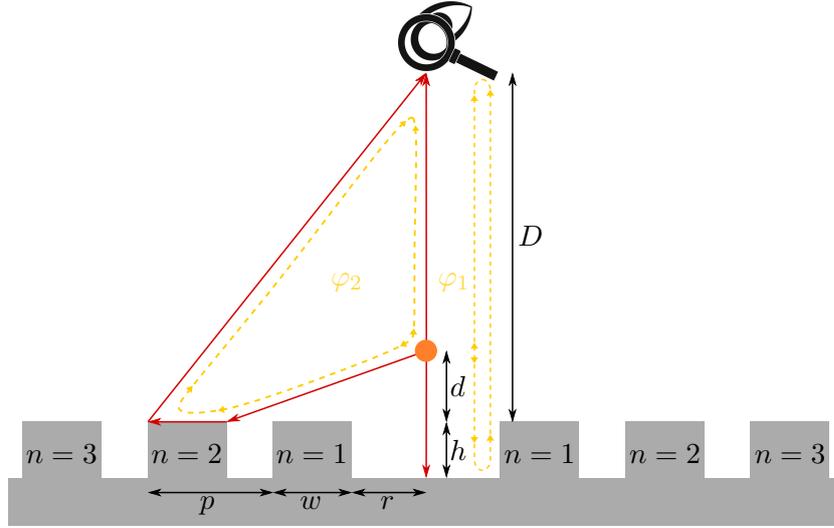
Figure 3.9.: Simplified two-dimensional model of a bullseye resonator structure. A point-like emitter depicted in orange is located in the center of the structure at a certain height d above metal rings with width w and height h, which are separated by a pitch size p and a central radius r. The observation point is situated in the farfield of the plasmonic structure at distance D. For constructive interference at the observation point, the two optical path differences φ_1 and φ_2 have to be a multiple of the wavelength.

the reflective surface or it can be redirected by the rectangular metal blocks with height h, width w and pitch size p, which represent the rings in the 3D case. This propagation path involves the transfer of light from free space modes to bound surface plasmon polariton (SPP) modes at the inner ring edge, the SPP propagation along the ring surface and the re-emission into free space modes at the outer edges.

In order to analyze the bullseye resonator toy model, the different optical paths "reflection from the surface" and "capture and re-emission at a ring site" have to be examined relative to the direct upward propagation path. This leads to two interference conditions for the relative optical path length differences φ_1 and φ_2

$$\varphi_1 = \left(2 \cdot (d+h) + \frac{\lambda}{2} \right) \quad \% \quad \lambda \tag{3.4a}$$

$$\varphi_2 = \left(\sqrt{((n-1) \cdot p + r)^2 + d^2} + \frac{w}{v_{SPP}} + \right. \tag{3.4b}$$
$$\left. + \sqrt{D^2 + (r + w + (n-1) \cdot p)^2} - (D-d) \right) \quad \% \quad \lambda$$

For constructive interference, relative path differences of a multiple of the wavelength should occur, indicated by the modulo $\% \, \lambda$ operator. Additionally, for reflection of the metallic substrate, an additional phase shift occurs, which corresponds to an optical path of $\lambda/2$. When propagating along the ring surface, light is bound to the interface as surface plasmon

polaritons, whose propagation velocity v_{SPP} differs from that of light in free space modes. v_{SPP} can be calculated directly from published material data (compare section 2.3.2), for an aluminium-air interface it is approximately 97.5% of the speed of light in free space.
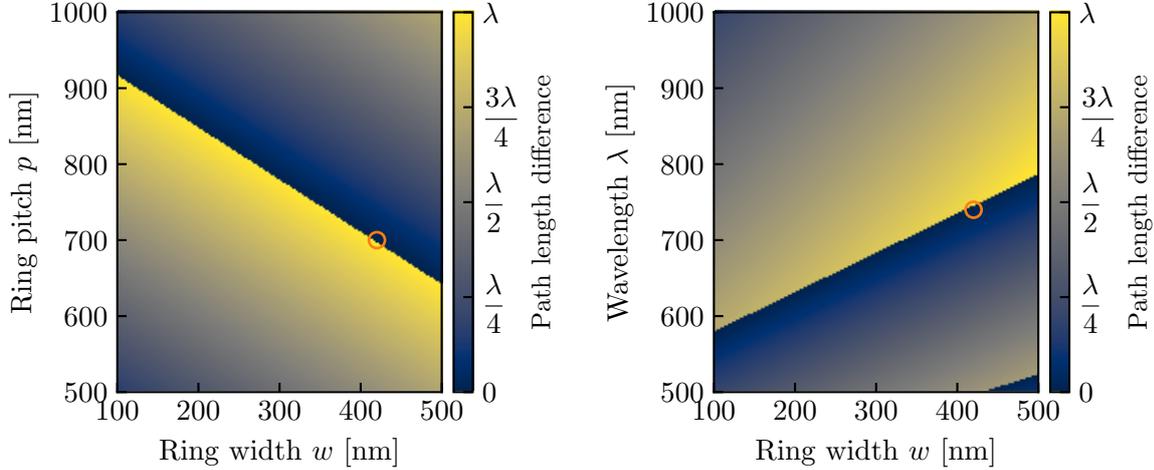
(a) Calculated relative optical path lengths for varying ring pitches and ring widths

(b) Calculated relative optical path lengths for varying emission wavelengths and ring widths

Figure 3.10.: Calculated relative optical path lengths for different parameters of the bullseye toy model of figure 3.9. Emission in the normal direction is achieved by an overall net path length difference of zero. The orange circles indicate optimized geometrical parameters derived from full-fledged FDTD simulations presented in section 6.3. (a) Varying the pitch of the plasmonic rings and their width. (b) The influence of the ring width in dependence of the emission wavelength.

As the conditions for constructive interference in equations 3.4 include several free parameters, a series of iterative optimization steps are necessary to find an optimal set of parameter values, which are not necessarily independent of each other. Figure 3.10 illustrates the results for optimized parameters as a phase map, where the resulting net optical path difference for a given parameter set is colour-coded. In figure 3.10(a), the ring width and the ring pitch are varied for a fixed wavelength of 740 nm, corresponding to the emission wavelength of the silicon-vacancy center. The resulting net phase shift is colour-coded for each combination. Constructive interference in forward direction is observed for a certain relation between the ring pitch and the width of the rings. Figure 3.10(b) illustrates a similar result for varying ring widths and emission wavelengths and a fixed ring pitch of 700 nm. Also here, there are linear relations between the two varied parameters, where the net phase shift is a multiple of 2π.

As the phase conditions in equations 3.4 are mathematically trivial, they can be evaluated with nearly no computation time. Still, they can hint towards a set of geometrical design parameters by which working bullseye structures can be constructed. But how do their results compare to full-fledged FDTD simulations, which take into account all relevant geometrical and material-related effects? Such simulations, which are presented in section 6.3, present optimized parameters very similar to that of the simple toy model presented here. The orange circles in 3.10 illustrate the parameter values optimized by the 3D FDTD simulations. It is

immediately clear that there is very good agreement between the results of the toy models and the full-featured FDTD simulations. One can therefore conclude that metallic bullseye structures can be roughly designed by a simple phase model and their geometry subsequently fine-tuned by computationally much more demanding FDTD simulations.

Limitations of the Phenomenological Model

Even though the previously presented toy model for bullseye resonators can already explain many phenomena by simple phase-matching analyses, it can nonetheless fail to take into account certain aspects of both real metallic resonator devices and the incorporated quantum emitters. One aspect is the purely two-dimensional treatment of the resonator structure. This can be problematic if the emission in the center of the resonator is not uniform but polarization-dependent. The effect of polarization in the system, which breaks the rotation symmetry is therefore neglected altogether. However, in reality most real quantum emitter like colour centers in diamond or semiconductor quantum dots exhibit polarized emission. Also material properties like absorption or optical resonances of the nanostructure are not included in the toy model. A prominent example for this is the interband resonance of aluminium at about 800 nm (compare section 2.3.1), which has to be taken into account when designing real aluminium ring devices.

Additionally, the toy model also assumes a perfectly reflecting base substrate. However, in the experimentally investigated devices, which are presented in chapter 6, the reflective surface is made from a dielectric filter with many alternating dielectric layers. For a phase-matching calculation, the single reflecting surfaces would have to be approximated independently, which would make the toy model approach tedious. In this context, more complex questions like the influence of structural uncertainties, e.g. surface roughness, cannot be modeled easily either. Those questions have to be investigated by simulations, which include all geometrical and material parameters.

Chapter 4.

Experimental Techniques and Methods

According to the *scientific method*, which is the backbone for modern sciences, knowledge is created by empirical studies or careful observation of hypotheses and theoretical models [63]. For this reason, conducting physical investigations requires the possibility for testing nature by means of experiments. In the course of this thesis, testing the hypotheses and models of quantum emitters and their interplay with nanophotonic and -plasmonic structures is performed mainly by optical experiments, where the emitted light is measured and analyzed.

This chapter describes the main experimental and technical techniques and procedures employed during this thesis. At first, the photoluminescence setup is presented, which can be combined with both an atomic force microscope for mechanical measurements and manipulation (compare also section A.2.2) or a second microscope stage for performing Fourier-space measurements of the emission. After that, techniques for time-resolved measurements are described in detail with an emphasis on experimental uncertainties and their resulting influence.

4.1. Confocal Photoluminescence Setup

The main tool employed for the characterization of defect centers in diamond is photoluminescence. In principal, photoluminescence experiments are based on optically exciting a bound system, whose excited state then decays radiatively. When detecting the emitted photons, conclusions can be drawn upon the electronic and energetic structure of the investigated system. The main theoretical details of this measurement principle for optically active colour centers in diamond is described in chapter 5. In this section, the actual technical implementation of this method is presented.

The main components of the experimental setup employed for the majority of the experimental investigations for this thesis is presented in figure 4.1. Its basic working principle is that of a *confocal laser-scanning microscope* (CLSM) and consists of optical excitation and detection paths, which are spatially overlapping along the beam path, hence the name confocal. The overlapping beams are focused by a microscope objective, at whose focal point the quantum emitter is located. The main advantage of the confocal measurement scheme is its ability for high spatial resolution of both excitation and detection, which facilitates high signal-to-noise ratios and suppresses background or stray fluorescence light [64]. In the experiment, spatial overlap between the two beam paths is achieved by using dichroic mirrors (DM), which couple excitation laser light to the excitation beam path. This light was provided by a frequency-doubled continuous-wave solid-state Nd:YAG laser emitting at 532 nm.
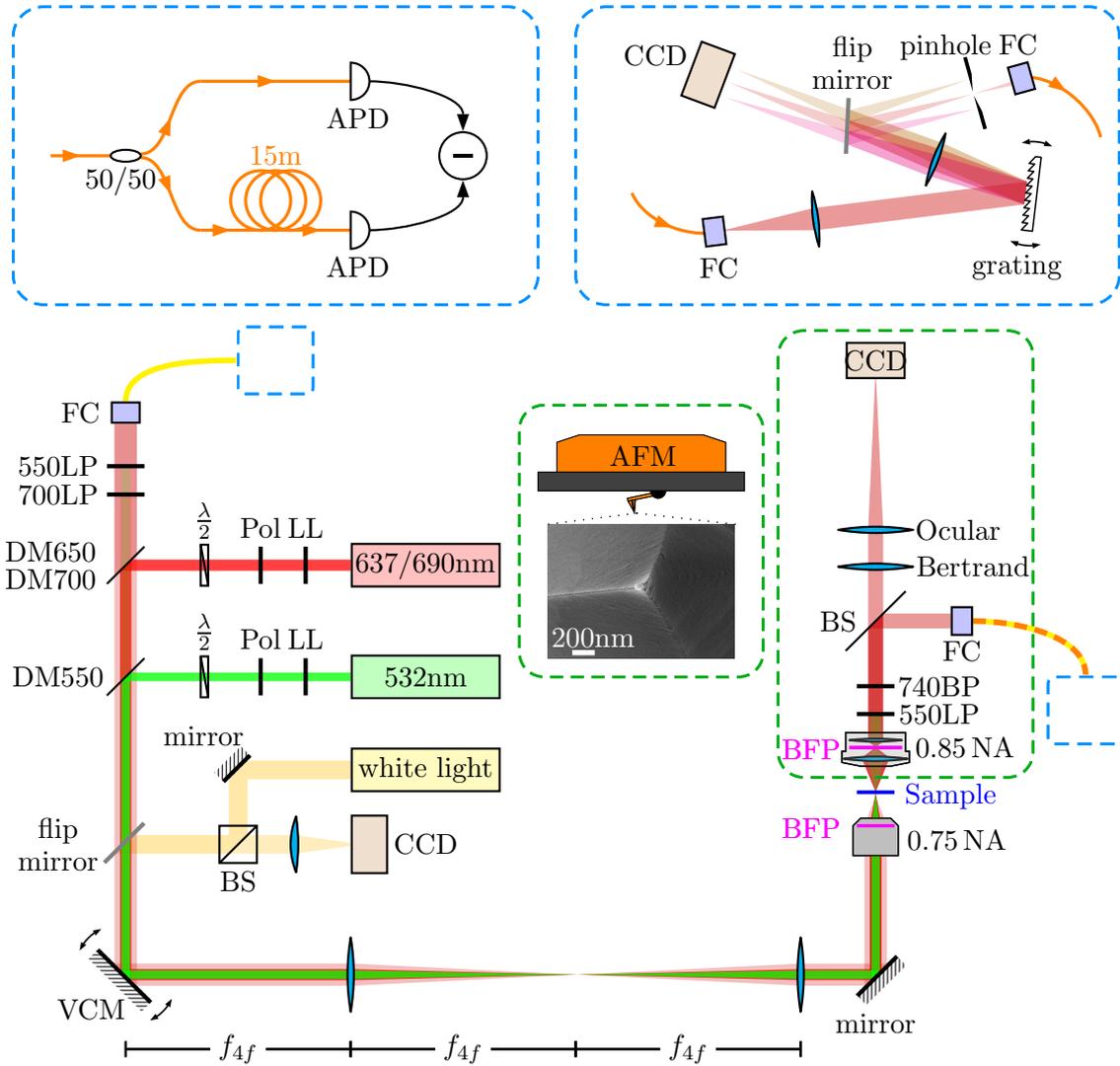
Figure 4.1.: Scheme of the employed room-temperature confocal photoluminescence setup and the detection units. In its essence, the setup consists of a 4f-geometry, with which the sample plane can be scanned through the 0.75 NA objective with excitation laser light via a rotating voice-coil mirror (VCM). The light emitted on the sample plane can be either collected confocally in reflection with a fiber coupler (FC) or analyzed in transmission using a hybrid real and Fourier space microscope stage with a 0.85 NA microscope objective. Alternatively, the upper side of the sample plane can also be accessed with an atomic force microscope (AFM) for position nanomanipulation of nanodiamonds. If the emitted light is coupled to an optical fiber, it can either be analyzed temporally using a fiber-based HBT setup or it can be analyzed spectrally using a spectrometer setup with a reflective optical grating. A detailed description of the working principle and the various components can be found in the running text.

The laser light was further modulated with an additional acousto-optical modulator in double-pass configuration (not shown), which allowed for fast on-/off-switching of the laser with switching times of about 15 ns. Additionally, a second laser beam path in the experiment supplied pulsed laser light at either 637 nm for the resonant excitation of the nitrogen-vacancy center (see also section 5.2.3) or light at 690 nm for off-resonant excitation of silicon-vacancy centers. The 637 nm laser light was provided by a home-built pulsed diode-laser setup, which created pulse widths of about 7 ns [65]. For the much faster decaying silicon-vacancy centers, light pulses at 690 ns were provided by a commercial *PicoQuant PDL 800-B* picosecond pulsed laser diode with pulse lengths of about 150 ps. As all laser setups were connected to the experiment by single-mode optical fibers, switching between the different laser setups was facilitated by simply reconnecting the appropriate fiber and replacing the dichroic mirror in the setup. The laser light wavelengths in the experiment were further spectrally cleaned by small-bandwidth laserline filters (LL) and polarized by linear polarizers and subsequent rotating lambda-half waveplates. In confocal operation mode, the collected light emitted by a nanoemitter was coupled to a single-mode fiber collimator (FC) after reflected excitation light is spectrally filtered out by longpass filters (LP) at 550 nm and/or 700 nm.

Scanning of the sample surface was achieved by employing a controllable, rotating OIM100 *voice-coil mirror* (VCM) from *Optics in Motion* in combination with a 4f geometry consisting of two achromatic lenses with focal lengths of 150 mm. In this configuration, the fourth focal point is located at the *back-focal plane* (BFP) of the 0.75 NA focusing microscope objective. Thus, tilting of the VCM is translated to a shift of the beam at the focal point of the objective. As the voice-coil mirror can be adjusted with high bandwidth, optical scanning of the upper sample surface through the substrate could be performed at a rate of 75 Hz and high repeatability as with this scheme, the sample itself stayed static in lateral directions. For accurately placing the sample surface at the focal point of the objective, it was mounted on a piezo stage for vertical positioning.

Additional coarse control of the sample position was provided by an additional mechanical three-axis positioning stage. In order to easily control the focus position on the sample surface, an imaging system was used. For this, white light was coupled into the beam path, which illuminated the sample surface. The reflected image of the sample surface was then imaged by a CCD camera. In order to directly image the excitation beam position, the flip mirror used for the imaging consisted of a reflecting neutral density filter, which was chosen such that it attenuated the excitation laser power to a level similar to that of the illuminating white light. This allowed to directly position the excitation beams on the sample surface manually with high accuracies below 1 μm, limited mainly by the resolution of the mechanical positioning stage.

As the confocal photoluminescence setup illuminates and collects the nanoemitter under investigation through the sample backside, the upper half of the sample is freely available for further experimental equipment. For this, either an *Easyscan 2 atomic force microscope* (AFM) from *Nanosurf* or a second microscope stage capable of performing Fourier analysis could be positioned on the upper side of the sample. The AFM was employed for mechanical analysis and manipulation of the nanoemitter position, the so-called pick-and-place procedure, which is described in detail in section A.2.2. Analyzing the emission properties of nanoemitters and the influence of nanostructures on the emission was carried out by the second microscope stage. This stage consists of a microscope objective with a numerical aperture of 0.85 and

maps the emission either on a highly sensitive CCD camera (*pco.1300* from *PCO*) or couples the collected light to an optical fiber via a fiber coupler. Similar to the confocal detection scheme, an optical longpass filter at 550 nm and/or a bandpass filter at 740 nm for detecting silicon-vacancy centers were employed. Analysis of the emitted light via the CCD camera could be carried out either in real space or in Fourier space by employing an additional aspheric *Bertrand lens* (focal length 75 mm), which maps the back-focal plane of the objective on the CCD chip. Thus measurements in Fourier space were performed by simply combining the permanently installed ocular lens with the additional Bertrand lens. A more detailed description about Fourier microscopy and the performance of the employed setup is given in the following section 4.2.

Emitted light, which is coupled to an optical fiber either confocally or by using the second microscope stage, can be analyzed either temporally by directly measuring the photon statistics via the *Hanbury Brown and Twiss* (HBT) effect or spectrally using a spectrometer setup. The basic principle for a HBT type of measurement is based on splitting the investigated light into two parts and measuring correlations and/or anticorrelations between events on both detectors [66, 67]. Typically, this measurement is performed in free space by employing a beamsplitter and two silicon avalanche photodiodes (APDs) from *PerkinElmer*. Initial experiments with this configuration, however, showed optical crosstalk between the two APDs due to breakdown flashes [68], which are detected by the other detector. For this reason, for most experiments a fiber-based approach was implemented, which consisted of a multi-mode fiber beamsplitter with a splitting-ratio of 50/50 and an additional optical path delay of 15 m on one detection arm. By spatially separating the two detectors to separate housings and the additional optical delay, crosstalk between the two APDs could be completely avoided. The fast detection of APD events was performed by using a fast *time-to-digital converter* (TDC) based on the *Acam TDC-GPX* chip with a maximum timing resolution of 27 ps, which provided timestamps for the single events and allowed for software-based event correlation in post-processing.

For spectrally resolved measurements, a home-built spectrometer setup was used. This setup consisted of a reflection grating with 1200 lines/mm mounted on a high-precision rotation stage. The investigated light was first coupled to free space and spatially broadened. After being reflected on the grating and, therefore, spectrally separated, a large aspheric collection lens focuses the light on a highly-sensitive CCD camera (*Andor iDus*). This allowed for a maximum spectral resolution below 0.1 nm at 740 nm. Optionally, the dispersed light could also be redirected by a flip mirror and spectrally isolated by a pinhole before being coupled to an optical fiber, where it could be further temporally analyzed using the previously described HBT setup.

4.2. Fourier Microscopy

Fourier microscopy, or more exactly *Fourier-plane imaging microscopy*, is a technique with which Fourier images of an illuminated or emitting object are measured. As classical *Fourier optics* predicts, this Fourier image contains complementary knowledge to that of traditional real plane imaging: Instead of obtaining spatial information from a real plane microscope image, Fourier microscopy provides information about the angular distribution of emitted

light. This is of particular interest for studies concerning the emission shape of quantum light sources like hybrid systems consisting of nanoemitters in plasmonic bullseye structures.

4.2.1. Basic Working Principle

A schematic illustration of light propagation in a typical Fourier microscope setup is presented in figure 4.2. In optical microscopy, the Fourier image is located at the *back-focal plane* (BFP) of the imaging objective. As this image plane is typically situated inside the microscope objective, it needs to be imaged on a detector chip by an imaging lens, typically called the *Bertrand lens* in microscopy. In the actual experimental setup, this role was fulfilled by an aspheric lens with a focal length of $f_B = 75\,mm$. It is important to note here that for Fourier imaging the microscope objective has the be chosen carefully: As most objectives are optimized for real plane imaging, the properties of the back-focal plane, its position and exit numerical aperture are varying widely and have to be investigated carefully. For this thesis, a $0.85\,$NA achromatic objective from *Edmund Optics* with a small effective working distance of $150\,$µm was chosen after characterizing several alternatives.
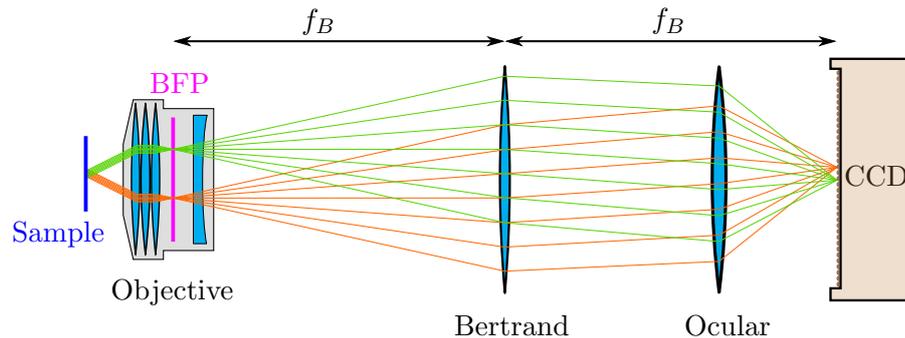
Figure 4.2.: Schematic illustration of light propagation in Fourier microscopy. Compared to a microscope for real space imaging, which consists of a microscope objective and an ocular lens, an additional Bertrand lens with focal length f_B maps the back-focal plane (BFP) of the objective on the CCD detector.

The actual design of the optical beam path for Fourier microscopy can vary: Instead of directly mapping the BFP on the CCD chip with a single Bertrand lens as chosen for the setup in figure 4.1, a configuration with intermediate focal points might be advantageous for absolute imaging performance [69]. The rather compact design of the presented experimental setup was chosen due to the fact that the complete transmission stage including the CCD camera and the fiber coupling system were housed in an optical cage system and mounted on top of a single three-axis *Tritor* piezo stage from *Piezosystem Jena*. However, detailed investigations of the performance of the Fourier imaging system, which are presented in the subsequent section 4.2.2, show that the imaging quality is more than adequate and yields a angular resolution of the Fourier microscope of approximately 0.15°.

4.2.2. Characterization and Calibration

Although the principle of Fourier microscopy and the application of this scheme in the experimental setup is straightforward, especially the usage of high NA optics, which is performance-optimized for real space imaging, has to be considered. As the objective was not designed for Fourier imaging, the quality can be susceptible to flaws like optical aberrations or beam clipping and, therefore, requires careful characterization and calibration to ensure the validity of the experimental results [69]. Tests of the Fourier transmission stage are presented in figure 4.3.

For a direct comparison between the real space and Fourier space performance of the optical setup, a periodic grating was employed. Figure 4.3(a) shows a real space image of the grating: It consists of a periodic array of gold bars with a lattice spacing of $10\,\mu m$ and was fabricated by electron-beam lithography (compare section A.1.2 for more details). Measuring an exact Fourier transform of this grating would now require the illumination of this grating with a true macroscopic plane wave, which does not exist. However, this plane wave illumination can be approximated easily by a collimated laser beam with large aperture, which was created by inserting an additional Fourier lens before the 4f configuration of the confocal laser path (compare figure 4.1).

Performing a Fourier transformation on the gold grating can be performed in two ways: either calculate the Fourier transform of the spatial light distribution or directly measure the Fourier transformation by imaging the Fourier plane on the detector chip. Ideally, both strategies should then yield the same result. Figure 4.3(b) illustrates a numerical *Fast-Fourier transformation* (FFT) of the real space image in figure 4.3(a). As one would expect, the FFT shows a regular periodic pattern, which corresponds to a discrete distribution of k-vector components introduced by the diffraction of the plane wave at the grating. The direct measurement of the k-space by the Fourier microscope setup is presented in figure 4.3(c), which shows a very similar k-space distribution as the numerical FFT method. Here, it is important to note that the similarity also holds for higher emission angles well above $45°$, which demonstrates that the setup performs well for the complete observable spatial angle.

While the grating measurement provides very good qualitative results, a more thorough quantitative characterization procedure was performed as well. For this, a collimated laser beam with a large aperture simulates a plane wave and illuminates the Fourier detection unit at specified angles relative to the optical axis. Here, one would expect a linear dependence between the illumination angle and the distance to the position for normal incidence on the CCD chip. An exemplary measurement result for this characterization shows figure 4.3(d), which reveals the expected linear dependence between the incident angle and the distance to normal incidence. Deviations from the linear behaviour are mainly attributed to uncertainties in the adjustment of the entrance angle, a statistical error which was accounted for by repeating the calibration multiple times.

Additionally, the transmission efficiency of the optical setup changes for off-axis illumination. Ideally, the objective would collect light beams from different incident angles equally well as long as they are within the objective's numerical aperture. This of course does not hold in practice as a microscope objective comprises of several lenses with additional internal beam apertures, which lead to clipping of the propagating beam for off-axis and/or off-normal

(a) Measured real space image of a grating

(b) Calculated FFT image of (a)

(c) Measured Fourier space image of (a)

(d) Angle-dependent optical performance tests
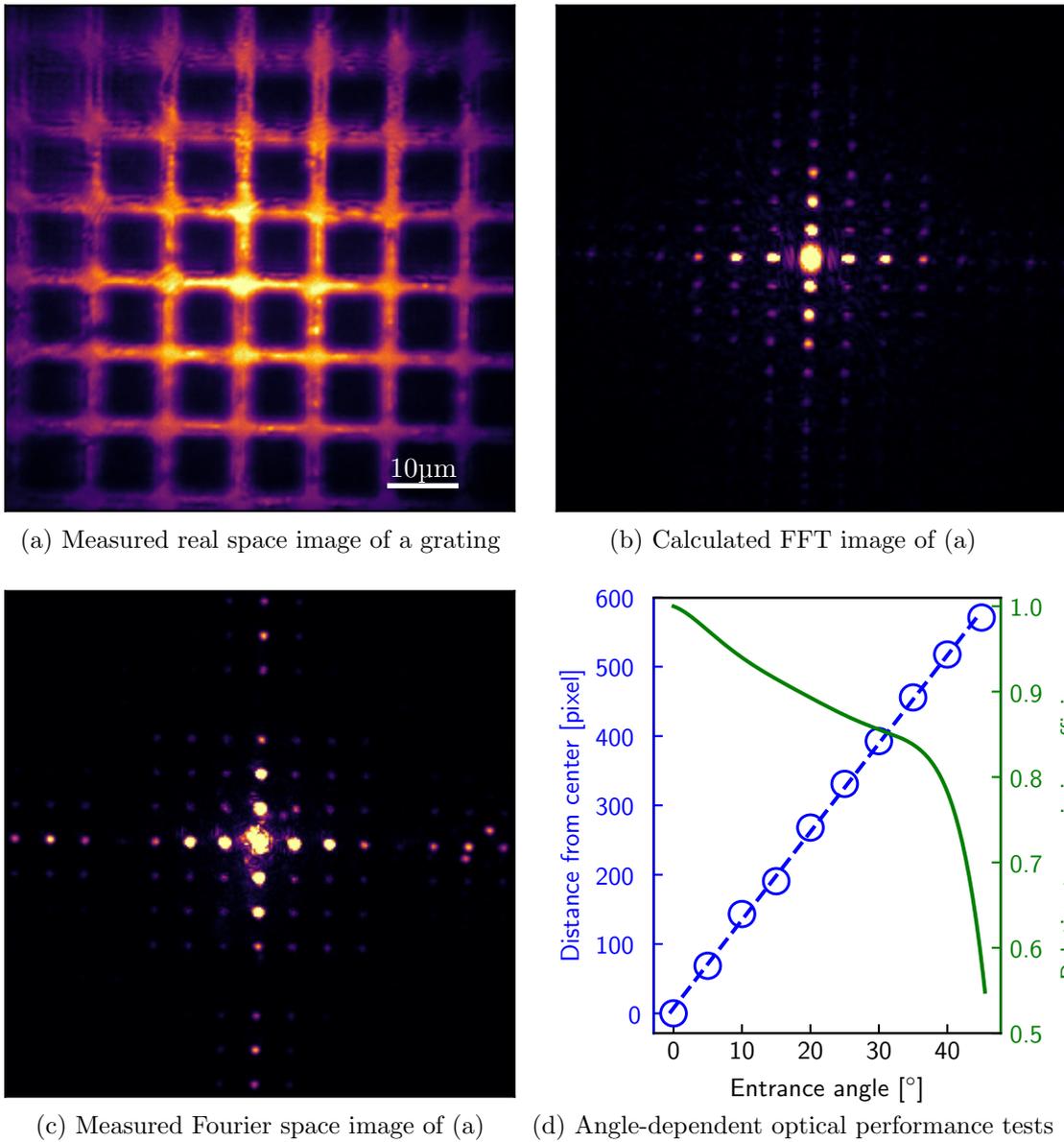
Figure 4.3.: Test of the Fourier microscope setup using a gold grating with a lattice pitch of 10 µm ((a)-(c)) and calibration measurements ((d)) using a large aperture collimated beam. (a) Real space microscope image of the grating. (b) Calculated Fast-Fourier transformation of the image in (a). (c) Measured Fourier microscope image of the grating using plane-wave illumination. (d) Linearity test and relative transmission efficiency of the Fourier microscope for plane-wave illumination using different entrance angles relative to the optical axis yielding an angular resolution of approximately 0.15° for the transmission stage.

incidence. For the employed microscope objective, figure 4.3(d) shows the transmission efficiency of the Fourier setup relative to the transmission efficiency for normal incidence. At low entrance angles, the transmission decreases only slightly, while as soon as the entrance

angle approaches the maximum acceptance angle (i.e. the objective's numerical aperture), the transmission efficiency drops quite drastically. Consequently, when evaluating k-space measurements, this effect was taken into account by normalizing the data accordingly.

4.3. Time-Correlated Single-Photon Counting (TCSPC)

The physical process of creating single photons using optically active states is a dynamic one: After the electron absorbs an excitation photon and reaches (possibly after via a sequence of very short-lived intermediate states) an excited state, it will decay into the energetically lower state after a characteristic lifetime and emit a photon. The statistics of this dynamics, i.e. the *lifetime* of the electron staying in the excited state (hence simply called the excited state) can be directly measured via time-resolved optical experiments. The probably most common method for this is the so-called *time-correlated single-photon counting* (TCSPC) method, whose working principle is outlined hereinafter.

4.3.1. Basic Principle of TCSPC

In a TCSPC experiment, the dynamics of the system is directly measured by timely resolving detection events with respect to the excitation time point. Figure 4.4(a) illustrates the experimental procedure: At fixed times, a short laser pulse excites the system, which emits a fluorescence photon after a characteristic, statistically varying time. The time difference between the detection of the excitation pulse and the fluorescence photon is then analyzed with a histogram (compare figure 4.4(b)). As the decay from an excited state to an energetically lower state is a purely statistical process, which is driven by random zero-point fluctuations, after recording many detection events (i.e. enough collected data points for each time bin), the resulting histogram reflects the dynamics of the system as the resulting decay curve $S(t)$ directly incorporates the lifetime τ_0 as the decay parameter:

$$S(t) = S_0 \cdot exp\left(-\frac{t}{\tau_0}\right) \tag{4.1}$$

It is important to note that only one exponential decay is considered. For investigations of ensembles of quantum emitters like measurements of the excited state lifetime of a nanodiamond incorporating several silicon-vacancy centers (compare section 6.4.2), this leads to an average excited state lifetime. In order to investigate the dynamics of systems with different decay processes, equation 4.1 can be adjusted accordingly.

4.3.2. Analyzing the Experimental Decay Curves

In an ideal TCSPC experiment, the measured time-delay histogram directly shows the excited state lifetime via the exponential decay curve. While this hold true in theory, imperfections and measurement uncertainties necessitate further analysis of the experimental output. There are two main contributions to the time uncertainties in TCSPC, one concerning the excitation pulse and the other the detection of single photons.
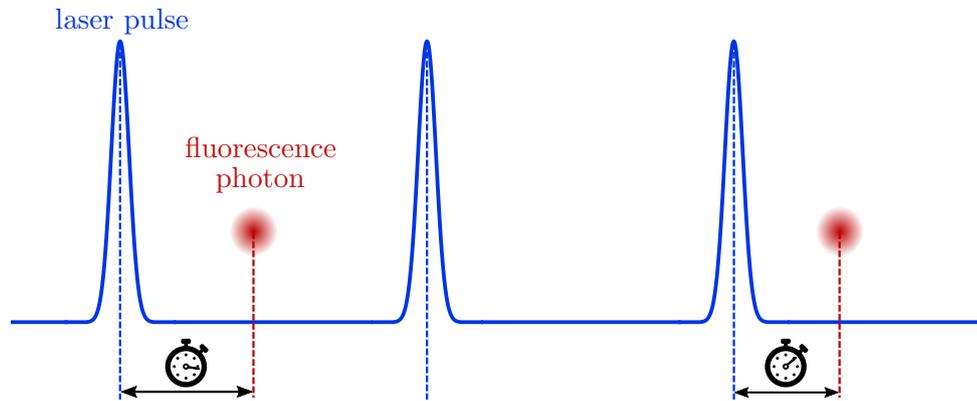
(a) Principal scheme of time-correlated single-photon counting, which measures the time difference between optical excitation pulses and detected fluorescence photons.
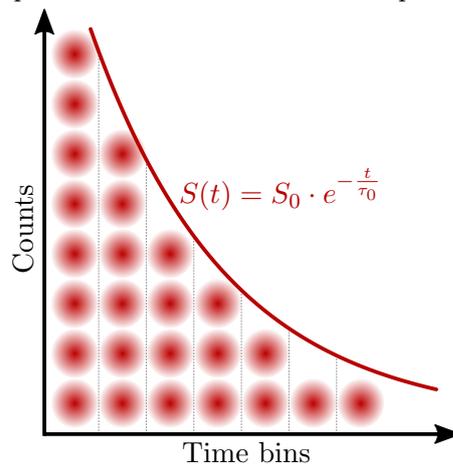
(b) Histogram of the arrival times of detected fluorescence photons.

Figure 4.4.: Principal scheme of time-correlated single-photon measurements: (a) A short, well-defined laser pulse excites the system, which emits a single photon after a characteristic lifetime. The time-differences between the laser pulses and the photon detections is recorded. (b) Accumulating the detections per time bin over time after excitation for many excitation-detection cycles leads to a typical decay curve, where the decay constant equals the excited state lifetime τ_0 of the system.
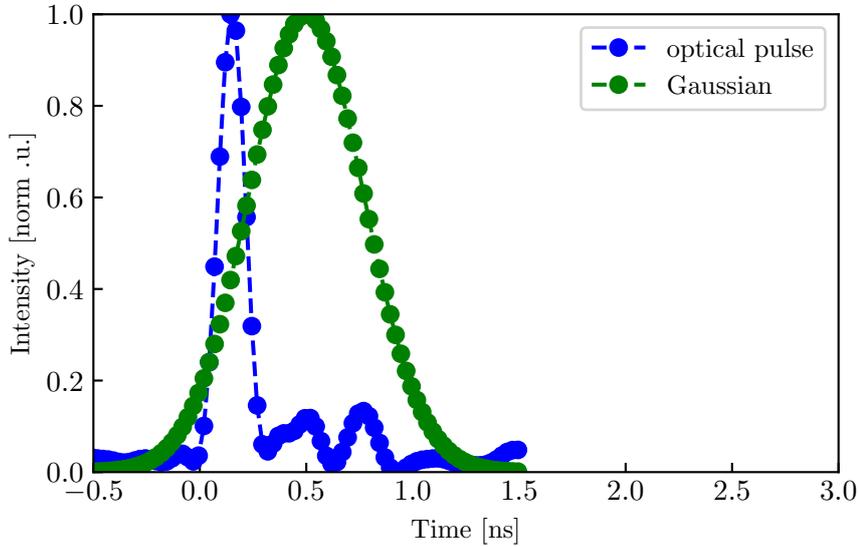
(a) Time trace of the optical excitation pulse at 690nm (blue) and an assumed Gaussian function with a FWHM of 540ps (green) representing the timing uncertainty of the detector.
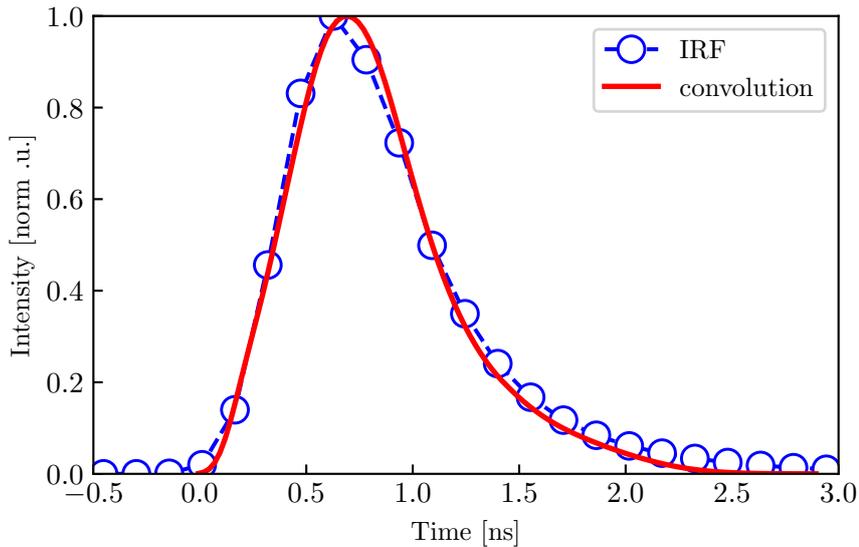
(b) Comparison between the measured IRF of the TCSPC detection system (blue) to a mathematical convolution of the two curves from (a).

Figure 4.5.: Investigation of the instrument-response function and its components. (a) shows the main components of the IRF, the optical excitation pulse with a FWHM of 150 ps measured with a fast photodiode (blue) and an assumed Gaussian distribution with a FWHM of 540 ps (green), which represents overall timing jitter of the system. (b) Comparison between the measured instrument-response function (blue), which was measured by detecting attenuated excitation laser pulses themselves with the TCSPC setup, and a convolution of the two signals of (a).

The starting point of the start-stop measurement should be fixed and well defined in time as the time difference to the stop events incorporates the desired time-sensitive information about the optical system. Therefore, an ideal excitation laser pulse for TCSPC would be infinitely short. Apart from the fact that fundamental physics make this objective rather impossible (an infinitely short laser would have an infinitely large bandwidth), the pulse length for diode lasers is normally limited by the length of the electrical signal for the laser diode, which limits it to typically from some 10 ps up to some 100 ps. Figure 4.5(a)) shows the time trace of the employed diode laser at 690 nm in blue measured with a fast photodiode (*Thorlabs SUV7-FC* with a bandwidth of 7 GHz). Here, the FWHM of the optical pulse is about 150 ps. Additional low amplitude afterpulses are also present, which stem from a slight impedance mismatch between the electrical signal driver and the laser diode itself. Nevertheless, as the intensity of the secondary pulses is much smaller than the main pulse, they can be neglected in the analysis.

The second contribution to timing uncertainty in TCSPC experiments is the detection procedure. The state-of-the-art technique for the detection of single photons with high timing resolution in the visible or near-infrared are *avalanche photodiodes* (APDs), where the incoming photon triggers an electron whose signal is then multiplied by impact ionization [70]. The time-critical point here is the time it takes the freed electron(s) to travel to the electrical connections of the APD chip. As the absorption point of the photon inside the chip is random, it introduces timing uncertainty. Additional jitter stems from the electric amplification of the signal [71]. For this thesis, PerkinElmer APDs with a typical timing jitter of about 350 ps according to the manufacturer were employed. The amplified electrical signals from the APDs are then fed as TTL pulses in a *time-to-digital converter*, where the arrival times of signals are recorded. Here, both the electrical signal from the excitation laser as well as the signal from the APD detection are tracked and their time difference recorded. Typical time lengths for the binning of the TCSPC histogram (compare figure 4.4(b)) in the experiment were about 150 ps. All detection uncertainties manifest in a purely statistically distributed timing uncertainty, which is well described by a Gaussian distribution with a FWHM of 540 ps in green in figure 4.5(a)).

The convolution of both the excitation laser signal with its finite length and the timing uncertainty of the detection is typically referred to as the *instrument-response function* (IRF) and incorporates all timing uncertainties of the experimental apparatus. The IRF can be directly experimentally determined by measuring the time dynamics of the (highly attenuated) laser pulse itself by e.g. inserting a mirror instead of an experimental sample. Figure 4.5(b) presents the IRF of the employed system determined with this method. In order to compare the independently obtained single components of the IRF to this, a convolution of the two curves from 4.5(a) is plotted in red. As one would expect, the convolution agrees with the measured instrument-response function to a high degree.

In a real time-correlated single-photon counting measurement, the resulting measurement curve $I(t)$ thus corresponds to a convolution of the instrument-response function $IRF(t)$ and the "real" decay signal $S(t)$ of the single-photon emitter:

$$I(t) = IRF(t) \otimes S(t) \tag{4.2}$$

4.3.3. Modeling the Modified Exponential Decay

Several strategies are possible for dealing with the influence of the IRF on the measured decay curve. Very often, the influence of the IRF on the measurement can be simply neglected as long as the examined lifetime is much longer than the width of the IRF (determined by both the optical excitation pulse and the timing jitter of the detection). This works nicely for systems like the nitrogen-vacancy center, which has an excited state lifetime of typically several 10 ns, much longer than any timing uncertainty in the experiment. For SiV centers, this does not hold as the excited state lifetime of about 1 ns is of the same magnitude as the uncertainty. Here, other approaches have to be applied.

One straightforward approach is to numerically deconvolute the IRF from the experimental signal. In theory, the resulting curve should then be free from any measurement influence and purely represent the decay dynamics of the system. However, numerical deconvolution is often mathematically not stable and the resulting curve, therefore, often very noisy and distorted. This is especially true when the number of time bins in the calculation is limited.

Another approach is the modeling of the IRF curve with an analytical function, which can be convoluted with the exponential decay. This results in a fitting curve for the overall measurement, which automatically incorporates all components. Often, a simple Gaussian function is fitted to the IRF curve and the obtained fit parameters are then used in an adapted fitting curve for the TCSPC measurement. However, a simple Gaussian function deviates quite strongly from the actual IRF curve. In the following, two possible more advanced model functions are discussed, which both yield good results. A more detailed analysis can be found in e.g. [72].

Modeling the IRF with a Modified Gamma Distribution

One approach for modeling the instrument response function accurately is the usage of a Gamma distribution. In a general case, this distribution can be written as

$$G(t) = a \cdot \frac{t^{c-1} \cdot e^{-\frac{t}{b}}}{b^c \cdot \Gamma(c)} \tag{4.3}$$

with $\Gamma(c) = \int_0^\infty t^{c-1} e^{-t} dt$ as the Gamma function. Note that the usual definition of the Gamma function does not include the proportionality factor a. For accurately fitting the measured IRF, however, this factor is of great importance.

The measured decay curve is then a convolution of the IRF modeled by the Gamma distribution $G(t)$ and an exponential decay $S(t) = S_0 \cdot exp\left(-\frac{t}{\tau}\right)$. Evaluating the convolution integral and substituting yields:

$$\begin{aligned}
I(t) = S(t) \otimes G(t) &= \int_0^t S_0 \cdot e^{-\frac{t-t'}{\tau}} \cdot a \cdot \frac{t'^{c-1} \cdot e^{-\frac{t'}{b}}}{b^c \cdot \Gamma(c)} dt' \\
&= S_0 \cdot a \cdot \frac{e^{-\frac{t}{\tau}}}{b^c} \cdot \left(\frac{\tau \cdot b}{\tau - b}\right)^c \cdot \frac{\Gamma(c) - \Gamma\left(c, \frac{\tau - b}{\tau \cdot b} t\right)}{\Gamma(c)}
\end{aligned} \tag{4.4}$$

Here, $\Gamma\left(c, \frac{\tau-b}{\tau \cdot b}t\right) = \int_{\frac{\tau-b}{\tau \cdot b}t}^{\infty} e^{-t} \cdot t^{c-1} \cdot dt$ represents the complemented incomplete gamma integral.

Figure 4.6 shows a fit of equation 4.3 to the measured instrument-response function determined by an independent calibration procedure. The obtained fit parameters can then be employed as fixed parameters for fitting a fluorescence decay curve with equation 4.4. Overall, the agreement between the fit and the measured data can be considered as quite good. However, there are some noticeable deviations, especially on the falling flank, which holds the main information for TCSPC measurements. Therefore, for an even better modeling of the instrument response, another approach is presented in the next section.
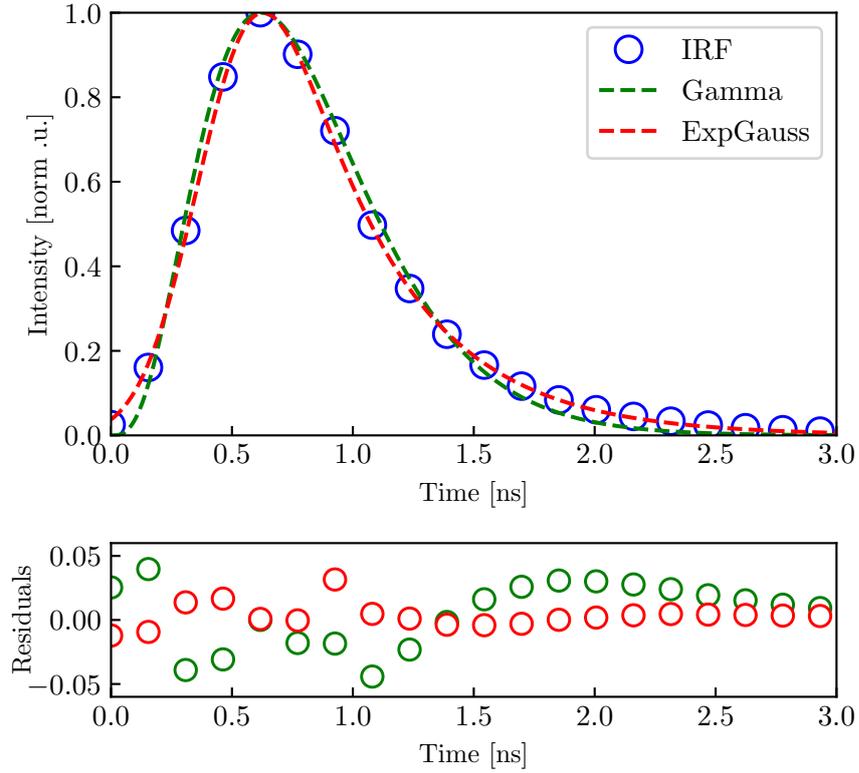
Figure 4.6.: The instrument response function and fit curves for modeling the IRF with a (green) Gaussian function and (red) an exponentially modified Gaussian distribution. The fit residuals show that while both fit curves represent the IRF fairly accurately, the red curve models the behaviour nearly perfectly. Mathematical definitions of the employed functions are given in the running text.

Modeling the IRF with an Exponentially-Modified Gaussian Peak

As the time trace of the pulsed laser diode has an exponentially decaying shape, the IRF itself follows the shape of a Gaussian peak convoluted with an exponential decay (see figure 4.5). This fact can be used for finding a suitable functional representation of the instrument response function.

For this, the Gaussian peak, which represents the timing jitter stemming from the employed PerkinElmer APD, is modeled as

$$R(t) = \frac{1}{\sigma\sqrt{2\pi}} \cdot exp\left(-\frac{1}{2}\left(\frac{t_0 - t}{\sigma}\right)^2\right) \tag{4.5}$$

Here, t_0 describes the mean of the Gaussian peak and σ^2 describes the width of the Gaussian function. The exponential decay stemming from the pulsed laser diode emission characteristics can be modeled as

$$D(t) = D_0 \cdot exp\left(-\frac{t}{\tau_1}\right) \tag{4.6}$$

The convolution of these two functions $IRF(t) = R(t) \otimes D(t) = \int_{-\infty}^{t} R\left(t - t'\right) \cdot D\left(t'\right) dt'$ is then used for fitting the instrument response function. Evaluating the convolution integral yields an analytical form for the IRF:

$$IRF(t) = \frac{D_0}{\sqrt{\pi}} \cdot exp\left(\frac{t_0 - t}{\tau_1} + \frac{\sigma^2}{2\tau_1^2}\right)\left(1 - erf\left(\frac{t_0 - t + \frac{\sigma^2}{\tau_1^2}}{\sqrt{2}\sigma}\right)\right) \tag{4.7}$$

In this context, the error function $erf()$ is defined as $erf(z) = \frac{2}{\sqrt{\pi}}\int_0^z e^{-t^2} dt$.

The result of a least squares fit of equation 4.7 to the measured instrument-response function is shown in figure 4.6. At first glance, there is a high degree of matching of the fitting curve with the experimental data, also the fit residuals illustrate this fact. Consequently, while the Gamma distribution represents the IRF reasonable well, the exponentially modified Gaussian distribution in equation 4.7 yields a nearly perfect match.

Fitting Measured Exponential Decay Curves

Following the argument of convoluted signals for fitting the IRF, the actually measured exponential decay curves in TCSPC have three contributions: the timing jitter from the measurement electronics $R(t)$, the exponentially decaying power emission from the pulsed laser diode $D(t)$ with the decay constant τ_1 and the actual fluorescence signal $S(t)$ from the measured optical system.

The overall signal $I(t)$, therefore, consists of a convolution of those three contributions. Using the fact that convolutions satisfy both the commutative as well as the associative law yields

$$I(t) = IRF(t) \otimes S(t) = (R(t) \otimes D(t)) \otimes S(t) = R(t) \otimes D(t) \otimes S(t) \tag{4.8}$$

This mathematical equation allows for the overall fitting procedure used for the determination of the excited state lifetime: First, the overall measured instrument response function is

fitted as described in the section above. The fit results are then subsequently used as fixed parameters in the fitting of the actual decay curves.

The convolution of the exponential decay curve for the laser diode behavior $D(t)$ with the fluorescence signal $S(t)$ can be analytically solved as

$$D(t) \otimes S(t) = \frac{\tau_1 \tau_0}{\tau_0 - \tau_1} \left(exp \left(-\frac{t}{\tau_0} \right) - exp \left(-\frac{t}{\tau_1} \right) \right) \tag{4.9}$$

Convoluting this expression with the Gaussian time behaviour $R(t)$ is lengthy but a mathematically rather simple procedure as the calculation reduces to convoluting a Gaussian with an exponential decay twice.

The complete analytical formula for the detection signal $I(t)$ of a measured exponential decay is then

$$I(t) = \frac{I_0}{\sqrt{\pi}} \frac{\tau_0 \tau_1}{\tau_0 - \tau_1} \left(exp \left(\frac{t_0 - t}{\tau_0} + \frac{\sigma^2}{2\tau_0^2} \right) \left(1 - erf \left(\frac{t_0 - t + \frac{\sigma^2}{\tau_0^2}}{\sqrt{2}\sigma} \right) \right) \right.$$
$$\left. - exp \left(\frac{t_0 - t}{\tau_1} + \frac{\sigma^2}{2\tau_1^2} \right) \left(1 - erf \left(\frac{t_0 - t + \frac{\sigma^2}{\tau_1^2}}{\sqrt{2}\sigma} \right) \right) \right) + y_0 \tag{4.10}$$

Here, the (arbitrary) proportional factor I_0 accounts for the fact that the measured IRF and decay curves have different overall count rates and y_0 represents a time-independent constant offset from e.g. dark counts of the APD modules or stray light.

On paper, fitting a measured TCSPC curve with this formula should reveal the true decay constant of the investigated optical system independent of any temporal disorder introduced by the imperfect measurement apparatus. Nonetheless, careful testing is indispensable before applying the algorithm on real data.

Testing the Fitting Procedure

In order to test the fitting accuracy of equation 4.10, synthetic TCSPC curves were created by convoluting the experimentally measured IRF curve from figure 4.6 with a pure exponential decay signal of chosen decay constant $\tau_{0,assumed}$. This synthetic data can then be employed to test the accuracy of the derived fitting algorithm by comparing the extrapolated fitted decay constant $\tau_{0,fitted}$ to the assumed decay constant $\tau_{0,assumed}$. Figure 4.7 displays the results of this comparison for fitting with a simple monoexponential decay (orange, equation 4.2) and the double-exponentially modified Gaussian function (blue, equation 4.10) in dependence of $\tau_{assumed}$. For better comparison, both functions were fitted on the falling flanks of the synthetic data curves only. As an example, the two insets in figure 4.7 show the fit results for an assumed lifetime $\tau_{0,assumed} = 1.000$ ns.

Obviously, the fitted lifetime $\tau_{0,fitted}$ for both fitting algorithms converge to the real value for larger assumed decay constants, i.e. they converge towards the assumed lifetime $\tau_{0,assumed}$.
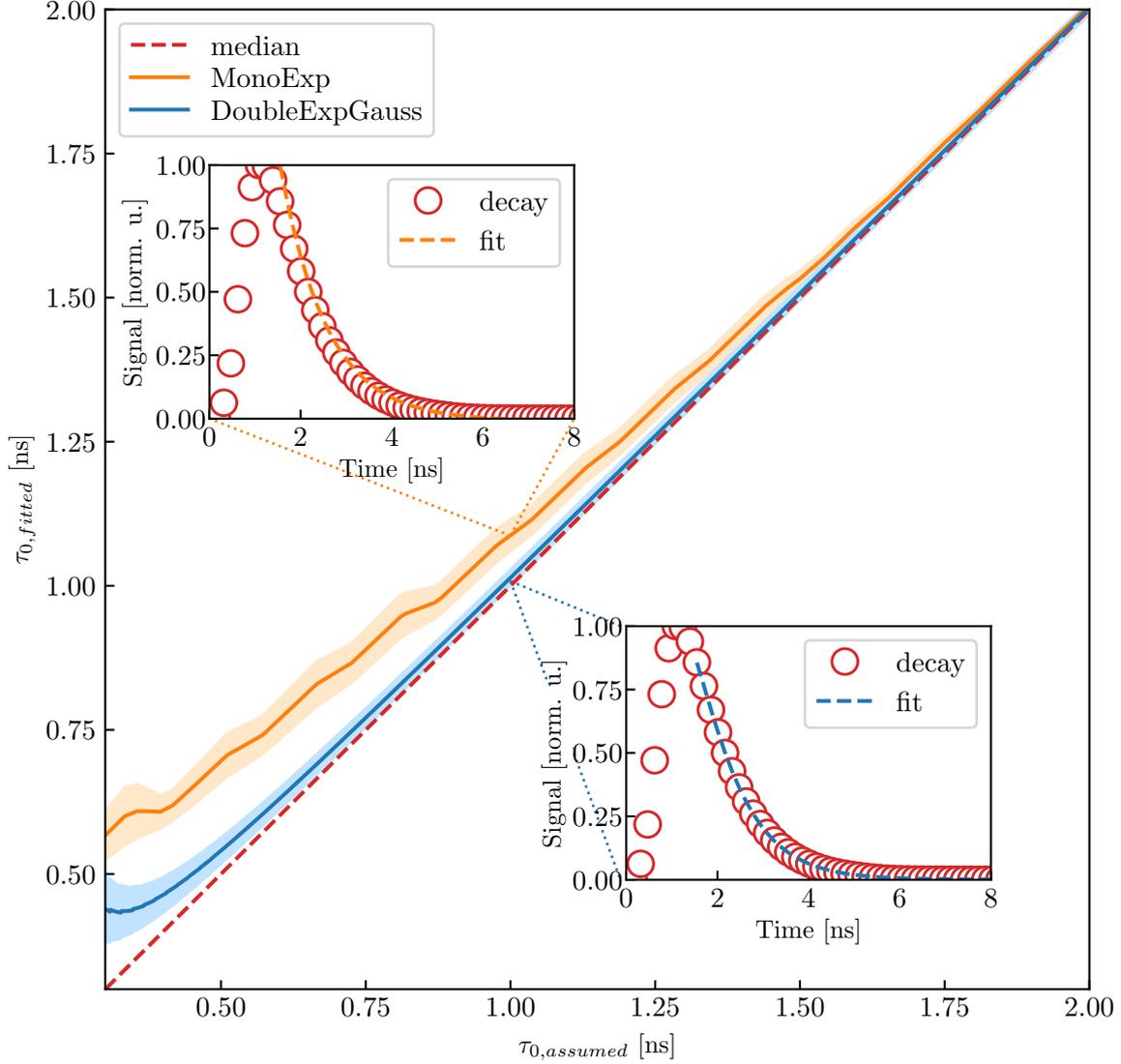
Figure 4.7.: Accuracy tests for fitting of synthetic TCSPC data using a monoexponential decay (orange, equation 4.2) and a double-exponentially modified Gaussian (blue, equation 4.10) for different decay lengths. The synthetic TCSPC experiment curves for the curve fitting were created by convoluting the measured IRF in figure 4.5(b) with a pure exponential decay of chosen decay constant $\tau_{0,assumed}$. The insert plots show the fit results for an assumed decay constant of $\tau_{0,assumed} = 1.000$ ns yielding a fit result of $\tau_{0,fitted_{DoubleExpGauss}} = (1.008 \pm 0.011)$ ns for the DoubleExpGauss function and $\tau_{0,fitted_{MonoExp}} = (1.087 \pm 0.028)$ ns for a fit using a monoexponential decay function.

This is rather unsurprising because the larger the decay constant of the optical system is compared to the timescale of the measurement uncertainty (i.e. the IRF), the less influential the measurement uncertainty becomes. Therefore, it is sufficient to fit TCSPC data with a simple exponential decay curve for optical systems with a decay constant of much larger

length scale than the IRF (in this case some ns). For this thesis, this fact is employed for analyzing time-resolved measurements of the excited state lifetime of the NV^- state in section 5.2.3.

For very fast optical systems like the excited state of the silicon-vacancy center with a typical lifetime of about 1 ns (compare section 5.3), this simplification is not valid. Here, the simple monoexponential (equation 4.2) fit results deviate strongly from the correct values. Additionally, a step-like course occurs that is a result of the finite time binning of 164 ps, resulting in unsteady sampling of the decay curve. In contrast to this rather unsatisfactory performance, the more refined fitting with a double-exponentially modified Gaussian function (equation 4.10) yields much better results. Apart from very short $\tau_{0,assumed}$, where the decay constant is faster than the decay of the IRF, the obtained fit values agree nearly completely with the assumed ones. The insert of figure 4.7 shows the synthetic decay curve for an assumed decay constant of $\tau_{0,assumed} = 1.000$ ns, which corresponds to the typical excited state lifetime of a SiV center. Here, the least-squares fit reveals a fitted decay constant of $\tau_{0,fitted} = (1.008 \pm 0.011)$ ns, which corresponds nicely to the expected value.

4.4. Autocorrelation Measurements

Another type of temporal measurements regularly performed in course of this thesis are second-order autocorrelation measurements of emitted fluorescence light in order to directly measure the photon statistics of an optical system (see section 5.2). From their initial inventors, this type of optical intensity-correlation measurement is also called a *Hanbury Brown and Twiss* (HBT) measurement. As this experiments also involves temporally resolved detection of incoming photons and subsequently correlates the outcome, the timing uncertainty of the detection system influences the result of a measurement as well. Therefore, a similar analysis of its influence is necessary.

For this, we first assume a perfect single-photon source. For such a system, Poissonian statistics tells that the measured second-order correlation ($g^{(2)}$) function features an expected value of zero at $\tau = 0$, that is at zero time difference between the two detectors. In general, the second-order correlation function can be written as [8]

$$g^{(2)}(\tau) = \frac{\langle I(t) I(t+\tau)\rangle}{\langle I(t)\rangle \langle I(t+\tau)\rangle} \tag{4.11}$$

Here, τ represents the time difference between two events. Colour centers in diamond typically have, apart from the radiative transition with lifetime τ_0, and additional non-radiative long-living shelving state with lifetime τ_S. Compare chapter 5 for more details. By analyzing the rate equations, an analytical expression for autocorrelation measurements can be found [19]

$$g^{(2)}(\tau) = 1 + c_1 \cdot e^{-\frac{\tau}{\tau_0}} + c_2 \cdot e^{-\frac{\tau}{\tau_S}} \tag{4.12}$$

Here, the proportionality factors c_1 and c_2 determine the relative relative coupling strengths of the excited state to the ground and shelving state. The excited state lifetime τ_0 of the single-photon emitter influences the slope of the $g^{(2)}$ function [21], while the longer lifetime of

the shelving state τ_S influences the g$^{(2)}$ curve only for larger time differences. For an analysis on the influence of small timing uncertainties, the shelving state can, therefore, be neglected ($\tau_S = 0$). The resulting curve then represents a two-level system.

When trying to measure such an ideal second-order correlation curve temporally resolved, the previously discussed instrument-response function influences the temporal measurements and, therefore, modulates the outcome of the experiments. The overall expected curve $S(t)$ is then a convolution of the ideal g$^{(2)}$ curve and the IRF$_{\text{HBT}}$:

$$S(\tau) = g^{(2)}(\tau) \otimes IRF_{HBT}(\tau) \tag{4.13}$$

In real measurements, $S(t)$ can deviate strongly from the ideal case. Compare also similar investigations in [73, 74]. The instrument-response function IRF$_{\text{HBT}}$ for autocorrelation measurements differs to that for TCSPC measurements in the previous section (compare equation 4.7). The reason for this is that two detectors A and B are employed in the experiment. Both of them have their own distinct Gaussian-like timing uncertainties $R_A(t)$ and $R_B(t)$, which can be modeled similar to equation 4.5. The resulting instrument-response function is then a temporal convolution of the two Gaussian functions

$$IRF_{HBT} = R_A(t) \otimes R_B(t) \tag{4.14}$$

In order to evaluate the influence of the temporal jitter on autocorrelation measurements, the curves for perfect (*ideal*) g$^{(2)}$ function according to equation 4.12 and the expected (*real*) curves according to equation 4.13 are compared to each other. The expected curves were calculated by numerical convolution of two Gaussian functions according to equation 4.5 with a full-width at half-maximum (FWHM) of 540 ps each and the ideal g$^{(2)}$ function in equation 4.12. Figure 4.8 presents the difference at $\tau = 0$ between the real and ideal case for different assumed excited state lifetimes τ_0 relative to the temporal timing uncertainty of $FWHM = 540$ ps.

It is immediately visible that the realistically measurable minimal $g^{(2)}(\tau = 0)$ deviates strongly from zero for short lifetimes, an effect similar to the influence of the IRF on the excited state lifetime measurements in figure 4.7. This is not surprising due to the nature of the correlation measurements: Around $\tau = 0$, very small timing differences between the two detectors have to be resolved. If the lifetime τ_0 of the system is of the same order as the timing uncertainty, the uncertainty simply blurs the dip at $\tau = 0$ as the timing difference cannot be resolved accurately. An example for this difference between an ideal g$^{(2)}$ curve and the blurred curve is presented in the insert of figure 4.8, which illustrates the case of an excited state lifetime double the FWHM uncertainty of one detector.

For this thesis, mainly nitrogen-vacancy centers were investigated via autocorrelation measurement. When incorporated in nanodiamonds, their excited state lifetime is typically of the order of a few 10 ns (5.2.3), much longer than the timing uncertainty of the employed detection system, which is in the order of $FWHM = 0.5$ ns. Therefore, the influence of the timing jitter on $g^{(2)}$ measurements of NV-centers can be neglected. For silicon-vacancy centers, whose lifetimes are much smaller and in the order of 1 ns, the effect of the detection time uncertainty on the g$^{(2)}$ measurement cannot be neglected. Here, blurring of the $g^{(2)}(\tau = 0)$ dip would be
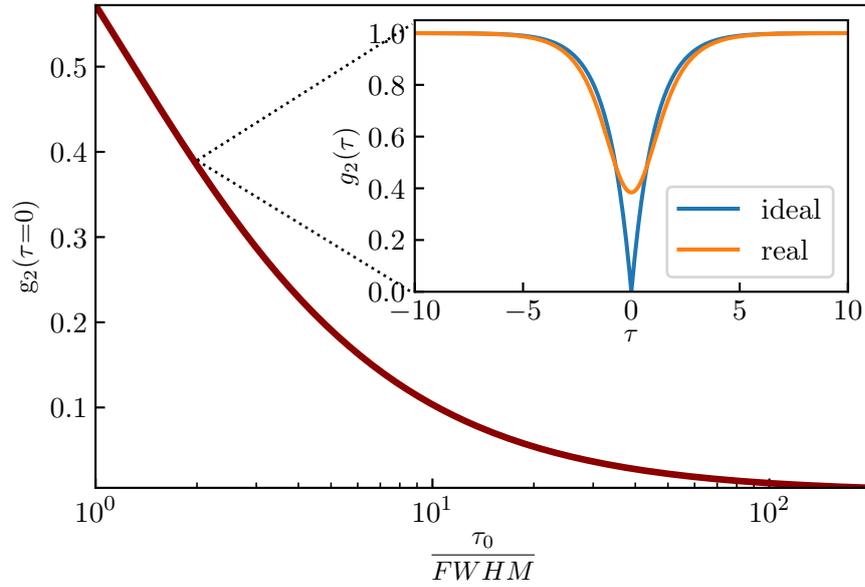
Figure 4.8.: Test of the influence of timing jitter on autocorrelation measurements for different assumed decay constants τ_0 relative to the FWHM of the timing uncertainty. While the ideal $g^{(2)}$ curve features a value of zero at $\tau = 0$, the real curve dip is damped due to the influence of the detection timing uncertainty. An example for this difference between the ideal and realistic case is given in the insert plot.

much stronger and would have to be addressed. This could be done by e.g. analytically convoluting the pure second-order correlation function 4.12 with the instrument-response function in equation 4.14.

There is one simplification at least. Electrons behave ... in exactly the same way as photons; they are both screwy, but in exactly in the same way.

(Richard P. Feynman)

Chapter 5.

Colour Centers in Diamond

Optical information processing based on single quanta of light requires efficient emitters of single photons. Over the years, many different single-photon emitters have been found and investigated for their possible use [75]. Most of them share the same basic physical principle of creating single photons: Two energetically separated electronic states, where an electron transfers its potential energy gain from decaying from the energetically higher to the lower state to an emitted single photon. The physics and therefore the working principles behind these discrete energetic levels, however, can vary greatly and affects the mode of operation and/or the usability for certain applications.

One particular type of single-photon emitters are energetically localized states in a semiconductor or insulator environment. Here, the energetic band gap formed by the interaction of the constituent atoms provides the means for creating confined bound electronic states, which can be optically or electrically excited. In particular, these bound states can be formed by introducing additional dopant atoms into the material, which locally alter the electronic structure.

This chapter introduces two varieties of so-called *colour centers* in diamond, which are dopant sites in a diamond host lattice. As the name suggests, they can act as optically active systems, which - depending on the dopant atom - emit light at a certain spectral range. After a brief introduction into the unique properties of diamond, the *nitrogen-vacancy center* and the *silicon-vacancy center* are presented. For both colour centers, the electronic structure and the resulting optical properties are explained with an emphasis on their usage in small nanometer-sized diamond host lattices, so-called *nanodiamonds*.

5.1. Diamond as a Material

Diamond has some unique properties, which makes it stand apart from other naturally occurring materials, and is well known for its hardness and thermal conductivity [76]. It is a metastable form of carbon atoms arranged in a crystalline lattice with graphite being the other, thermodynamically preferred crystal structure. From a crystallographic point of view, the diamond crystal is composed of a *face-centered cubic* (fcc) lattice structure with a two-atomic basis. Figure 5.1(a) illustrates the unit cell configuration of pure diamond with the basis pair atoms depicted by a gray and red atom each.

The packaging structure of the diamond lattice is caused by the sp^3 hybridization of the constituent carbon-carbon bonds and results in tight binding between the crystal atoms. One

(a) Unit cell in diamond   (b) Nitrogen-vacancy center   (c) Silicon-vacancy center
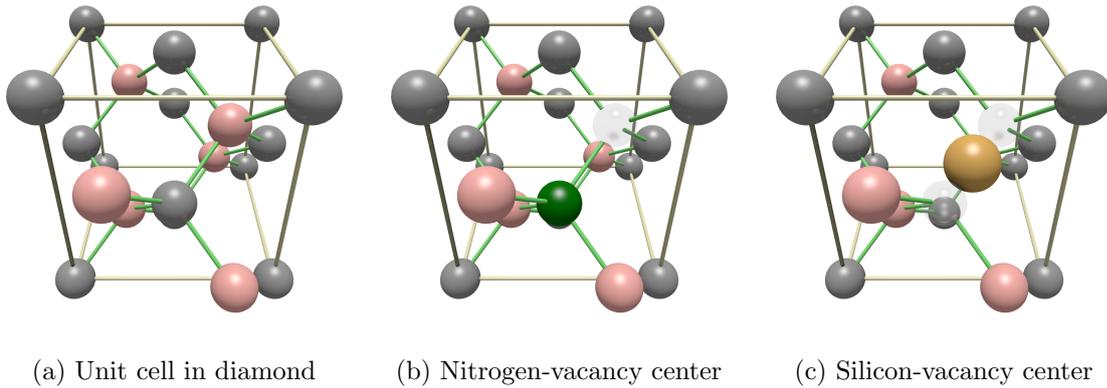
Figure 5.1.: The lattice structure of diamond in the presence of defects forms optically active localized states. (a) The unit cell configuration of diamond as a fcc lattice with a two-atomic basis, represented by a gray and red atom each. (b) A nitrogen dopant atom (green) accompanied by a vacancy site form the nitrogen-vacancy center. (c) Silicon as a dopant atom resides in an intermediate lattice place and is accompanied by two vacancies.

consequence of the high binding strength is the large energetic band gap of diamond at about 5.5 eV [77], which renders a pure diamond crystal colourless in the visible spectrum. However, many naturally occurring diamonds exhibit a distinct colour. So where does this colouring stem from? The reason are defects and impurities, which break the crystal structure and create localized optically active states. For diamond, hundreds of intrinsic (no impurity atom) and extrinsic (one or more dopant atoms) are known [78].

Using defect centers in diamond as an emitter for single quanta of light has some key advantages. Firstly, the diamond crystal is in itself stable down to the nanometer level, which makes it possible to break bulk diamond down to very small crystal sizes, also called *nanodiamonds*. Additionally, due to the large band gap, electronically trapped states formed by defect sites are shielded from both the valence and conduction band, making the system less susceptible to carrier loss from thermal excitation. In contrast to other semiconductor based single-photon emitters, many defect sites in diamond are well-known to operate also at ambient temperatures.

By choosing the type of dopant atom, different emission wavelengths and other electronic properties like the electron spin-coherence or the coupling to phonons can be influenced. Of the many known choices, two were employed for this thesis and, therefore, shall be explained in detail in the following sections. One is based on a nitrogen dopant, called the *nitrogen-vacancy* (NV) center, the other is silicon-based and thus called the *silicon-vacancy* (SiV) center.

5.2. The Nitrogen-Vacancy Center

From all the colour centers known to this date, the arguably most famous one is the nitrogen-vacancy center, which has been known to be usable as a stable room-temperature single-photon source for many years [19]. The reasons for this popularity as a subject of investigation are

manifold, one major reason is that the NV center is naturally occurring and known to provide yellowish colour to diamonds. At the atomic scale, the NV center if formed by substituting a carbon atom by a nitrogen one (compare figure 5.1(b)). As the nitrogen atom is larger than its carbon counterpart, it is energetically favorable that the dopant atom is accompanied by a single vacancy site. Due to the asymmetric arrangement, the center exhibits a permanent electric dipole, which makes the system susceptible to external electric fields. This feature can be employed for tuning the NV center via the DC stark shift [79]. However, it makes the system also erratic when fluctuating electric fields are present, a phenomenon called *spectral diffusion* [80]. For NV centers in nanodiamond, where the surface is in proximity to the colour center, the fields are mainly caused by local electric charges at the surface [81].

5.2.1. Energetic Level Structure

The complex of a nitrogen dopant atom accompanied by a vacancy site creates an energetically localized state within the band gap of the diamond crystal. Figure 5.2(a) illustrates the resulting level structure of the NV system with its two distinct charge states, a neutral NV^0 state and a negatively charged NV^- state [82].

(a) Level scheme of the NV center (b) Emission spectrum of the NV center
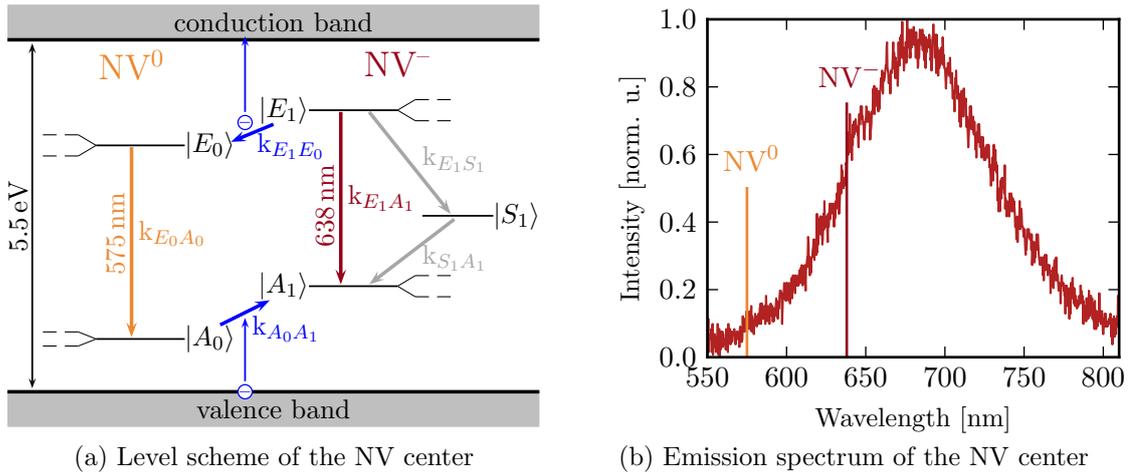
Figure 5.2.: (a) The level structure of the nitrogen-vacancy center in diamond with its two optically charged states (neutral and negative) and the additional shelving state for the NV^- state. (b) Typical photoluminescence spectrum of a single nitrogen-vacancy center hosted in a nanodiamond excited off-resonantly at 532 nm, which shows that typically both charge states contribute to the overall emission.

Both charge states show a characteristic direct transition line from the excited state $|E_0\rangle/|E_1\rangle$ to the ground state $|A_0\rangle/|A_1\rangle$ at 575 nm for the neutral and 638 nm for the negative charge state, which is called the *zero-phonon line* (ZPL). Typical lifetimes for the excited states are in the order of several to tens of nanoseconds. Moreover, the NV^- state also has a long-living shelving state $|S_1\rangle$, which itself consists of two energetic levels split by 1.19 eV or 1.042 μm. As the wavelength of this transition is not detected in the experimental setups employed for this thesis, it can be safely neglected. An additional metastable, long-living shelving state has also been found for the neutral charge state [83], however, its overall impact on the dynamics

of the system is small and can, therefore, be ignored for this study [84]. High-resolution spectroscopic investigations of the nitrogen-vacancy center at cryogenic temperatures would show that for each charge state both the ground and the excited states are further split into $m_s = 0$ and $m_s = \pm 1$ spin states each [85]. In this regard, of particular importance for many experiments is the long spin-coherence time of the NV$^-$ ground state in the order of milliseconds at low temperatures, which can be optically initialized due to a preferential decay into the $m_s = 0$ state via the $|S_1\rangle$ shelving state [86].

5.2.2. Emission Spectrum and Charge State Switching

When investigating nitrogen-vacancy centers with spectroscopic tools, very often both zero-phonon lines and the corresponding emission sidebands can be observed. The reason for this is *photochromism*, i.e. optically induced charge state switching between the neutral NV^0 and the negative NV$^-$ state [87, 81] by means of two-photon processes to either capture an electron from the valence band (transition $k_{A_0 A_1}$) or releasing an electron to the conduction band (transition $k_{E_1 E_0}$). When performing photoluminescence measurements with excitation light, which can drive both charge state transitions like a laser at 532 nm, the emission spectrum results in a convolution of the emission spectra of the NV^0 and NV$^-$ states. Figure 5.2(b) illustrates a typical emission spectrum of a NV center at room temperature, which shows a broad emission band spanning from about 575 nm, the ZPL of the neutral charge state, to about 800 nm. The cause of the strong broadening of the direct emission line is the coupling of the electronic states to phonon modes present in the diamond crystal, which gives rise to the large co-called *phonon sidebands* [19].

5.2.3. Resonant Excitation at Room Temperature

For a better understanding of the dynamics behind the charge state switching of the NV center at room temperature, a temporally resolved spectral analysis of the system was performed. To this end, selective resonant excitation of the NV$^-$ transition ($k_{E_1 A_1}$ in figure 5.2(a)) in combination with off-resonant reinitialization of the state was performed at room temperature on nanodiamonds hosting a single NV center. Figure 5.3 shows a time trace of the fluorescence recorded while performing one excitation sequence. For the analysis, the fluorescence detection was restricted to emission stemming from the negative charge state only. To this end, the spectral acceptance window was required to be limited to wavelengths beyond 680 nm. This cutoff wavelength is larger than many previous experiments, which often set the cutoff at about 650 nm [88, 89]. Recent two-photon absorption experiments, however, supported the choice of a much longer cutoff at 680 nm [90].

The sequence starts by resonantly exciting the NV$^-$ transition using a home-built pulsed laser source at 638 nm with a bandwidth below 500 MHz [65]. After several resonant excitations, the fluorescence response drops as the system switches into the neutral charge state. The remaining emission spikes in the measurement time trace stem from residual inelastic scattering of the excitation laser. By analyzing the decay curves (compare the inset in figure 5.3), both the excited state lifetime as well as the number of possible resonant excitations could be determined. Statistical analysis showed that on average, 6 to 10 single pulses were sufficient to induce the switch to the neutral charge state. It is important to note here that careful
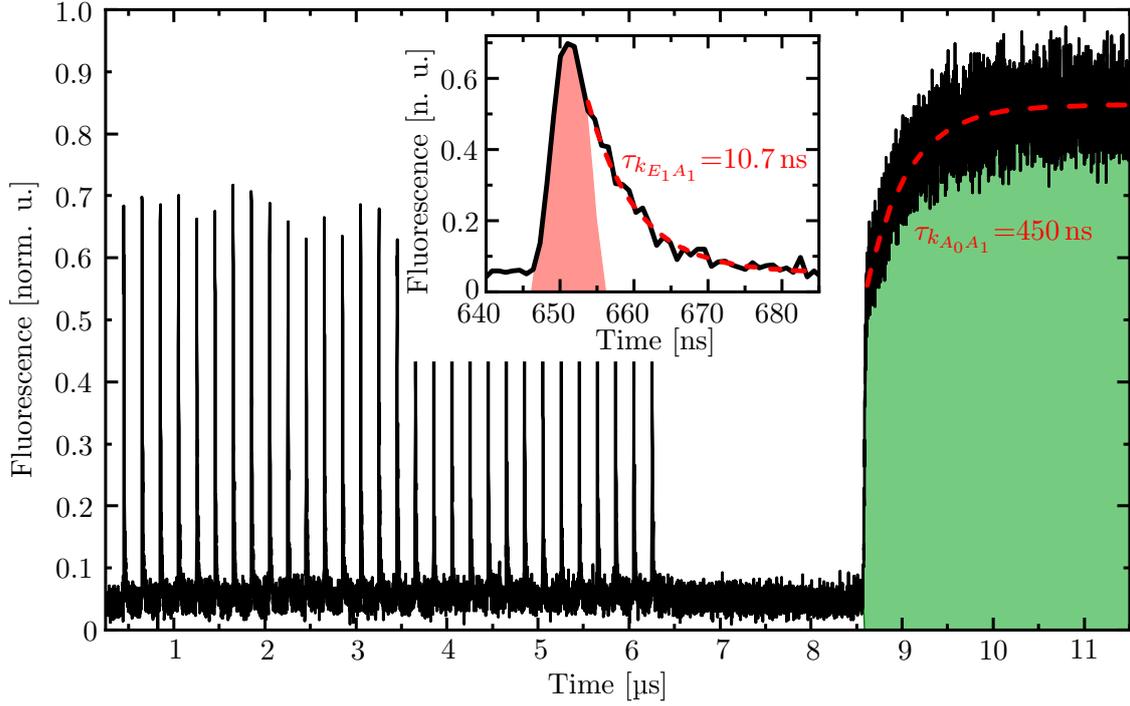
Figure 5.3.: Experimental sequence for the resonant excitation of the negative charge state of the NV center. After pulsed resonant excitation of the NV$^-$ transition, which also induces photochromism into the NV^0 state, the system is reinitialized by off-resonant excitation at $532\,\mathrm{nm}$.

tuning of the laser emission to the NV$^-$ line is necessary. As this line can be shifted, measurement tries with varying laser frequency were necessary for an optimal excitation efficiency. In course of these optimization runs, the spectral width of the optical $k_{E_1 A_1}$ transition at room temperature could be determined as well and was found to be typically in the range of $1\,\mathrm{nm}$ for nanocrystals with sizes of several tens of nanometers.

In order to prove single-photon emission from the resonant excitation cycles, the second-order correlation function was measured. For this Hanbury Brown and Twiss (HBT) type of experiment, the detected fluorescence was divided and recorded by two avalanche photodiodes. The correlation between events from the two detectors then directly displays the statistics of the emission [8]. Figure 5.4(a) shows the result of this experiment: For zero time difference between the two detectors, the second-order correlation function shows a value of $g^{(2)}(\tau = 0) \approx 0.10$, indicating clear single-photon emission. Additionally, two peaks at $\tau = \pm 6\,\mathrm{ns}$ are present, which are a result of optical cross-talk between the two detectors. Compare section 4.1 for further details about this phenomenon.

For the purpose of reinitializing the system to the negative charge state, a single long off-resonant excitation pulse at $532\,\mathrm{nm}$ was employed. By analyzing the onset of the emission from this pulse, the reinitialization time for changing from the neutral to the negative charge state could be determined. Figure 5.4(b) shows the onset times for different laser excitation powers. Depending on the laser power, this time was found to be in the order of several hundred ns to $1\,\mu\mathrm{s}$ for moderate laser powers of about $1\,\mathrm{mW}$. The power-dependence clearly

(a) Measured second-order correlation function for selective resonant excitation of the NV$^-$ state

(b) Power-dependence of the reinitialization time
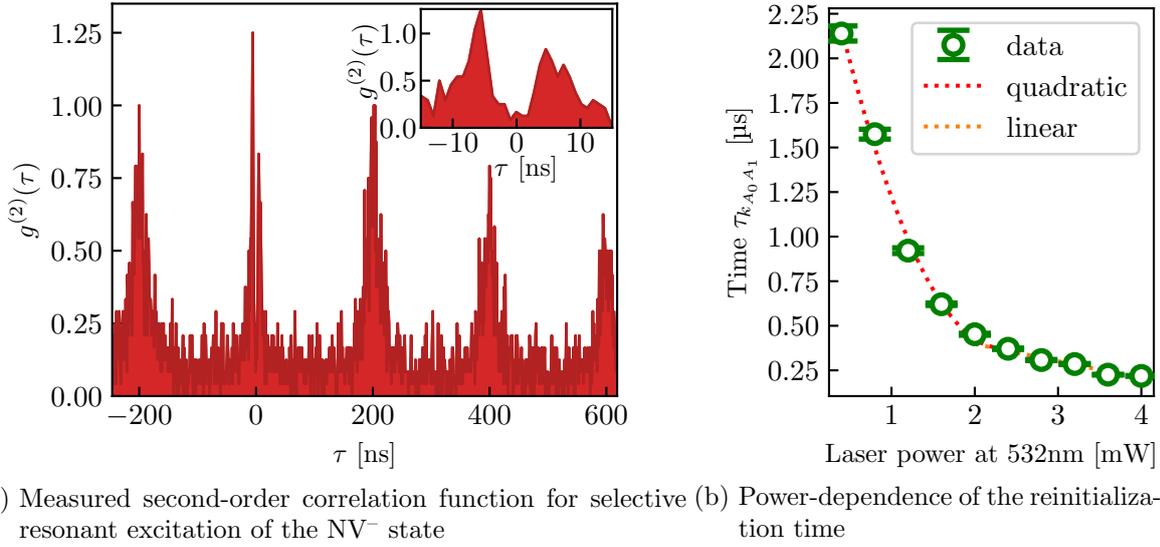
Figure 5.4.: Characterization of the resonant excitation scheme in figure 5.3. (a) Measured second-order correlation function of light emitted after pulsed resonant excitation of the NV$^-$ state. (b) Measured power-dependence of the time needed to reinitialize system to the NV$^-$ state using off-resonant laser light at 532 nm.

shows a quadratic behaviour for lower excitation powers, which hints at a two-photon process for the charge-state conversion (compare also [91]). For higher laser powers above saturation at about 2 mW, the reinitialization time decreases linearly. This might be attributed to a saturation of the excited states, which renders the recapture of an electron from the valence band linearly dependent on the excitation power. Further information about this experimental study can be found in [92].

5.3. The Silicon-Vacancy Center

The silicon-vacancy center is - as the name suggests - formed by introducing a single silicon dopant atom in the diamond crystal. Figure 5.1(c) illustrates the resulting lattice structure, which is comprised of the silicon atom positioning itself in an intermediate place between two crystal sites. Consequently, the SiV center is formed by the silicon atom accompanied by two vacancies [93]. This symmetric arrangement has the key advantage of producing no permanent electric dipolar moment, by which the SiV system is immune against spectral diffusion induced by external electric fields [94].

The internal level structure of the negatively charged silicon-vacancy center is illustrated in figure 5.5(a) with the zero-phonon line being positioned at about 738 nm [95]. Both ground and excited state are split into $|m_s\rangle = 0$ and $|m_s\rangle \pm 1$ states separated by 47 GHz and 258 GHz, respectively, which results in four distinct emission lines [96]. Typically, only the negative charge state is optically active. Photochromism, i.e. the switching of the charge state by optical excitation between the negatively and the neutrally charged silicon-vacancy

(a) Level scheme of the SiV$^-$ center

(b) Emission spectrum of the SiV$^-$ center

(c) Emission spectrum line broadening for different temperatures
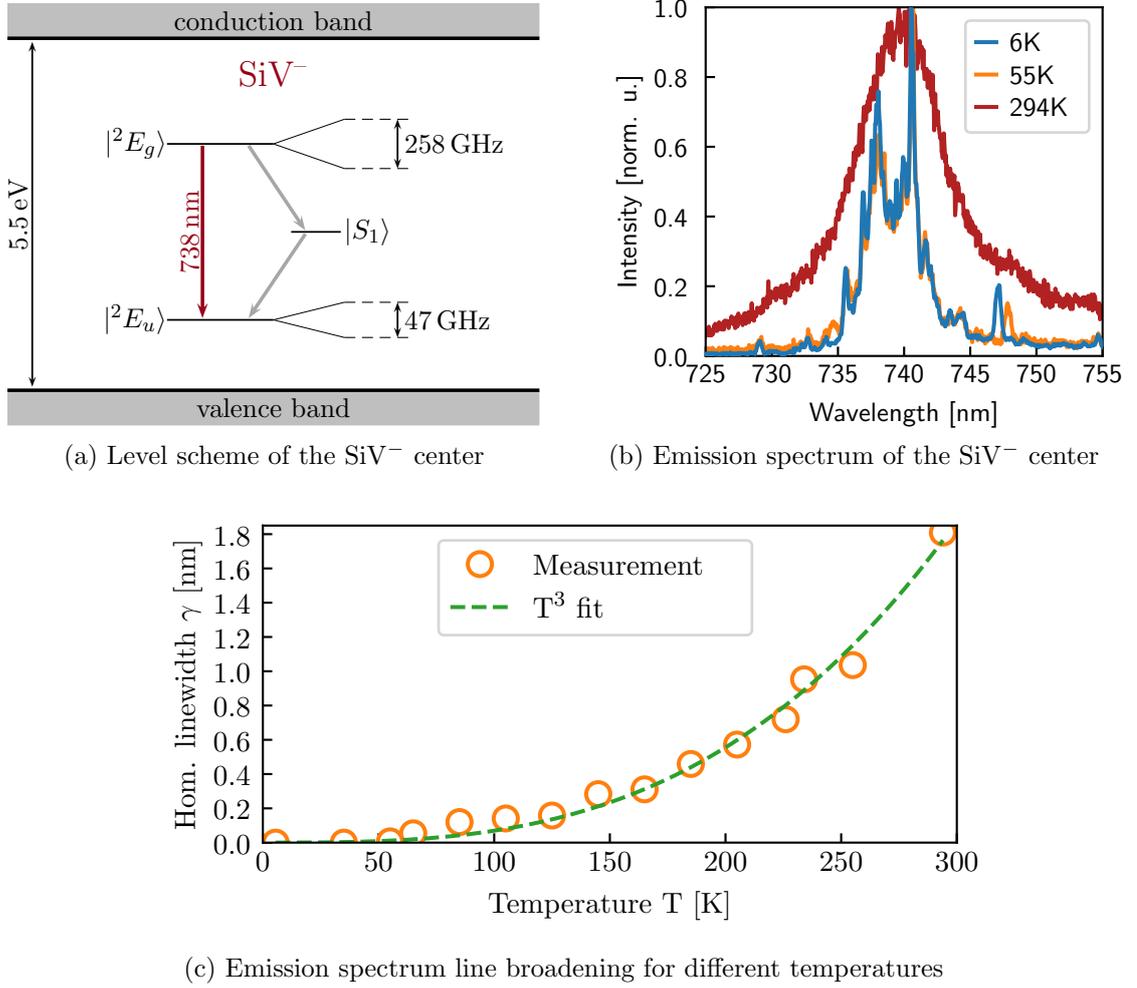
Figure 5.5.: Level structure and temperature-dependent emission effects of the negatively charged silicon-vacancy center. (a) Energetic level structure of the SiV-center with split ground state and excited state leading to four emission lines at 738 nm. (b) Typical emission spectra of an ensemble of SiV centers at different temperatures. (c) Temperature-dependence of the homogeneous linewidth γ, which follows a cubic temperature-dependence while the inhomogeneous line broadening is temperature-independent.

center state, is only possible by illumination with UV light or thermal excitation of charge carriers by strong heating [97]. Similar to the NV-center, an additional long-living shelving state $|S_1\rangle$ with a typical lifetime of several nanoseconds is also present [98].

What makes the silicon-vacancy center stand apart from many other colour centers is its high *Debye-Waller factor*, which describes the proportion of released light being emitted directly in the zero-phonon line. For the SiV$^-$, this can exceed 70% at room temperature, with some claiming even higher numbers [78, 99]. For this reason, it is a prime choice when creating single-photon sources from colour centers in diamond. One main drawback for their usage

is that SiV centers are not naturally occurring like the NV center but need to be artificially created either by ion implantation [95] or by chemical growth [98]. This drawback is especially true for silicon-vacancy centers in nanodiamonds as the SiV center tends to become unstable in diamond crystals with sizes below 100 nm [100].

In this thesis, nanodiamonds grown via *chemical vapor deposition* (CVD) were employed, which on average, hosted several SiV centers. For a better understanding of their dynamics, they were investigated spectrally. The typical emission spectrum of such a colour center ensemble for several diamond temperatures is presented in figure 5.5(b). The spectra were recorded using a home-built low-temperature photoluminescence setup built during this thesis (see [101] and [102] for more information about the experimental details). At low temperatures, many single emission lines are visible, which are shifted relative to one another. The reason for this behaviour is the non-perfect crystalline host environment of the nanodiamond, which induces local strain to different colour centers [78]. At ambient temperatures, the single emission lines cannot be resolved anymore as the homogeneous line broadening increases.

For a better understanding of the dynamics behind the emission of such a SiV ensemble, measurements of the emission spectrum were performed for different temperatures from 6 K to 293 K. The analysis of this investigation is analogous to [103] and distinguishes between the inhomogeneous line broadening, which is induced by stress in the crystal and homogeneous line broadening of the zero-phonon lines due to phonon interaction. The inhomogeneous contribution can be approximated by a Gaussian profile $I_G(\lambda)$

$$I_G(\lambda) = \frac{A}{\sigma\sqrt{\pi/2}} \cdot e^{-2\frac{(\lambda-\lambda_c)^2}{\sigma^2}} \tag{5.1}$$

with amplitude A, central wavelength λ_c and width σ and is assumed to be temperature-independent. The homogeneous line broadening of the single ZPLs is mainly caused by electron-phonon interaction and follows a Lorentzian lineshape with γ as the linewidth

$$I_L(\lambda) = \frac{2A}{\pi} \cdot \frac{\gamma}{4\left(\lambda-\lambda_c\right)^2 + \gamma^2} \tag{5.2}$$

The overall shape of the ensemble emission can then be approximated by a Voigt profile, which convolutes the Gaussian profile I_G and the Lorentzian shape I_L, and which reads as [98]

$$I(\lambda) = \frac{2Aln(2)}{\pi^{\frac{3}{2}}} \frac{\gamma}{\sigma^2} \int_{-\infty}^{\infty} \frac{e^{-t^2}}{\left(\frac{\sqrt{ln(2)}\gamma}{\sigma}\right)^2 + \left(\frac{\sqrt{4ln(2)}(\lambda-\lambda_c)}{\sigma} - t\right)^2} dt \tag{5.3}$$

In order to obtain the temperature-dependent evolution of the homogeneous linewidth γ, equation 5.3 was fitted to measured emission spectra of a nanodiamond for different temperatures. To this end, for the fit at the lowest temperature at 6 K, the homogeneous line broadening γ was assumed to be zero, which provided a value for the inhomogeneous line broadening of $\sigma = 2.9\,nm$. This value was then assumed to be constant for the remaining

measurements at higher temperatures. Figure 5.5(c) illustrates the evolution of the homogeneous linewidth γ, which stays nearly zero for temperatures below $70\,\mathrm{K}$ and subsequently follows a cubic dependence on the temperature [104].

The temperature-dependent measurements illustrate that silicon-vacancy centers do not have to be kept at liquid helium temperatures to achieve nearly ideal lifetime-limited emission profiles. Keeping samples at temperatures below $10\,\mathrm{K}$ requires expensive helium-cooling equipment. Instead, liquid nitrogen temperatures at about $77\,\mathrm{K}$, which are much less expensive to operate, are already enough to obtain SiV emission shapes nearly unaffected by phonon coupling.

Chapter 6.

Experiments with Bullseye Resonators

In this chapter, the main results of simulations and experiments on bullseye resonator structures hosting an emitting diamond nanocrystal in its center are presented. As described in chapter 3, this nanoplasmonic structure should induce an emission profile, which is much more oriented in forward direction as compared to the case of a nanoemitter positioned on a planar fused silica substrate, thereby increasing the collection efficiency and usability of light emitted by the nanoemitter.

This claim is put to the test by combining experimental studies and corresponding simulation results. After summarizing and emphasizing on the design of the fabricated and assembled bullseye resonator structures, measurements on the emitted farfields and the emission dynamics of different planar ring resonators were investigated and analyzed.

6.1. Design Choices for Bullseye Structures

Some general design rules and the basic concepts of plasmonic resonators consisting of concentric rings on a reflecting substrate are already discussed in section 3.3. The basic outcomes of these findings are that the metallic rings need a ring spacing slightly smaller than the emission wavelength of the employed emitters and a reflecting substrate to redirect light emitted towards the substrate, which would otherwise be lost and seriously lower the collection efficiency.

Apart from these general rules, some additional design choices and elementary experimental investigations are necessary. In particular, these choices concern the two main components of the final bullseye resonator structure, namely the metallic rings themselves as well as the underlying reflecting substrate. The question of finding a suitable substrate type is treated in detail further on in section 6.3.1 with the conclusion that for redirecting light from a colour center hosted in a nanodiamond, a dielectric substrate offers some advantages when compared to a metallic base film typically used in bullseye resonator structures.

This section deals with the question of choosing the most suitable metal for the ring structure. Their typical form is presented in figure 6.1(a), which displays scanning electron microscope (SEM) images of fabricated bullseye structures. When fabricating these metals in a top-down lithography based approach, which is described in detail in section A.1, two main demands on the deposited material must be fulfilled: Firstly, the material must produce a smooth and even surface for low-loss propagation of surface plasmon polaritons (SPPs). Secondly,

the outer ring edges, where SPP modes are converted into free space modes, must be sharp. Thermal evaporation at high vacuum meets both demands and produces smooth films for various metals if it is applied with correct parameters. In this regard, another very practical necessity is the availability of the metal in such an evaporation machine.
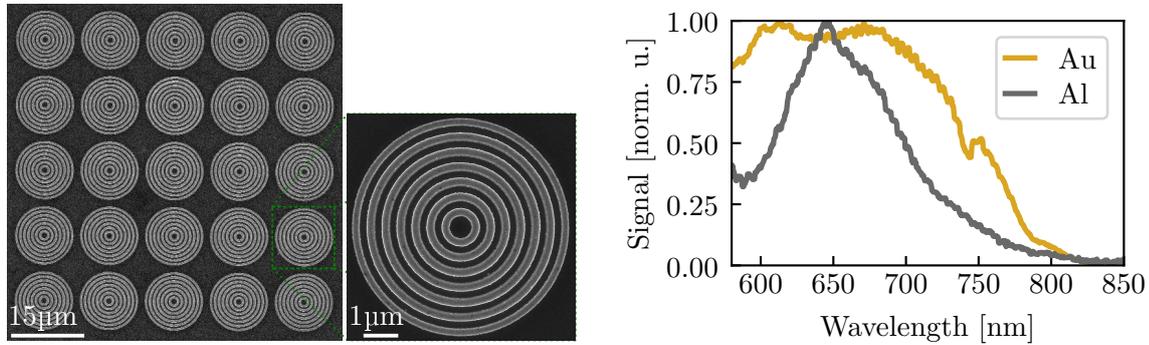
(a) SEM pictures of investigated bullseye resonator arrays.

(b) Comparison of normalized autofluorescence spectra for gold and aluminium structures.
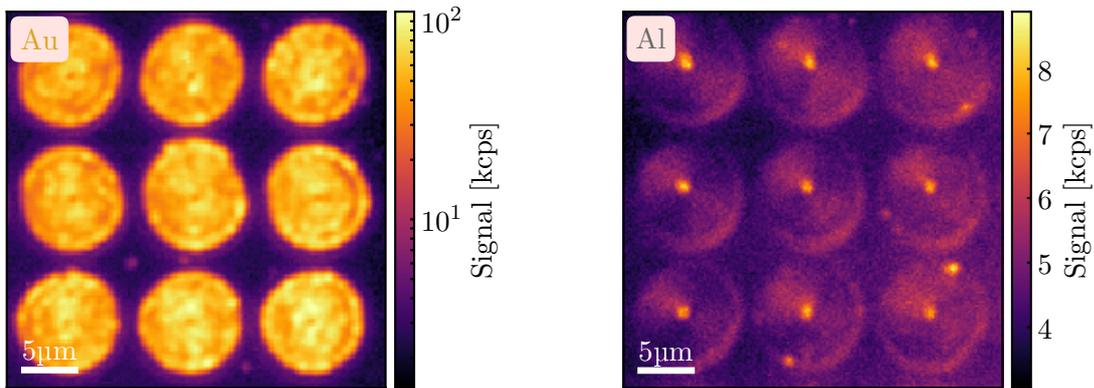
(c) Mesured autofluorescene of gold bullseye resonator arrays.

(d) Mesured autofluorescene of aluminium bullseye resonator arrays.

Figure 6.1.: Investigation of geometrically identical fabricated bullseye structures for tests of suitable metals using confocal photoluminescence spectroscopy (PLS) with 1.0 mW of excitation power at 532 nm. (a) SEM images of investigated metallic bullseye resonator arrays. The ring material is either gold or aluminium, each deposited by evaporation. (b) Measured normalized emission spectra of PL emission for both investigated metals. (c) and (d) High-resolution PLS maps for bullseye structures made from gold and aluminium. The signals are summed over the emission spectrum beyond 550 nm.

Another very fundamental demand on the employed metal is its plasmonic activity. For plasmonic devices operating in the visible and near-infrared, mainly two metals are used to this end: silver and gold. The restriction to these two materials mainly lies in their high electric conductivity and, therefore, strong plasmonic resonances in the spectral region of interest. Of the two, silver has the highest plasmonic strength in the visible spectral region. However, it also has the big disadvantage of being very susceptible to oxidation: silver structures very

quickly oxidize from the surface into the bulk of the material, which renders the structure unusable for plasmonic tasks [29, 105]. For this reason, gold is the de facto standard material for plasmonic structures, partly also due to its chemical inertness, which makes it ideal for biological applications.

However, gold has the major disadvantage of strong autofluorescence, which spans a broad spectral range. The reason for this behaviour is a very flat valence d-band, which allows scattering of holes into various momentum states. When recombining with excited electrons, this leads to a spectrally broad emission [106]. In this regard, other metals might be advantageous, especially non-nobel metals should exhibit much smaller autofluorescence as their band structure often doesn't feature the flatness of the valence d-band of noble metals. One such candidate is aluminium, which is most commonly used in plasmonics in the ultraviolet region [29], though it also features quite strong plasmonic responses in the visible and near-infrared. See section 2.3.2 for further details and comparisons between the different plasmonic materials.

In order to compare resonator structures made of gold to those made of aluminium for their usefulness in the context of single-photon applications, identical structures made of either material were fabricated and experimentally characterized. For this, the surface roughness of the rings were measured with the help of an atomic force microscope and the autofluorescence of both structures was measured using a confocal photoluminescence setup, whose details are presented in section 4.1. As one would expect, similar to previous investigations on the surface quality of evaporated materials, the surface roughness of gold and aluminium structures differed only marginally and was in the order of several nanometer. The autofluorescence measured via photoluminescence using excitation light at 532 nm with 1 mW of optical power is presented in figures 6.1(c) for gold and 6.1(d) for aluminium. It is immediately evident that there is a huge difference in autofluorescence of over an order of magnitude between the two materials. While aluminium shows only weak autofluorescence of several kilocounts per seconds, which is acceptable in a single-photon environment, gold bullseye resonators aren't suitable for these kind of applications.

Additionally, the fluorescence stemming from both structures is spectrally differently distributed. Figure 6.1(b) compares normalized autofluorescence spectra for the two cases, which show quite different distributions for the two metals. While gold is quite evenly distributed over a broad spectral range, the aluminium autofluorescence is much more spectrally localized towards shorter wavelengths, a fact, which can already be expected from the different shapes of the respective band structures discussed earlier. As the fluorescence of aluminium is much more confined to a rather small spectral window, it can also be spectrally filtered much easier: For the case of silicon-vacancy centers emitting at 740 nm, a simple bandpass filter is sufficient to suppress the vast majority of autofluorescent light and enhance the signal-to-noise ratio of the emitted single photons significantly.

A possible disadvantage of using aluminium structures for plasmonic applications is its strong affinity to oxidation. This is partly true as the material surface quickly oxidizes. However, due to the quick formation of a complete aluminium oxide layer at the surface, oxidation into the bulk of the material as with silver is prevented. For the plasmonic resonances, this additional nanometer thin oxide layer on the metal interface leads to a shift of the plasmonic resonance and a slight damping of the strength of the resonance [29, 107]. Consequently, for

designing and simulating plasmonic ring structures made from aluminium, these shifts have to be experimentally investigated by measurements like the ones presented in the following section 6.2 and then taken into account in the final design of the bullseye resonator structure.

6.2. Characterization Measurements using Subwavelength Apertures

The proposed single-photon source is based on two key components: defect centers in nanodiamonds and metallic bullseye resonators. In order to fully understand the influence of the actual plasmonic bullseye structure, it is beneficial to investigate its influence independently from the quantum light source. One way to do this is to fabricate plasmonic devices, which mimic the behavior of a point-like light source using a subwavelength aperture. With this structure, both the experimental results as well as the corresponding simulations can be compared using a well-understood and well-investigated geometry [108, 109].

Figure 6.2(a) shows SEM images of such a subwavelength aperture surrounded by concentric aluminium rings. This structure has been realized on a fused-silica substrate, which had been covered by an evaporated aluminium film. On top of the aluminium layer, the ring structure was formed by the standard electron-beam lithography process. During this process, a multilayer of the electron-sensitive resist PMMA is spin-coated on the aluminium film and patterned by a focused electron beam. After removing the areas in the resist illuminated by the electron beam, a negative form of the ring structure is created, which is subsequently filled with metal using an evaporation technique. In a last step, the unpatterned PMMA regions are removed by a solvent. For a more detailed description of the fabrication process, see section A.1.2. By using a subsequent focused-ion beam milling process, which penetrated both the central disk as well as the reflecting metallic base film, the subwavelength aperture was created. The nanostructures produced by these steps possess a ring structure featuring a circle pitch of 550 nm, a circle width of 350 nm and a circle height of 80 nm with the central hole diameter being about 160 nm.

The realized structure has then been investigated by Fourier transmission measurements, the description of this method is found in section 4.2. For this measurement, strongly attenuated laser light at 532 nm was focused on the central aperture through the substrate and the transmitted farfield was mapped on a CCD chip. The result of this experiment is shown in figure 6.2(b). Clearly visible is a bright central emission spot surrounded by rings at higher emission angles. These airy-like emission profile already hints at an interference pattern, in this case the interference pattern induced by the surrounding ring structure. For a better and more comprehensive understanding of this observation, three-dimensional FDTD simulations (compare section 3.1.2) of the experimental case were performed and are presented in figure 6.2(c), which shows the simulated farfield of the subwavelength aperture depending on the illumination wavelength. Here, some spectral regions, where constructive interference occurs in forward direction, are clearly visible while this condition cannot be fulfilled for other wavelengths. For a more detailed investigation of these effects and the condition for emission redirection in forward direction see section 3.3. Finally, figure 6.2(d) compares the experimental findings with the corresponding simulations. It shows very good agreement between the two cases both for the position of the emission peaks and their relative height.
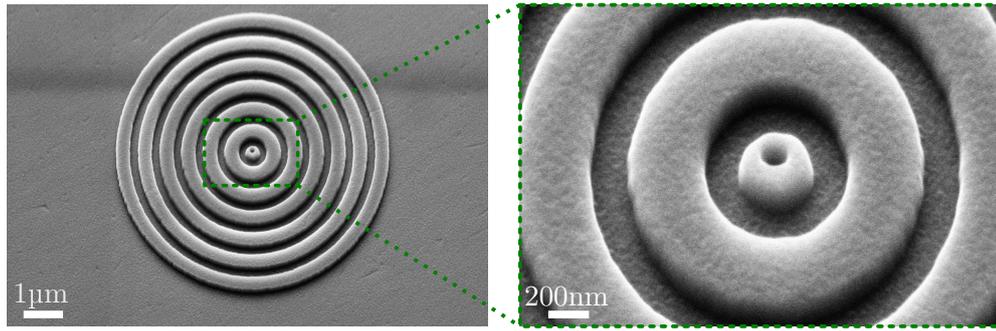
(a) SEM pictures of the investigated aluminium bullseye structure having circles with a pitch of 550 nm, a ring width of 350 nm and a height of 80 nm.
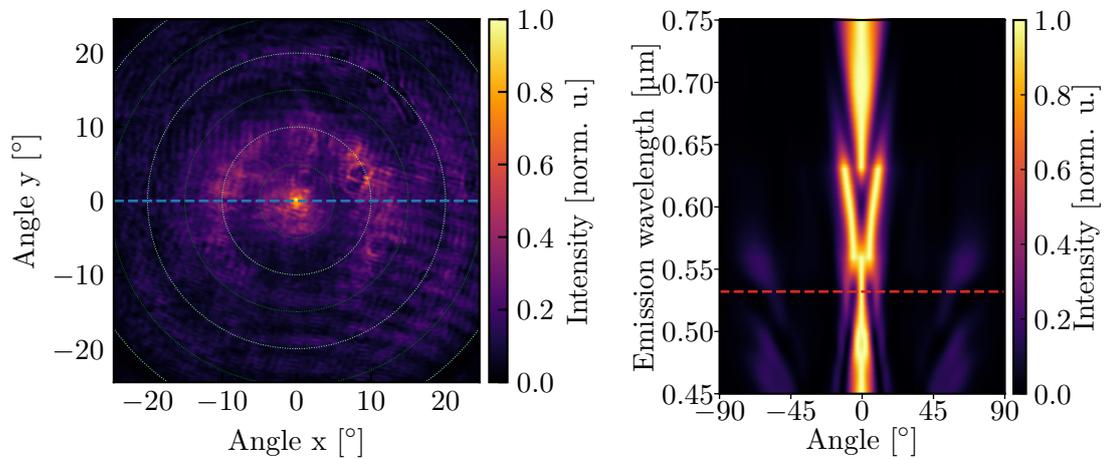
(b) Measured emission farfield of (a) using Fourier microscopy.

(c) FDTD simulation of the transmitted farfield of (a).
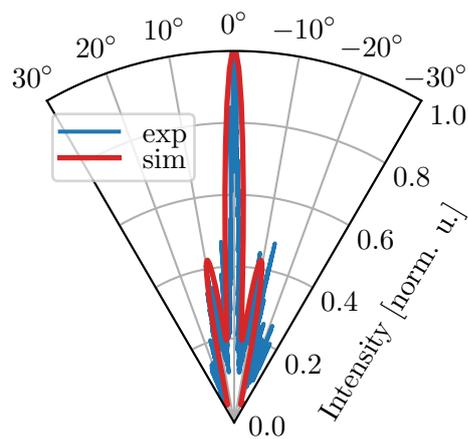
(d) Cut of (b) compared to the simulation in (c).

Figure 6.2.: Studies of the effect of bullseye structures around a subwavelength aperture. (a) SEM images of the studied aluminium structure. (b) Measured transmitted farfield at 532 nm using Fourier-space microscopy. (c) Corresponding FDTD simulations. (d) Comparison of the experimental case in (b) to the expected transmission farfield of the geometry from FDTD simulations in (c).

All in all, this preliminary experiment exemplified several key conclusions. First, the fabrication process works well and reproducibly, producing smooth structures with sharp ring edges, which are essential for efficient in- and out-coupling of light from free space modes to plasmonic modes. The experiment itself shows the desired effect of the emission redirection hinting that the same effect will occur under the right conditions for photoluminescence light of colour centers in the center of a bullseye structure. Additionally, the FDTD simulation, which is performed ab-initio without any assumptions other than the geometrical parameters and the choice of materials, agrees with the experimental case to a very high degree. Consequently, the combination of fabrication, experimental results and corresponding simulations works well together and can be used for checking against one another. This presents a very useful toolset for investigating the coupling of nanodiamonds to plasmonic nanostructures.

6.3. Coupling of Nanodiamonds to Plasmonic Structures

In theory, metallic ring resonators with feature sizes comparable to the wavelength of light should perform well in redistributing the emission of point-like light sources. This is investigated in detail in section 3.3. In this section, the corresponding experimental results and conclusions from investigating the emission of quantum emitters in different environments are presented.

6.3.1. Design and Geometry of the Investigated Nanodevice

After thoroughly testing and thereby confirming the correctness of the employed investigation tools in the previous section, the actual envisioned design of a single-photon emitting colour center in a nanodiamond positioned in the center of a bullseye resonator structure could be examined. To this end, planar metallic ring structures were fabricated by electron-beam lithography and subsequent metal evaporation similar to the subwavelength aperture case described in section 6.2. In an additional step, the final nanodevice was capped via spin-coating with a thin layer of PMMA 950K-2% resulting in a final polymer thickness of about 60 nm. This capping layer serves two purposes: first it shields the metal rings from the environment making the device itself more sturdy. Additionally, it smoothens the topography of the device, which is crucial for the accurate and deterministic positioning of nanodiamonds later on.

Instead of a simple reflecting metal base film typically used in these kinds of experiments, a commercial dielectric mirror substrate is employed. Figure 6.3(a) shows a cross-sectional view of such a dielectric filter, which was produced by a focused-ion beam for investigation of the filter layer layout. In combination with AFM measurements and further analysis of the layer composition by EDX (*energy dispersive x-ray spectroscopy*)[110] in an SEM machine equipped with an *Oxford EDS* detector, both the layer thicknesses as well as the layer materials could be accurately determined, which is crucial for accurately modeling the optical properties of the nanostructure via finite-element methods (see section 3.1.2). For further validation of these analyses, the found geometrical parameters were used in transfer-matrix method simulations for the transmission spectra of such a multilayer film[111]. Comparing the simulated result

(a) SEM image of the employed dielectric shortpass filter substrate.

(b) Transmission spectrum of (a) compared to emission spectra of colour centers.

(c) AFM image of a nanodiamond placed in the center of a bullseye structure.

(d) Scheme of the final investigated single-photon source geometry.
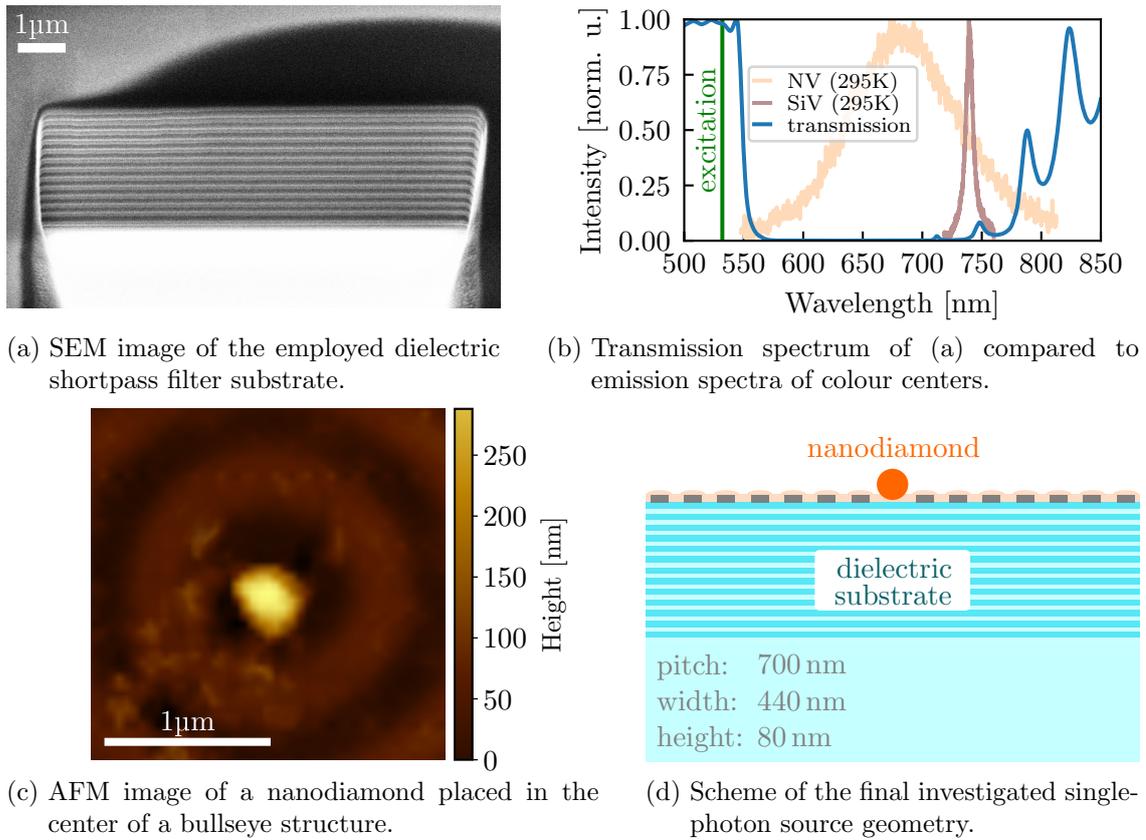
Figure 6.3.: Scheme and images of an investigated plasmonic bullseye structure with a positioned nanodiamond. (a) SEM image of the dielectric substrate. The trench for the cross-sectional view was produced by focused-ion beam milling. (b) Transmission spectrum of the employed substrate showing high transmission for excitation light at 532 nm and very low transmission for typical emission spectra of colour centers. (c) AFM image of the bullseye center after positioning of a nanodiamond. (d) Cross-sectional scheme of the final investigated nanodevice. The optimized parameters for the bullseye structure are rings with a lattice pitch of 700 nm, a ring width of 440 nm and a ring height of 80 nm.

with the publicly available transmission spectrum of the manufacturer further confirmed the found properties.

The dielectric mirror substrate itself was chosen for two purposes: On the one hand, it is reflective for the emission of colour centers in nanodiamonds on top of the mirror and on the other hand, it is also transmittive for the off-resonant excitation laser light at typically 532 nm. Due to this configuration, the nanodiamond can be efficiently optically excited with laser light through the substrate while its fluorescence is reflected in forward direction. The measured transmission curve of the dielectric substrate together with the typical photoluminescence spectra of NV- and SiV-centers at room temperature is presented in figure 6.3(b). As can be seen, even for the rather broad emission spectrum of the nitrogen-vacancy center at room temperature as well as the emission of SiV^- centers at 740 nm, the reflectivity of the substrate

is very high. Reflection measurements at 738 nm determined the reflectivity of these mirrors to be about 97.5%.

After the fabrication process, pre-chosen nanodiamonds had to be positioned correctly and accurately by nanomanipulation techniques, either by a so-called pick-and-place procedure, which is described in detail in section A.2.2, or by a spin-coating based approach described in section A.2.1. As the pick-and-place procedure, which enables positioning of nanodiamonds via an atomic force microscope, facilitates much better control of the overall process, it was the method of choice for this experimental study. Figure 6.3(c) shows an AFM image of the topography after positioning a nanodiamond in the center of a bullseye resonator. The image appears to be slightly blurred. However, this is the result of the AFM cantilever tip being blunted as part of the pick-and-place procedure. Additionally, the smoothing effect of the PMMA capping layer can be seen as well as small scratches on the PMMA layer, which were caused by the final fine positioning of the nanodiamond by horizontally pushing with the AFM tip. As the scratches are rather small, much smaller than both the nanodiamond and the wavelength of light, they do not disturb the performance of the nanoplasmonic device. The nanodiamond has a height of roughly 220 nm and contains an ensemble of silicon-vacancy center, which are located randomly inside the diamond crystal apart from an outer crystal shell of about 40 nm, where the energetic conditions for forming this rather large defect center with two vacancy sites cannot be met. See section 5.3 for further details on the employed colour center sample. This uncertainty in the emitter position caused a broadening of the emission characteristics from the plasmonic structure, an effect which is presented in the following sections.

Finally, figure 6.3(d) provides a cross-sectional schematic view of the final structure. The design parameters of the aluminium resonator structure are optimized for the emission of SiV centers at 740 nm (compare section 3.3 for more details on the modeling of such structures): a ring lattice pitch of 700 nm, a ring width of 440 nm, a ring height of 80 nm and a central ring radius of one lattice pitch. The whole resonator structure resides on top of 13 double layers of dielectric mirror with film thicknesses of 128 nm and 68 nm, respectively.

6.3.2. The Emitted Farfield of Nanodiamonds in Different Environments

In order to fully understand the behaviour of the two main components of the nanoplasmonic device, the planar dielectric mirror and the metallic ring structure, it is beneficial to study them independently from one another. The plasmonic structures were already investigated in section 6.2, in this section the farfield emission profile of nanodiamonds on different substrates will be investigated, namely on a planar glass substrate, the dielectric mirror substrate and in the center of a bullseye structure fabricated on top of a dielectric mirror. For each geometry, both simulated farfields using full three-dimensional FDTD simulations (compare section 3.1.2) as well as transmission measurements using Fourier microscopy (see section 4.2) were employed and compared to each other.

The general schemes for each of the three setups are displayed in figures 6.4(a), 6.4(b) and 6.4(c) and illustrate the general idea of this measurement series: By gradually adding building blocks to the geometry, their influence on the emission can be examined: First, a nanodiamond on a planar low-fluorescence fused silica substrate (*Hellma Analytics 665.000-QS*) is
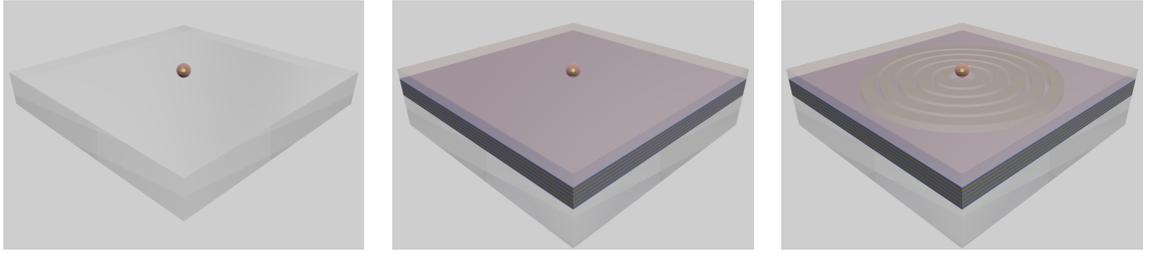
(a) Scheme for the emitter on a glass substrate

(b) Scheme for the emitter on a dielectric mirror

(c) Scheme for the emitter on a bullseye structure
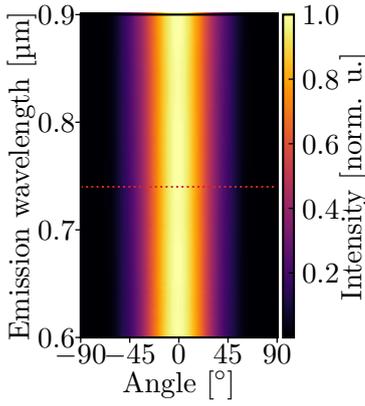
(d) FDTD simulation of (a)
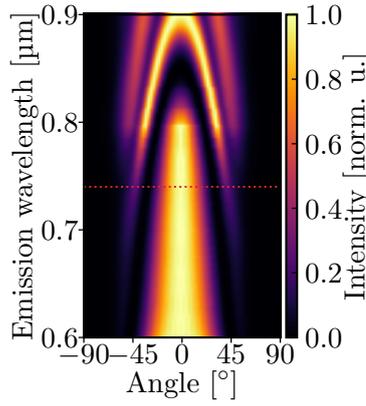
(e) FDTD simulation of (b)
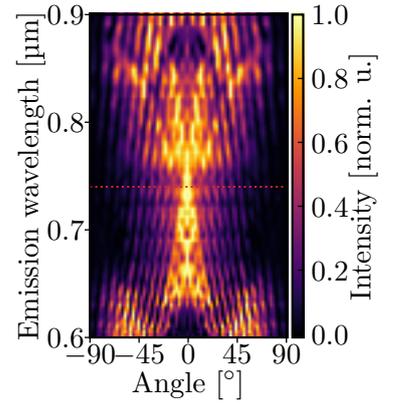
(f) FDTD simulation of (c)
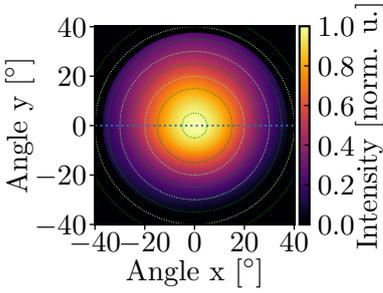
(g) Measured Fourier image of the emission of (a).
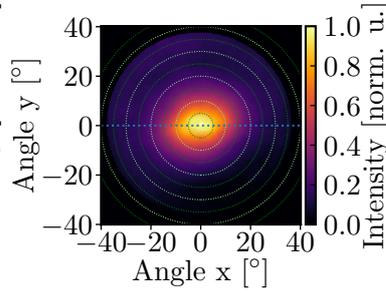
(h) Measured Fourier image of the emission of (b).
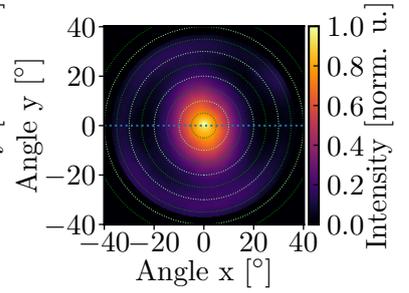
(i) Measured Fourier image of the emission of (c).
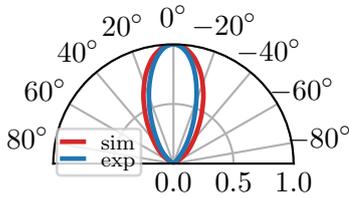
(j) Cut of (g) compared to (d).
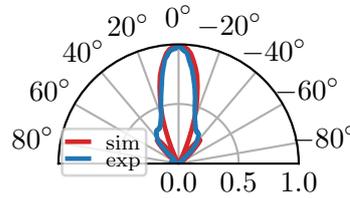
(k) Cut of (h) compared to (e).
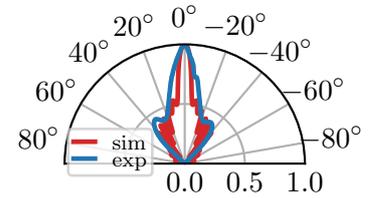
(l) Cut of (i) compared to (f).

Figure 6.4.: Studies on the effect of the environment on the emission profile of defect centers in nanodiamonds. (a)-(c) Schemes of the investigated environments. (d)-(f) Wavelength-dependent FDTD simulations of the emitted farfield. (g)-(i) Measured farfields of SiV centers at 740 nm using Fourier microscopy. (j)-(l) Comparison of the measured farfields with the simulated case.

investigated. In a next step, a nanodiamond is placed on a dielectric mirror substrate, which is presented in the previous section 6.3.1. In order to make the geometry comparable to the bullseye resonator case, the mirror substrate is also covered with a 60 nm PMMA capping layer. Finally, a nanodiamond is positioned in the center of a bullseye ring structure, which is located on the dielectric mirror. As the three individual nanodiamonds varied in their size from roughly 220 nm for the nanodiamond on the plasmonic structure to about 295 nm for the nanodiamond on top of the dielectric mirror, their individual sizes were taken into account in the investigation.

For all three geometries, FDTD simulations were performed, which take into account all available geometrical parameters. In order to fully mimic the employed nanodiamonds, which contained multiple silicon-vacancy center sites with random orientation and emission direction, dipolar sources with random orientations were placed inside the assumed diamond sphere apart from an outer diamond shell of about 40 nm, where silicon-vacancy centers are not energetically stable and, therefore, not formed. The emitted farfields for the three geometries simulated in this way are presented in figures 6.4(d)-6.4(f). In the simulations, the collected fields, which were used for the farfield calculation, were limited to the upper half of the simulation space since the emission in this hemisphere was to be investigated.

The influence of the dielectric substrate in the vicinity of the emitting sites is the main cause of the non-uniform emission profile for the case of the emitter residing on a glass substrate in figure 6.4(d). Intrinsically, the assumed emitter with randomly located dipoles would show perfectly isotropic emission characteristics. However, due to the fact that the emitting sites aren't located in vacuum but rather on top of a dielectric glass substrate, the emission profile is reshaped such that emission directions in upward and downward directions are favored compared to emission along the surface of the glass substrate. Additionally, only light emitted in the upper hemisphere is collected in the simulation, which results in the cone-shaped emission profile.

The simulations for the dielectric mirror case in figure 6.4(e) show a rather strong redistribution of light into forward direction, i.e. the direction normal to the surface. Additionally, an anti-resonance can be seen for an emission wavelength of about 820 nm. Both effects can be attributed to the dielectric mirror substrate as it introduces multiple reflection layers into the system. Due to the geometrically fixed conditions for constructive interference on these reflections, certain wavelengths are constructively interfering while this interference condition cannot be fulfilled for other ones. The influence of the mirror geometry and the corresponding dispersion properties of the employed materials can already be seen in the measured transmission curve of the employed mirror in figure 6.3(b), which shows the reflection band ending above 800 nm with additional smaller reflection peaks at higher wavelengths.

In order to investigate the influence of the geometry further, calculations for the interference conditions similar to the ones presented in section 3.3.2 can be employed. Figure 6.5 shows the simulated optical path length difference between light emitted directly in forward direction and light being reflected at the first dielectric layer with high refractive index. The relative optical path length φ can be calculated via

$$\varphi = \left(2 \cdot (r_{diamond} \cdot n_{diamond} + d_{PMMA} \cdot n_{PMMA} + d_{diel.} \cdot n_{diel.}) + \frac{\lambda}{2} \right) \quad \% \quad \frac{\lambda}{2} \qquad (6.1)$$
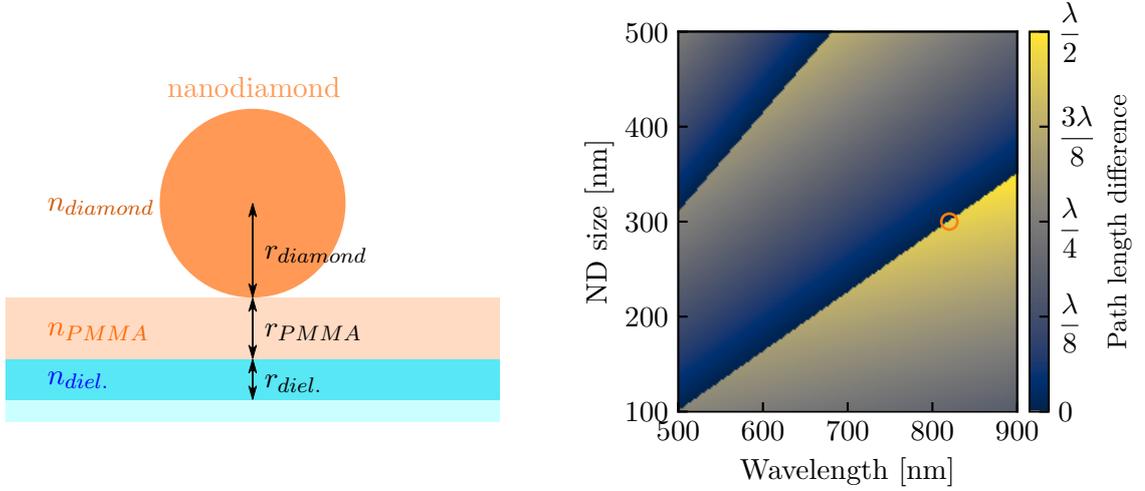
(a) Scheme for calculating the relative optical path length.

(b) Calculated relative optical path lengths for the scheme in (a).

Figure 6.5.: Calculated relative optical path length difference between light directly emitted in forward direction and light reflected by the first double-layer of the dielectric mirror substrate. (a) Scheme of the assumed geometry. (b) Calculated optical path length differences between the two paths using equation 6.1. The marked position at 820 nm and a diamond size of 300 nm corresponds to the observed anti-resonance in the full 2D simulation in figure 6.4(e).

with the thicknesses of the dielectric materials $r_{diamond}$, d_{PMMA} and $d_{diel.}$ for the first dielectric layer of the mirror and their refractive indices $n_{diamond}$, n_{PMMA} and $n_{diel.}$, respectively. Together with an additional phase shift of $\lambda/2$ due to reflection, the relative optical path length modulus $\lambda/2$ for destructive interference in forward direction can be calculated for different diamond sizes and emission wavelengths λ (figure 6.5(b)). The marked position, where the optical path length difference between the two light paths is $\lambda/2$ and, therefore, destructive, corresponds to an assumed nanodiamond size of 300 nm and a wavelength of 820 nm. This corresponds well to the full three-dimensional FDTD simulation in figure 6.4(e) with the anti-resonance starting at about 820 nm.

The simulation of a nanodiamond with many emitters positioned in the center of a bullseye structure on top of a dielectric mirror (figure 6.4(f)) provides a very different farfield pattern than the first two cases: Here, interference induced by the ring structure dominates the overall emission profile and induces a sharp resonance for the normal direction at about 740 nm, which coincides with the design goal of the structure. For more details on the design of the bullseye structure, compare section 3.3. Additional smaller sharp features are located at smaller angles around the forward direction. This can be attributed to the fact that the nanodiamond in the center hosts many randomly positioned emission dipoles with different orientations inside the diamond sphere. Due to this reason, some of the point emitters are located off-centered. As a result of this, the emission maximum is also slightly tilted relative to the forward direction, an effect, which is investigated in detail later on in section 6.5. The overall emission pattern stemming from all point emitters is then an incoherent sum of many different emission angles, which forms the observed rippled structure. Additionally, for emission wavelengths away

from the resonance region, the overall emission profile is highly broadened or features main resonances tilted relative to the forward direction.

Apart from simulating the structures, all three were also experimentally investigated using Fourier microscopy. For this measurement technique, light is collected by a microscope objective with a large numerical aperture, whose back-focal plane is then mapped on a CCD chip using an additional Bertrand lens. More details on this technique and information about the experimental setup can be found in section 4.2. Figures 6.4(g) - 6.4(i) show the measured emitted farfield for the three investigated structures. The SiV centers in the center of the structures were excited through the substrate side from the bottom with CW laser light at 532 nm and the emission profile emitted in the upward direction then recorded by the Fourier microscope system. When comparing the three measured Fourier images, a progressing increase in light concentration in the center of the image, which corresponds to the emission of light in forward direction, is clearly visible. The nanodiamond on a planar glass substrate (figure 6.4(g)) features a rather broad emission profile that stems from the intrinsically isotropic emission modified by the glass substrate and the measurement apparatus collecting only a part of the emission. The farfield emission profile for the nanodiamond positioned on the dielectric mirror substrate (figure 6.4(h)) is already much more confined. This is even more pronounced for the case of the nanodiamond being positioned in the center of the bullseye structure (figure 6.4(i)), where a very bright central emission area, which corresponds to the 0th interference order, is present. Additionally, a ring structure surrounding the central peak at about 30° is visible corresponding to the 1st interference order.

For a better quantitative comparison of the simulated results of the emission profile to the experimentally obtained farfield patterns, figures 6.4(j) - 6.4(l) present cuts from both methods in a polar plot for each studied geometry. In all three cases, one immediately sees good agreement between the simulated farfields and the measured emission patterns. This is rather unsurprising for the case of a nanodiamond on a planar glass strip (figure 6.4(j)), because only few parameters are influencing the emission shape. The observed deviations between the simulated and experimental case can be mainly attributed to the uncertainty in the actual height of the emitters relative to the glass surface, which are not known. But also the other two cases show very good agreement, yet slight deviations between simulation and experiment are visible in both of them. Although also here, the actual position of the emitting point sources are not known exactly, other uncertainties in the investigation play a role as well.

For the case of the nanodiamond on a dielectric mirror substrate, this uncertainty lies mainly in the interplay between geometrical and material parameters. Although the dielectric substrate has been thoroughly investigated using various techniques for both composition and dimensions (compare also section 6.3.1), which agree quite nicely and reproduce the transmission curve thoroughly, it is still afflicted by uncertainty. Especially the actual material parameters aren't known exactly but rather taken from literature and approximated in the simulations by a dispersive model (compare section 2.3.2). Therefore, it contributes to the uncertainty in the simulated results as compared to the experimental case. However, this uncertainty cannot be large as both the measured farfield could still be reproduced rather well and the accuracy of such dispersive simulations is reported manifoldly in literature [112, 33]. This fact is emphasized by the small degree of deviation between experiment and simulation.

Finally, the results for the case of a nanodiamond in the center of a bullseye resonator on top of a dielectric mirror substrate are compared (6.4(l)). Here, the experimental curve shows a strongly refocused cone-shaped emission peak in forward direction as well as a rather strong emission into the first emission order, which is manifested as side peaks in the one-dimensional polar plot. The complementing simulation in figure 6.4(f) predicts multiple ripple-like side peaks surrounding the central 0th order interference maximum, which match pleasantly to the experimental result. Similar to the case of the nanodiamond on a dielectric mirror, uncertainties in the geometrical parameters contribute to the slight deviations. Here, especially the actual distribution of emitter positions around the symmetry axis can only be estimated. Due to the fact that positioning emitters off-centered in the bullseye structure result in tilted emission profiles (compare also the measurement presented in the following section 6.5), their collective emission broadens and tilts the emitted farfield. The measured quite smooth farfield emission profile might be a result of this uncertainty. All in all, however, simulation and experiment agree to a high degree and emphasize the trustworthiness of the investigation.

6.4. Evaluation of the Bullseye Resonator Performance

When evaluating the experimental results by direct comparison to the corresponding simulations, some further analyses and conclusions can be done. In this regard, quantifying the actual performance of the bullseye structure for the capturing of light emitted by nanoemitters is of particular interest. Furthermore, the influence of the nanoplasmonic structure on the dynamics of the emitter itself is investigated.

6.4.1. Extracting and Analyzing the Collection Efficiency

Comparing the measured Fourier space images in figure 6.4 for the three investigated emitter environments clearly illustrates the combined influence of the bullseye structure and the underlying mirror on the emission shape of the intrinsically isotropic emitter. In order to further quantify the strength of the redirection, which is directly correlated to the efficiency with which one can collect the emission, the measured farfield in figure 6.4(i) is analyzed more thoroughly.

To this end, the relative cumulative average emission per solid angle $c_{obj}(NA)$ is calculated, which gives a figure for the redirection strength per emission angle, i.e. per chosen numerical aperture NA. This relative cumulative distribution has to be normalized by quantifying the additional losses in the system, which are not detected by the Fourier measurement. On the one hand, part of these losses is light, which is emitted into solid angles larger than those collected by the Fourier microscope. On the other hand, emission can also be transmitted through the non-perfect substrate mirror or can be absorbed by the nanostructure itself.

The complete formula for a quantitative calculation of the relative collection efficiency $\eta_{bull}(NA)$ for the experimentally investigated case in figure 6.4(i) can be written as

$$\eta_{bull}(NA) = c_{obj}(NA) \cdot (1 - l_{obj}) \cdot t_{filter} \cdot (1 - \mu_{Al}) \cdot r_{DM} \qquad (6.2)$$

Here, $c_{obj}(NA)$ is the already mentioned accumulated average emission per solid angle calculated from figure 6.4(i), l_{obj} represents the percentage of light being lost due to emission in angles not covered by the objective with a numerical aperture of NA=0.85, which was employed for the Fourier measurements, t_{filter} is the transmittivity of the optical filters in the detection path, μ_{Al} accounts for the absorption of light due to the aluminium structure and r_{DM} is the reflectivity of the dielectric mirror substrate. These single contributions have to be determined separately.

The losses due to emission angles larger than the numerical aperture of the microscope objective $l_{obj}(NA)$ can be estimated by analyzing the FDTD simulations. Comparing the experimental result to the simulated cases in figure 6.4 already illustrate the fact that the experimental results are nicely reproduced by the simulated cases. This fact can be employed for estimating the amount of emission loss due to high emission angles: As can be seen in the simulation in figure 6.4(f), nearly no emission is not captured by the k-space measurement, for the microscope objective with a numerical aperture of NA=0.85, the relative losses due to larger emission angles is less than 3%.

An additional loss channel is the transmission of light through the reflecting dielectric substrate, which is directly correlated with the reflectivity r_{DM} of the mirror. Despite the large number of thirteen double layers of high- and low-index dielectric materials (compare figure 6.3(a) for an SEM image of the layer structure), there is still some small transmission percentage present. Using transmission measurements with laser light at 740 nm, the wavelength of the SiV-center emission, reveals an average transmission of only 2.5%, which is in very good agreement with the manufacturer specifications.

The by far biggest loss channel is the absorption of light while propagating as bound surface plasmon polaritons on the aluminium structures. As the propagation length of these SPPs is small and in the range of only a few µm for an ideal metal-air interface, propagating for several hundred nanometers from the inner to the outer ring edge induces a significant loss of light due to absorption. This absorption μ_{Al} can be calculated analytically (compare section 2.3) and is a function of the propagation length of the SPPs. For a ring width of 420 nm, the absorption at a wavelength of 740 nm amounts to additional 14% of propagation loss. Possible additional loss of light due to so-called *leakage modes* [25], where the surface plasmon polaritons evanescently couples light to the substrate, was investigated by FDTD simulations but found the be of no importance for this investigation. This might be attributed to both the large height of the metal structure and the underlying substrate being a dielectric mirror, which does not permit propagation of light at 740 nm.

By combining the extracted collection efficiency of the measured bullseye resonator farfield with the investigated loss channels, the quantitative curve for the collection percentage per numerical aperture of the collection optics can be calculated via equation 6.2 and is shown in red in figure 6.6. For the purpose of comparing this curve with a case, where no structure is surrounding the emitter, the isotropic case is drawn in blue. The blue isotropic curve $\eta_{iso}(NA)$ represents the ratio of light from an isotropic source, which is emitted within a solid angle of chosen NA and can be calculated as

$$\eta_{iso}(NA) = -\frac{1}{2} \cdot [cos\,(arcsin\,(NA)) - 1] \tag{6.3}$$

In figure 6.6, the case of the bullseye structure shows a great improvement over the case of an isotropic emitter and enables the collection of a reasonable part of the overall emission for comparatively small numerical apertures: For example, with a collection optics having a numerical aperture of 0.5, which is still easily realizable with cheap, inexpensive optics, about 50% of the overall emitted light is collected.
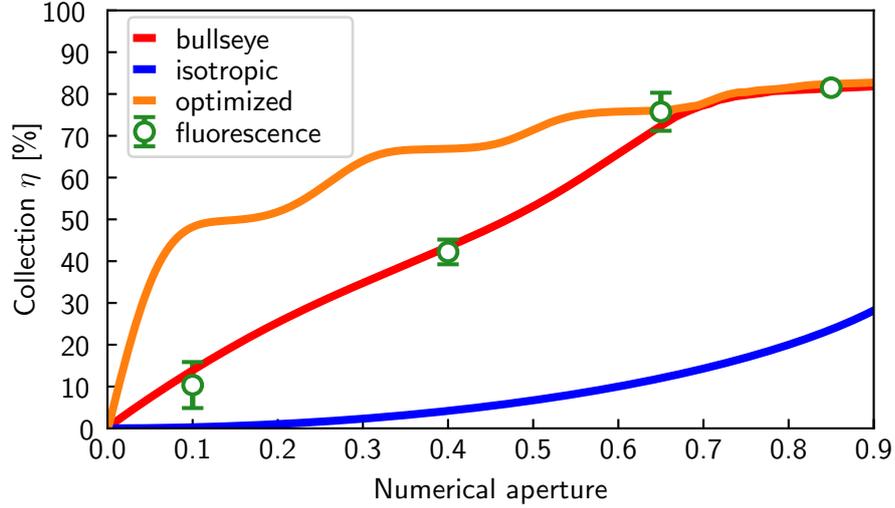
Figure 6.6.: Extracted collection efficiencies in dependence of the numerical aperture of the collection optics for a nanodiamond emitter on a bullseye resonator structure (red) compared to the case of an isotropic emitter (blue). The theoretical collection efficiency of an optimized bullseye structure with a single dipolar emitter is shown in orange. Independent measurements of the emitted fluorescence count rates for different numerical apertures of the collection optics in the case of the investigated bullseye structure are shown in green.

In order to experimentally verify the extracted collection efficiency in figure 6.6, the amount of fluorescence light emitted by the bullseye structure was measured for different numerical apertures. To this end, objectives with different numerical apertures of 0.1, 0.4, 0.65 and 0.85 were mounted on the transmission stage and the emission count rate was recorded by an avalanche photodiode. See section 4.1 for further technical details on the experimental setup.

As the employed objectives were from different manufacturers and, therefore, differed in their overall optical imaging quality, all of them were independently characterized. Especially the transmittivity of the single objectives varied greatly and was measured for each objective separately. In order to circumvent possible measurement errors due to differences in the coupling of light from the objective to optical fibers, a multi-mode fiber with a large core diameter of $50\,\mu m$ was used for guiding light from the transmission setup to the APD detector.

The measure for comparing the collection efficiency for the single objectives was the count rate on the APD detectors. To this end, several possible sources of errors were considered or circumvented: The excitation laser power for exciting the nanodiamond was actively controlled and kept constant well below saturation of the quantum emitters to ensure a constant emission rate from the source itself. In order to obtain more accurate results, both the excitation

and detection positions were automatically optimized and several runs were performed for each collection objective. The maximum observed count rates for all tries were recorded together with their statistical uncertainties. These raw count rates were then compared to each other, which gives a relative collection efficiency for different numerical apertures. In order to normalize these results, the measurement outcome for the objective with a numerical aperture of 0.85 was used, as this objective was also employed for the Fourier measurement and was, therefore, thoroughly characterized (compare section 4.2.2). For normalizing this measurement and, therefore, also the measurements for the other objectives, the previously discussed sources for light loss were considered.

The result of this measurement series using objectives with different numerical aperture is depicted in green in figure 6.6 with the error bars accounting for the uncertainties in the count rate measurement, excitation power and transmission properties of the objectives. Overall, these measurements mirror the extracted collection efficiency η_{NA} quite accurately. Still, the loss channels could only be estimated from theoretical models or independent measurements. Even though the estimations were thoroughly investigated, there is still room for uncertainty, the extracted collection efficiency curve for the bullseye case in figure 6.6 could also be slightly elevated or lowered.

It is worth mentioning at this point that the enhancement in the collection efficiency presented in red in figure 6.6 is not the upper limit of the achievable collection enhancement. The reason for this is that the investigated structure itself is not fully optimized due to the fact that the emitter positioned in the center of the structure consists of many point sources localized throughout the nanodiamond crystal structure. The resulting effect of positioning uncertainty also broadens the emission cone as can be seen in figure 6.4(i).

The case of a truly point source like emitter, which is investigated via simulations in the following section 6.4.3, is shown in orange in figure 6.6. It is clearly visible that the expectable collection enhancement is much higher for a single point source especially for lower numerical apertures as the emission profile shaped by the resonator structure is much more concentrated. Additionally, the emission profile itself improves and gets close to an ideal narrow cone shape, which enhances the coupling efficiency to cylindrical waveguiding structures like a single-mode fiber.

6.4.2. Evaluation of the Emission Dynamics

According to Fermi's Golden Rule, which is able to accurately describe many emission and absorption phenomena, the dynamics of a spontaneously decaying system depends on its surrounding [8]. Altering the geometry around the quantum emitter can therefore greatly influence its behaviour and enhance or suppress the rate of emission. Prominent examples of this dependence are the *Purcell effect*, which measures the relative emission enhancement of an emitter in a cavity structure [113, 49] or the *Drexhage experiment*, which directly maps the oscillating local density of optical states (LDOS) in the vicinity of a mirror by the change in the emission rate [114].

In an optical photoluminescence experiment, the influence of the geometry on the dynamics of the emitter can be directly investigated by measuring the excited state lifetime. To do this, one typically performs time-correlated single-photon counting (TCSPC), which involves
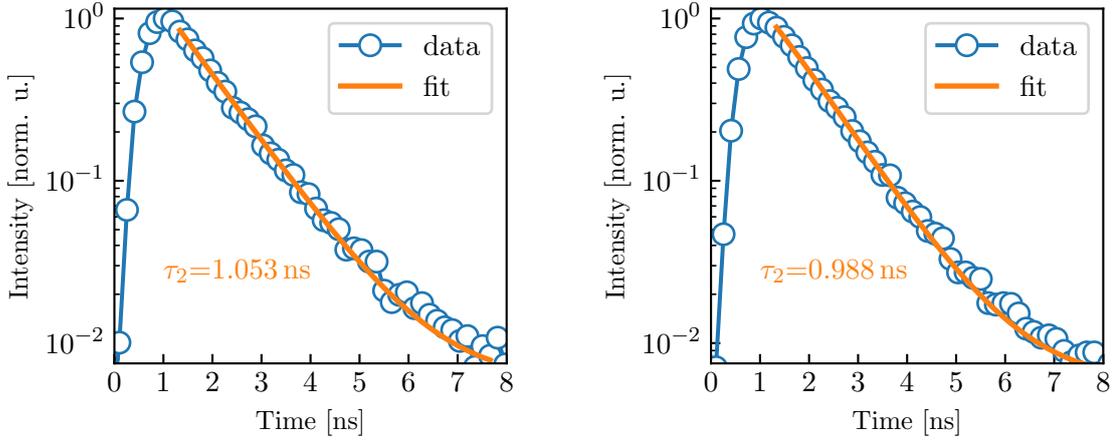
(a) Lifetime trace of the nanodiamond on a planar fused silica substrate.

(b) Lifetime trace of the nanodiamond in the center of a bullseye structre.

Figure 6.7.: Measured and fitted lifetimes of a nanodiamond on (a) a planar fused silica substrate and (b) after being positioned in the center of a plasmonic bullseye resonator. The lifetime traces were fitted with a double-exponentially modified Gaussian distribution (compare section 4.10 for further details about the fit procedure).

the repeated optical excitation of the system with a short, well-defined laser pulse and the recording of the time delay between excitation and the detection of a photon. The histogram of the arrival time of photons then incorporates the statistical excited state lifetime of the system. Figure 6.7 shows the recorded histogram of detected photons for a nanodiamond, which was first positioned on a planar glass substrate and subsequently transferred to the center of a bullseye resonator structure. Performing TCSPC measurements for both cases allows to determine the relative change of the emission rate of the emitter for the two geometrical surroundings. Both decay curves were fitted with a double-exponentially modified Gaussian distribution, which accounts for both the systematic timing uncertainty as well as the finite temporal width of the excitation laser. For further details about the experimental setup and the fitting analysis, see section 4.3.

The extracted collective lifetime of the ensemble of silicon-vacancy centers in the nanodiamond for the two environments are (1.053 ± 0.019) ns for the case of the glass substrate and (0.988 ± 0.014) ns for the full bullseye resonator structure, respectively. This means that the bullseye structure offers an increase in the local density of optical state as compared to the case of a planar fused silica substrate for the nanodiamond crystal. Is this to be expected? Again, the experimental case can be reconstructed by FDTD simulations, which offers a direct way of determining the density of states for a certain geometry. For this, one uses the fact that the radiated power from a simulated point-like dipole emitter is directly proportional to the local density of states at this point ([34], chapter 4).

3D simulations of the local density of states for a nanodiamond positioned on a planar glass substrate, a dielectric mirror and in the center of a bullseye structure on top of a dielectric mirror were performed for horizontal and vertical polarization. Table 6.1 summarizes the

	glass		dielectric mirror		bullseye	
Polarization	H	V	H	V	H	V
rel. enhancement factor	1.067	1.030	0.898	1.078	0.993	1.529
ratio H/V	1.036		0.833		0.649	

Table 6.1.: Relative emission enhancements of a single dipole positioned in different environments comparing horizontal (H) and vertical (V) emission for an emission wavelength of 740 nm.

results for an assumed emission wavelength of 740 nm. Here, the simulated LDOS values are normalized to the values for an emitter positioned in vacuum and are labeled as relative emission enhancement factors.

The probably most striking outcome of this simulation series is the diverging LDOS in the case of a metallic bullseye structure for the two emission polarization directions. This difference can be traced back to the nature of surface plasmon polaritons itself (compare also section 2.3.2): For an ideal planar metal-dielectric interface, only electric field components normal to the metal-dielectric interface (TM modes, also called vertically (V) polarized) can propagate along the boundary. For this reason, the local density of optical states for an emitter in the center of a plasmonic bullseye structure is larger for V polarization as compared to H polarized emission as scattering into resonant SPP modes on the metallic ring edges is favored for TM-polarized light.
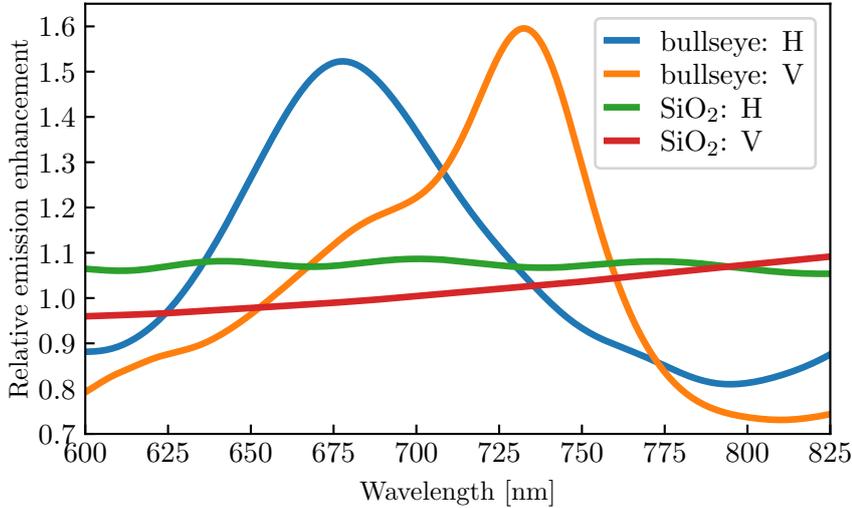
Figure 6.8.: Simulated local density of optical states for dipoles with horizontal (H) and vertical (V) electrical polarization in the center of a diamond sphere on a bullseye resonator structure and on a glass substrate. The relative emission enhancements are calculated by normalizing the emission rates for the single environments and polarizations using the emission rate of a dipole in vacuum.

This effect can be further investigated by comparing the normalized relative LDOS values for different wavelengths, which is presented in figure 6.8 for the situation of a nanodiamond emitter being positioned on a planar fused silica (SiO_2) substrate and in the center of a bullseye

resonator structure. For an emitter on a SiO$_2$ substrate, the relative emission enhancement is nearly constant over the investigated spectral region and rather independent of the emission polarization. This is in stark contrast to the situation involving the bullseye resonator, which shows a strong dependence on both emission polarization and emission wavelength. As the data in table 6.1 already indicates, there is a strong emission enhancement for vertical emission polarization around 740 nm, the design wavelength of the resonator. In spectral regions outside of this resonance region, however, horizontal polarization is more strongly enhanced or less suppressed compared to the local density of states without any structure.

The simulated results for the relative emission enhancement can be directly compared to the experimentally measured excited state lifetimes of a nanodiamond with an ensemble of colour centers in figure 6.7, which is positioned first on a planar fused silica substrate and subsequently in the center of a bullseye resonator. Comparing both measurements leads to a relative lifetime reduction - corresponding to a relative increase in emission rate - of about 6.5%. One uncertainty in this measurement is the emission dipole orientation of the silicon-vacancy centers in the nanodiamond. This is due to the fact that the SiV-centers are oriented along the four crystal [111] axes and the orientation of the diamond crystal itself relative to the geometry is unknown. However, the fact that there are many emitters in the diamond should lead - on average - to an equal amount of horizontal and vertical polarization. The simulated values of figure 6.8 predict an enhancement of 20% for the emitter in the bullseye resonator as compared to the emitter on a planar glass substrate. This number is significantly larger than the experimental value. Nevertheless, both the simulation and the experimental result illustrate the same trend: A metallic bullseye resonator structure can enhance the local density of optical states and therefore the emission rate of an emitter to a measurable degree.

6.4.3. Coupling of Redirected Light to Optical Fibers

For typical optical experiments, light is often guided with the help of optical fibers, as they offer both flexibility for the experimental layout as well as very low propagation losses. Similar to the case of planar dielectric waveguiding structures, which is discussed in detail in section 3.2, a standard single-mode optical fiber has a circular Gaussian shaped fundamental mode. In order to efficiently couple a propagating light beam to this guided mode, one needs sufficiently large mode overlap between the incoming and the fiber mode, a procedure which is often called *mode matching* [115].

The simulated emission farfield of a single point-like quantum emitter, which is positioned in the center of a bullseye structure described in section 6.1, is presented in figure 6.9. Here, both the two-dimensional emission pattern as well as a comparison between the expected farfields of emitters with horizontal and vertical position are illustrated. The optimized farfield pattern in figure 6.9(a) bears strong resemblance to a spherical two-dimensional Gaussian distribution and confines the vast majority of the emission to angles below 5°. Additionally, in contrast to the emission pattern of the measured system in figure 6.4(i) with many emitters in the center, for a single emitter the higher interference orders are nearly invisible.

A drawback of many nanophotonic schemes for efficiently harvesting the emission of quantum emitters is the need for a correct orientation of the emitting dipole: For example, only certain emission polarizations can couple to supported modes efficiently. In stark contrast to that,
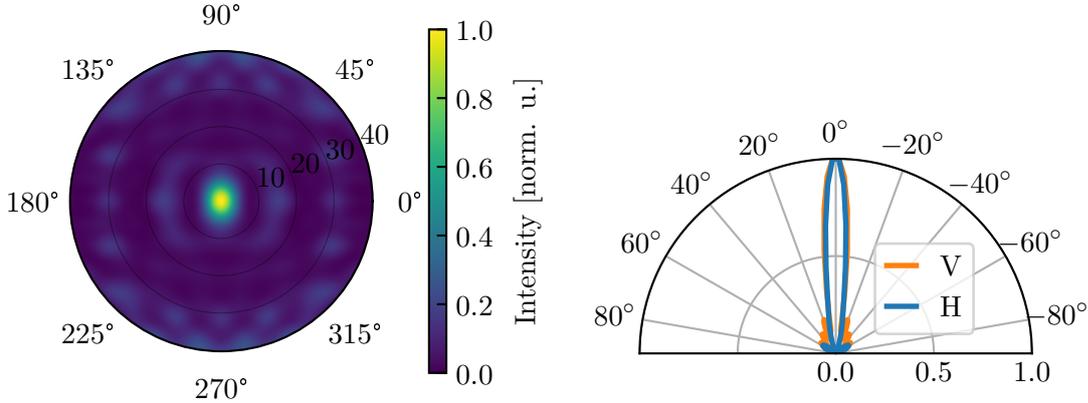
(a) Simulated emission farfield of a single emitter on a bullseye structure.

(b) Comparison of the emission pattern for different dipole polarizations.

Figure 6.9.: Simulated emission farfields using FDTD modeling of a single point-like emitter on a bullseye resonator structure. (a) Farfield emission pattern for a H polarized nanoemitter on a bullseye resonator showing a Gaussian-like narrow emission profile. (b) Comparison of the mission shapes of H and V polarized dipoles. Very similar emission patterns are produced by the resonator structure.

the presented bullseye resonator scheme operates nearly independently from the emission polarization. If one compares the emission pattern for horizontally and vertically polarized light, which is presented in figure 6.9(b), one finds nearly no difference between the two orientations. This can be explained by the basic working principle of the resonator structure: No matter where the emission is directed at, it is either redirected by the plasmonic ring structure, mirrored at the reflecting substrate or already propagating in forward direction. As figure 6.9(b) suggests, apart from differences in the expected emission rate, the resulting interference pattern for different polarizations is, therefore, always nearly the same. Colloquially speaking, one could say that the resonator structure can deal with all polarizations equally well.

For efficient coupling of the emitted farfield to a single-mode fiber, the already mentioned mode-matching conditions have to be met to a high degree. In particular, large coupling efficiencies from a free space mode like the emitted farfield to the guided mode of an optical fiber necessitates that the shape of the optical modes should be very similar. The illustrated two-dimensional emission pattern in figure 6.9(a) already resembles a circular Gaussian beam, the expected coupling of the resonator mode to a single-mode fiber can, therefore, be expected to be large.

In general, the coupling efficiency between two optical modes is determined by the overlap of the two light fields. In mathematical terms, this is expressed by the *overlap integral* η_{12} in equation 6.4, which calculates the overlap between two modes $\mathbf{E}_1$ and $\mathbf{E}_2$ [46].

$$\eta_{12} = \frac{P_2}{P_1} = \frac{\left| \int \mathbf{E}_1^* \cdot \mathbf{E}_2 \, \mathrm{dA} \right|^2}{\int |\mathbf{E}_1|^2 \, \mathrm{dA} \cdot \int |\mathbf{E}_2|^2 \, \mathrm{dA}} \tag{6.4}$$

The integral calculates the mathematical overlap between the two modes and normalizes the output by the overall power. For calculating the incoupling efficiency into a single-mode optical fiber, this corresponds to an overlap integral with the fundamental mode of the fiber, which is a circular two-dimensional Gaussian shape. Good fiber-coupling, therefore, necessitates an incoming mode with a shape similar to that of a Gaussian beam. When calculating the overlap integral of the simulated mode in figure 6.9(a) to a circular Gaussian beam representing the single-mode fiber mode [116], the coupling efficiency can easily exceed 60% if the overall mode diameters match. Together with an intrinsic loss of power at the fiber facet due to Fresnel reflection, which corresponds to about 4% of additional loss, nearly 60% of the bullseye resonator farfield can be coupled into standard single-mode optical fibers.

6.5. Aiming with Bullseye Resonators

Imagine a situation, where more than one single-photon source based on the presented bullseye resonator scheme should be employed. Typically, this involves that light from both sources are spatially overlapping at some point, e.g. in order to couple both sources to a single-mode fiber or for free space applications aiming at a specific point in space. Either case requires the possibility to aim with the emission of a source at a certain direction. This could be realized by employing isolated nanophotonic structures, which are mounted independently to one another. However, positioning small micrometer sized structures like the presented bullseye resonators with high accuracy involves both special equipment and labor. Another approach is to place more than one bullseye structure, each with its own single quantum emitter, on one structure, which then emit at slightly different emission angles.

As the substrate of the bullseye structures is planar by default, one therefore has to tailor the interference condition of the farfield emission. In an intrinsically symmetric structure like the one presented here, this can be very simply realized by displacing the emitter relative to the center position. Due to this breaking of the structure symmetry, a new resonance condition has to be fulfilled, which is determined by the now slight phase difference between the two structure sides. As a result of this, constructive interference occurs at a tilting angle relative to the forward direction.

The resulting effect of shifted emission mainly depends on two geometrical parameters: on the one hand, this is the displacement of the emitter relative to the central position in the structure. On the other hand, also the height of the emitter, i.e. the distance to the surface, is important as this also influences the interference condition (see also section 3.3). In order to investigate the effects of both parameters on the emission direction, a series of FDTD simulations for different displacements and nanodiamond heights was performed. For each simulation run, both the position of maximum emission as well as the width of the farfield emission cone, approximated by a Lorentzian curve, were recorded. Figure 6.10 summarizes the results of the 180 single simulation runs.

The simulation results show a nonlinear behaviour: for displacements of the nanodiamond below 175 nm, the emission shift relative to normal emission increases linearly and the angular width of the farfield cone, which is defined as the full-width at half-maximum (FWHM) in degrees, stays small. For higher displacements, the interference conditions are altered such that constructive interference of the 0th order is not fulfilled anymore, instead the interference
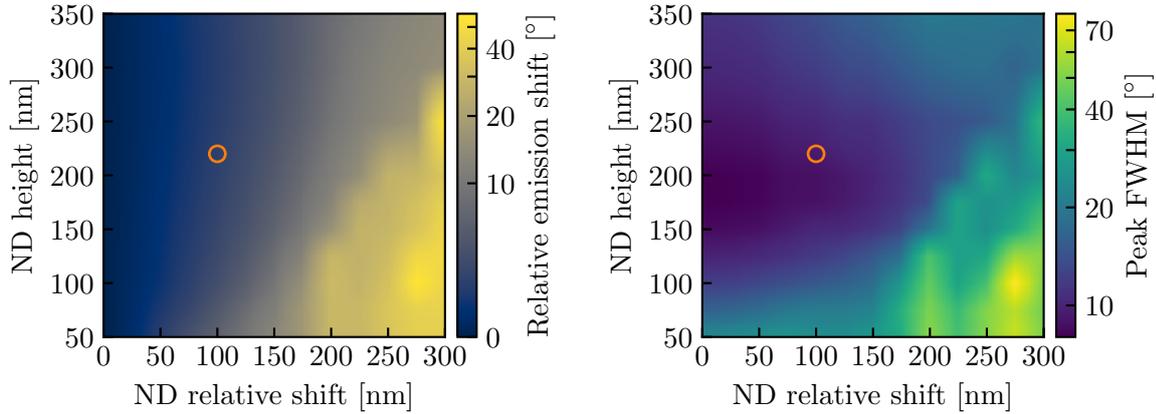
(a) Position of the relative maximum emission of displaced NDs for different ND sizes.

(b) FWHM of relative maximum position of displaced NDs for different ND sizes.

Figure 6.10.: Joined results of simulations of the effect of off-centered positioned nanodiamonds (NDs) on the emission direction. (a) Direction of maximum emission relative to normal emission in dependence of the relative position shift compared to the center of the resonator structure. (b) Corresponding full-width at half-maximum peak diameter of the brightest interference order positions of (a). The orange circle marks the experimentally investigated case presented in figure 6.11.

favors emission at high emission angles. This corresponds with a sudden increase in the width of the emission cone meaning that at this point also the focusing capability of the bullseye resonator structure breaks down.

The main outcome of the simulations series in figure 6.10 is that aiming is possible to a certain extent without loosing the redirection capability of the resonator structure. However, the effect is limited to several degrees due to a breakdown of the interference conditions. This simulated case is also verified with an experimental measurement: Figure 6.11 shows the outcome of this experiment, which involves a nanodiamond positioned in the structure with a small displacement relative to the central position. Figure 6.11(a) displays the topography of the investigated structure after positioning of the nanodiamond with the help of an atomic force microscope. The displacement of the center of the nanodiamond to the structure origin is about 100 nm.

The measured emission farfield of the structure is presented in figure 6.11(b) and features an emission peak slightly tilted at an angle of approximately 3.5° relative to the normal direction. As explained in the previous paragraph, this is a direct effect of the additional phase shift induced by the off-centered position of the emitters. For a more detailed investigation, wavelength-dependent FDTD simulations were performed and are presented in figure 6.11(c). As one would assume from the simulation series illustrated in figure 6.10, in the spectral resonance region around 740 nm, the emission peak is tilted to one direction. Comparing the experimentally obtained emission farfield to the simulation in a polar plot in figure 6.11(d) reveals very good agreement between both.

(a) AFM image of a nanodiamond positioned off-centered on a bullseye structure.

(b) Measured emission farfield of (a) using Fourier microscopy.

(c) Wavelength-dependend FDTD simulations of the emitted farfield.

(d) Cut of the experimental result in (b) compared to the FDTD simulations in (c).
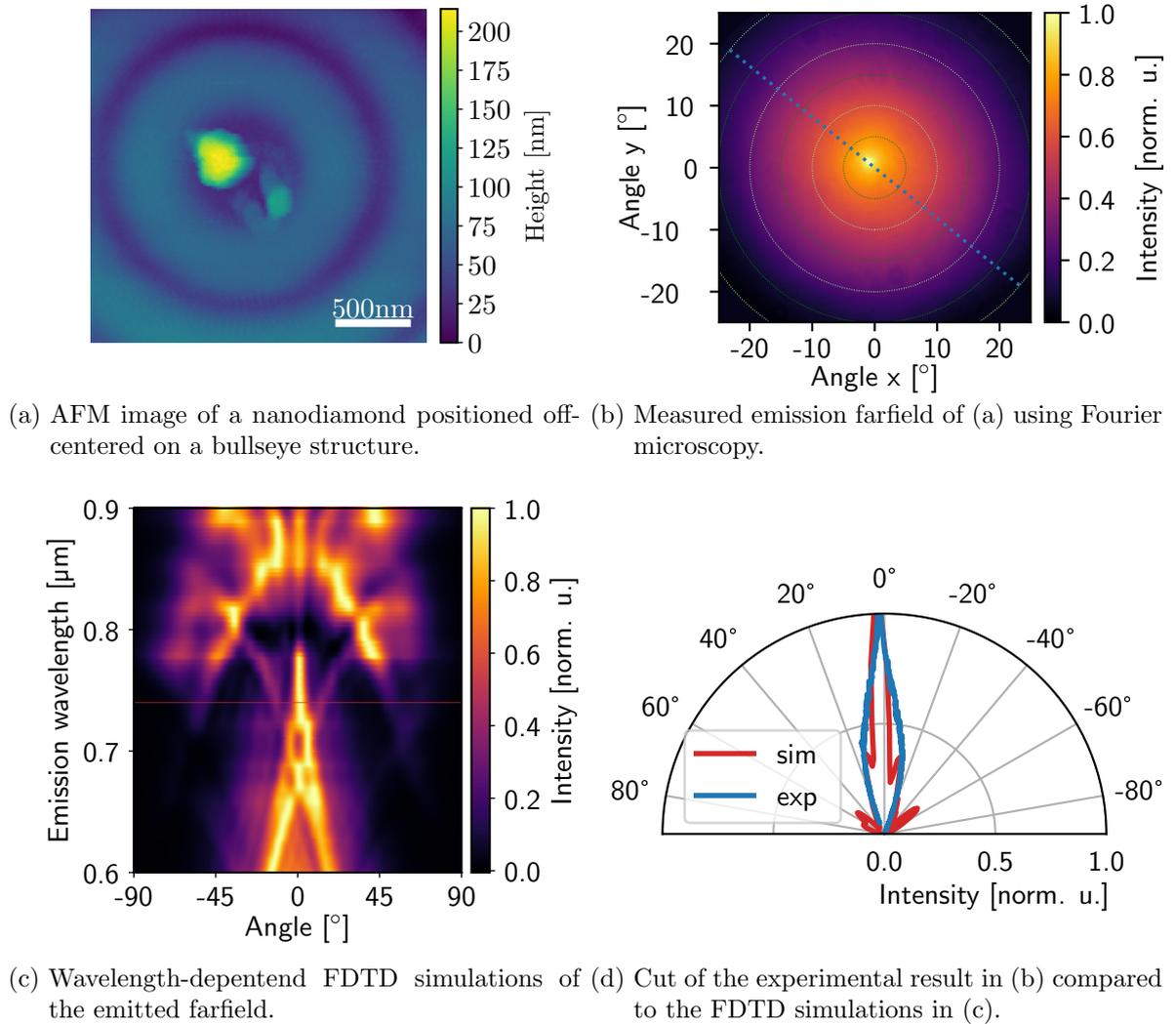
Figure 6.11.: Studies on the effect of off-centered positioning of nanodiamonds on bullseye structures. (a) AFM image of a nanodiamond positioned off-centered in the middle of a bullseye structure. Due to measuring with a slightly blunted cantilever tip, the ND appears bigger than its actual size. (b) Measured emitted farfield of the off-centered structure in (a) showing a shift in the main emission direction. (c) Simulated farfield emission of the off-centered positioned ND in dependence on the emission wavelength. (d) Comparison of a cut through (b) to corresponding FDTD simulations in (c) in a polar plot showing a tilt of about 3.5° in the emission direction.

The combination of experimental studies and corresponding simulations illustrate the possibility of actively controlling the emission direction of quantum emitters with bullseye structures. By using the highly precise positioning technique of AFM-assisted pick-and-place of nanoemitters in the center of the bullseye structure, which facilitates position accuracies in the range of some 10 nm, the resulting emission tilt is controllable to sub-degree accuracy. As each

bullseye single-photon structure can be tuned independently from one another, this technique allows also for adjusting different sources on one planar substrate relative to each other with ease and accuracy.

Chapter 7.

Summary and Outlook

The basic goal of this thesis was the creation of efficient solid-state based single-photon sources. For this, colour centers in diamond were employed as nonclassical light sources, which are well-known for their ability to emit single quanta of light even at room temperature. By combining these nanoemitters with nanophotonic or nanoplasmonic structures, the resulting hybrid quantum system enables efficient and deterministic creation and usage of single photons on demand.

Several key aspects for creating a hybrid source made of colour centers in nanodiamonds and plasmonic ring resonators were presented. Starting with a theoretical description of the interaction between electromagnetic waves and matter allowed for introducing the concepts for both dielectric waveguiding structures as well as the basic working principles of plasmonic structures and of surface plasmon polaritons. Based on this theoretical description, two different types of nanophotonic structures were investigated by both numerical simulations and analytical models: dielectric slot waveguides made of Ta_2O_5 and plasmonic bullseye resonators formed by concentric metallic rings on a reflective substrate. Investigating both approaches highlighted their potential for efficiently collecting light emitted by nanoemitters: While the slot waveguide approach facilitates collection of light in bound waveguide modes, which can be directly used in planar waveguiding circuits, plasmonic bullseye resonators reshape the farfield emission profile of the nanoemitter from an intrinsically isotropic emission to a highly directed one.

Two different types of colour centers were presented in detail, the nitrogen-vacancy center and the silicon-vacancy centers. For the nitrogen-vacancy center, a resonant excitation scheme at room temperature was developed, which can be employed for purifying the emission of the center. For the silicon-vacancy center, the temperature-dependent emission properties were studied. Both colour centers have their own distinct advantages and disadvantages, which have to be taken into account when choosing an appropriate one. For applications, where single-photon emission is required with high rate and purity, the silicon-vacancy center is highly advantageous as its spectral emission is much more confined. For this reason, it was employed in the experimental investigations of hybrid single-photon sources.

In order to experimentally characterize quantum emitters and measure the performance of fabricated hybrid single-photon sources, an optical photoluminescence setup was constructed, which enabled both the assembly of hybrid systems by an atomic force microscope based pick-and-place approach and the measurement of the emission shape by Fourier microscopy.

The real performance of a hybrid single-photon source based on bullseye resonators was experimentally determined by investigating aluminium ring resonators on a dielectric substrate, which hosted a nanodiamond with several silicon-vacancy centers at its center. In this regard, both the nanoplasmonic device itself as well as its influence on the emission shape of quantum emitters was measured. As predicted by numerical calculations, the experiments illustrates the great potential of such resonator structures for efficiently harvesting emitted single photons, especially when using low numerical aperture collection optics: Even cost-effective optics with a moderate numerical aperture of 0.5 are sufficient to collect more than half of the overall emitted light. Further investigations revealed that for a true point-like single quantum emitter, the collection efficiency can be even higher.

7.1. Further Possible Design Improvements

Colour centers in diamond work well as single-photon sources, especially at room temperature. However, depending on the requirements on the emitted single photons, other nonclassical emitters might be advantageous for certain tasks. Especially if the emission wavelength cannot be chosen freely, colour centers in diamond are at a disadvantage as their emission line is determined by the interaction of the dopant atom with the crystal environment. Here, other types of emitters can be advantageous, e.g. colloidal quantum dots [117, 118], dopant sites in other host matrices like SiC, YAG or ZnO [119] or organic dye molecules stabilized by an additional host environment [120]. Due to the presented hybrid approach for creating single-photon sources, where the emitter is deterministically positioned in the center of the resonator structure, switching the quantum emitter could be easily performed.
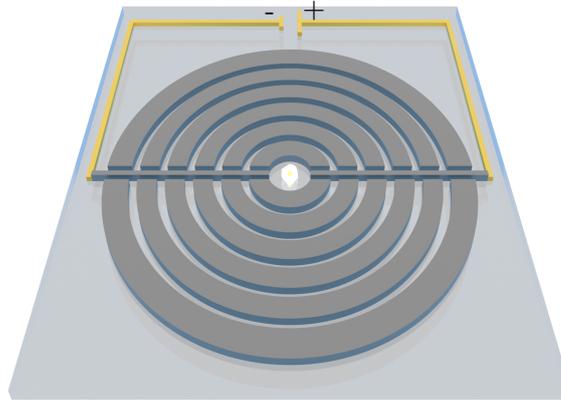
Figure 7.1.: Scheme for implementing electrical tuning of quantum emitters via the dc Stark effect in bullseye resonator structures.

Regardless of the employed emitter, in practical usage their emission frequency can still vary due to imperfections of the host matrix or local charge fluctuations. To address this problem in bullseye resonator structures in situ, applying local electric fields for influencing the emission of quantum emitters via the *dc Stark shift* is possible [79]. While the silicon-vacancy center does not possess a permanent electric dipole and is, therefore, insensitive to applied external

electric fields, the emission frequency of nitrogen-vacancy centers or other quantum emitters can be influenced greatly by this technique [121, 122].

In case of the presented metallic ring structure, which is fabricated by top-down lithography, the necessary gating electrodes can be directly incorporated in the design of the waveguides. Figure 7.1 illustrates one possible geometry. Initial electrostatic simulations with *Comsol Multiphysics* [123] hint that this design allows for effective dc Stark tuning of the emitter in the center of the structure by moderate gating voltages of some $10\,\mathrm{V}$. This corresponds to an effective tuning range above $10\,\mathrm{GHz}$ for the nitrogen-vacancy center at $633\,\mathrm{nm}$, which is similar to published values [124, 125]. Additionally, the performance of the bullseye structure in redirecting the emission suffers only slightly as long as the main emission direction of the quantum emitter is not directly in line with the gating electrodes.

7.2. A Compact and Sturdy Source of Single Photons

Many real-life applications require efficient single-photon sources, which are easy to use and insensible to disturbances, i.e. suitable for the usage in - for experimental laboratories standards - rough environments. While the single-photon source itself is composed of solid-state constituents, which are in itself insensitive to shocks, both the binding of the quantum emitter to the center of the structure and the resistance of the overall system have to be increased. One possible solution here would be to cover the assembled system with a capping layer, thereby protecting it from outside influence. In this regard, sputter deposition of fused SiO_2 is especially useful as it creates a transparent film of nearly arbitrary thickness.
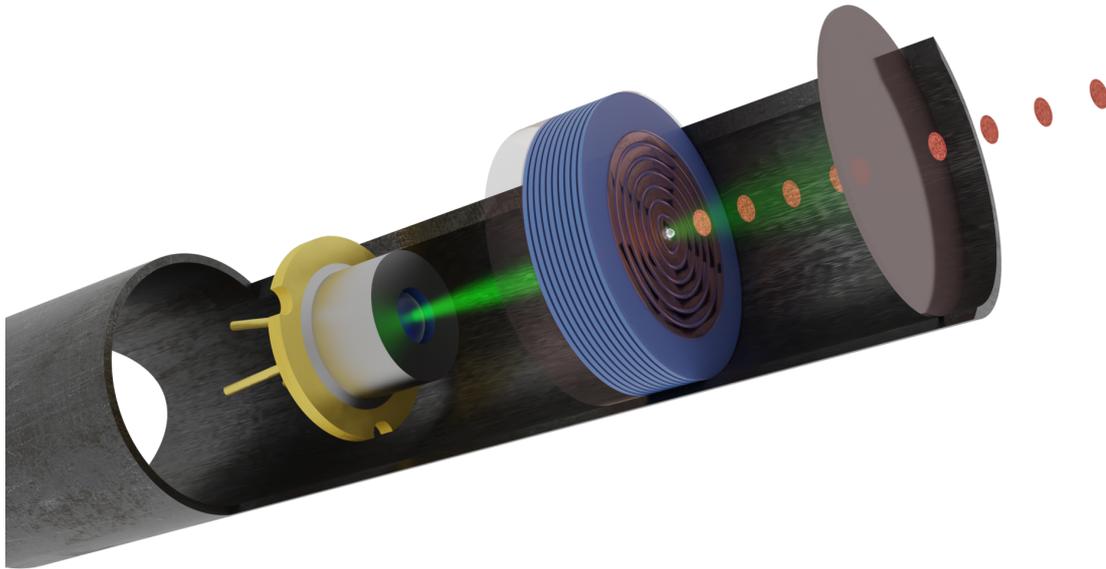
Figure 7.2.: Scheme for creating a compact single-photon source based on bullseye resonators. Apart from the structure itself, only a simple diode-based excitation light source and a cleanup filter for spectral cleaning of the emission are necessary.

Additionally, the presented hybrid sources can be operated in transmission mode, i.e. the excitation direction is separated from the emission side. This allows for creating ultra-compact and cost-effective sources as only a simple one-directional beam path has to be created. Compare figure 7.2 for the principal arrangement of such a source: Apart from the bullseye resonator structure, only an excitation light source is necessary, which can be realized by a simple laser diode on the backside of the plasmonic sample. In combination with the sturdy nature of solid-state systems, such a hybrid single-photon source could therefore also be employed in harsh environments.

Appendix A.

Realization of Nanooptical Structures

Richard Feynman's famous talk titled "*There's plenty of room at the bottom*" from 1959 presented many new ideas for experiments and technologies and since then has become a catchphrase for nearly anything, which can be related to physics at the small micrometer- to nanoscale. Many new ideas were realized in the following decades by improved or newly invented fabrication techniques. For optical experiments working in the visible or near-infrared spectral region, this meant that one could now create structures with sizes comparable to the wavelength of light, which facilitated novel types of interaction between light and matter. Furthermore, tools for directly measuring or manipulating objects at the nanoscale were investigated.

Developing and realizing optical structures at the nanoscale requires specialized techniques both for the fabrication of structures as well as the manipulation of nanooptical emitters. In this chapter, both aspects for the creation of hybrid single-photon sources based on defect centers in nanodiamonds coupled to optical nanostructures are presented. The first part of this chapter discusses the fabrication of nanooptical structures based on electron-beam lithography. Here, the need for structure sizes at the nanoscale necessitates special fabrication techniques suitable for reaching fabrication accuracies down to several nanometers. Additionally, careful characterization and testing of the single fabrication steps is needed, which is presented in detail. The second part of this chapter examines the deterministic positioning of nanoemitters on fabricated nanostructures. Due to the fact that the quality of nanoemitters (e.g. the concentration of defect centers and, therefore, their nonclassical single-photon emission behaviour) is not intrinsically predictable, pre-characterizing suitable emitters and subsequently transferring them to nanooptical structures is necessary. This so-called *pick-and-place* procedure involves several delicate steps, which - similar to the fabrication of nanostructures - have to be examined in detail.

Many of the fabrication and experimental processes presented in this chapter are rather technical procedures than physical ones. However, the author assumes (and knows from experience) that these facts might be highly relevant for future projects. Therefore, this chapter at times gives hands-on advice based on experience gained during this thesis. Some people might argue that nanofabrication itself is an art rather than a craft, a view which can be for the most part refuted. When it comes to nanofabrication, the essential ingredient is a thorough and methodical work procedure. As many fabrication steps are inherently susceptible to slight deviations in e.g. technical parameters or chemical concentrations, reproducibility is key.

A.1. Nanofabrication

Two different approaches are typically used for creating nanostructures like plasmonic metallic resonators on a plane surface, one is based on *focused-ion-beam milling* (or FIB milling) and one is based on *electron-beam lithography* (EBL). Both approaches have their own distinct advantages and disadvantages and, therefore, one may choose an approach depending on the special requirements.

For this thesis, nanostructures were typically created by means of EBL. For further structural analysis and post-processing of the structure (e.g. for creating additional single holes or slots), the created structures were sometimes subsequently processed by FIB milling. In the following, both methods are explained shortly. For further details, see for example [126].

A.1.1. Focused-Ion-Beam Milling

Especially for metallic structures like plasmonic resonators, a large majority of previous fabrication procedures were based on focused-ion-beam milling, a technique which uses a focused beam of accelerated ions with typical acceleration voltages of a few 10 kV for the direct removal of material. Typically, gallium ions are used for this task, although in recent years helium FIB machines gained some popularity due to their improved maximum resolution down to the sub-nm regime [127]. Possible reasons for this focus on FIB milling in creating metallic ring structures are manifold, although some of them are quite apparent: FIB milling is a very direct fabrication technique requiring only few fabrication steps. Additionally, the typical obtainable resolution and smoothness (e.g. the roughness of the structure's sidewalls) of the created structures are often superior to those created by e-beam lithography.

However, producing optically active nanostructures via focused-ion-beam milling also has some intrinsic drawbacks. The main drawback here is the technique itself: by physically etching the material via accelerated ions, strong doping of the material and, therefore, a change in the material properties occurs. In optical experiments, this manifests in a strongly increased autofluorescence of the created structure itself as well as a change in the physical properties of the material, for example the electric permittivity, and thus the refractive index. For plasmonic structures, these effects lead to a decrease in the performance as compared to a fabrication process based on e-beam lithography. See [128] for a comparative study of the two techniques on the strength of plasmonic resonances. Many of these drawbacks can be avoided by employing an electron-beam lithography based fabrication approach, where the desired structure is created by filling a lithographically defined shape, which acts as a negative, with evaporated metal. This separates the two steps of creating the form of the nanostructure from the deposition of metal, which also makes the process steps much more interchangeable if needed.

A.1.2. Electron-Beam Lithography

The basic requirement for lithography using a focused electron beam is an electron-sensitive resist, which changes its chemical properties upon exposure to the accelerated charges. Many of the commonly used EBL resists are based on polymer structures, the probably most famous

and widely used one is *poly methyl-methacrylate* (or PMMA) [129]. Being known in a hardened form as acrylic glass or plexiglass, PMMA as an electron resist consists of polymer chains with typical lengths of a few hundred thousand links, which are cracked to shorter polymer chains by the electron beam. This decrease in chain length enhances the solubility greatly and allows for chemical separation between the exposed and unexposed PMMA areas.

Figure A.1 illustrates the main fabrication steps towards creating plasmonic structures on a dielectric substrate. After initial cleaning of the substrate sample with acetone in an ultrasonic bath, isopropanol (IPA) and oxygen plasma, the sample was spin-coated with two layers of PMMA-500K 4% and a single layer of PMMA-950K 2%. Here, the spin-coating speed was 5000 rpm for 30 s. Each individual PMMA layer was soft-baked on a hotplate at 180° C for 2 min and cooled down before applying the next layer. The resulting layer thicknesses, which were measured via thin-film refractometry, were 160 nm for each of the PMMA-500K layer and 55 nm for the single PMMA-950K single layer, adding up to a total resist thickness of about 375 nm. There is a clear reason behind the rather complicated triple-layer resist structure, which is explained in detail in the following section.

As both the substrate and the PMMA layers are themselves isolating, an additional conductive polymer layer (AR-PC 5090 from Allresist) was spin-coated on the sample to serve as a discharge layer for the subsequent electron-beam exposure. The big advantage of the conductive polymer over a more conventional metallic discharge layer is its simplicity: Instead of employing time-consuming and complicated evaporation of a metallic film, a single spin-coating procedure is sufficient to create perfect discharge. Adding to this is the simple removal procedure of the polymer layer by dilution in deionized water, which leaves the underlying resist layers unaffected. This is in stark contrast to a metallic discharge film, which requires chemical etching or sputtering for its removal [126].

After applying the resist layers, the samples were patterned in an electron-beam lithography Raith-SmartSEM machine using electrons at 20 kV acceleration voltage. As the writing area, which the electron beam has to expose for one structure, is rather small, thousands of resonators with varying geometrical parameters could be realized on one single substrate easily. The quality of the written PMMA structures, especially the sidewalls, are highly sensitive to the exposure dose: While underexposure leads to an increased chance of loosing parts of the written PMMA structure in the development process, overexposure of the PMMA resist leads to increased roughness in the structure sidewall as cross-linking of PMMA between the interface of the exposed and unexposed areas increases and renders the edge less defined.

In preparation for using the exposed resist structure as a negative for the metallic ring structure, the exposed parts have to be removed. To this end, the conductive polymer layer was diluted in deionized water for 60 s. Afterwards, the PMMA resist structure was developed, i.e. the exposed parts were removed, by a high-contrast development solution of 1:3 MIBK:IPA mixture with added MEK for better contrast [130]. Here, gentle swinging of the sample in the mixture helps with the development. Too much of it, however, was found to increase the risk of small unexposed PMMA areas being detached from the surface. After 50 s, the process was stopped by washing the sample in isopropanol and drying it with nitrogen gas.

To use the created PMMA structure as a negative, a metallic film was deposited on the surface. This metal evaporation was performed in an ultra-high vacuum *electron-beam physical vapor deposition* (EBPVD) machine. Also for this procedure, optimized process parameters were

(a) Layer structure with two PMMA layers and a conduction copolymer layer spin-coated on a planar substrate

(b) Patterning of the layer structure with an electron beam

(c) Removal of the conducting copolymer

(d) Chemical removal of PMMA at the exposed areas

(e) Evaporation of a metallic layer

(f) Lift-off of the undeveloped PMMA areas
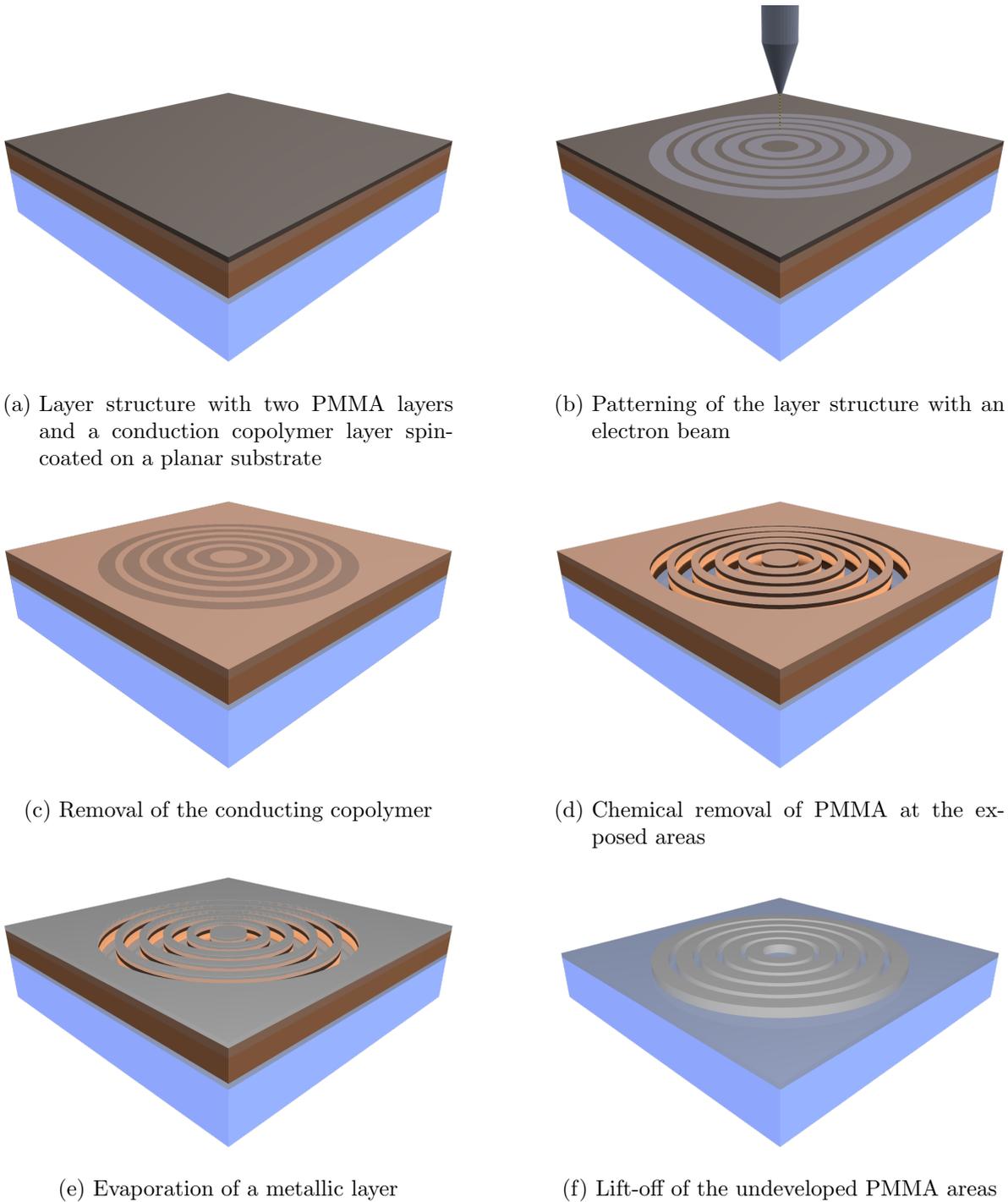
Figure A.1.: The main procedural steps for electron-beam lithography based fabrication of nanostructures. The basic principle of this fabrication technique is based on creating a PMMA negative of the desired structure with subsequent filling of this negative by evaporating material and a final lift-off of the unprocessed areas. A detailed description of the single steps is provided in the running text.

(a) Bad surface quality after Al evaporation

(b) Smooth surface after Al evaporation
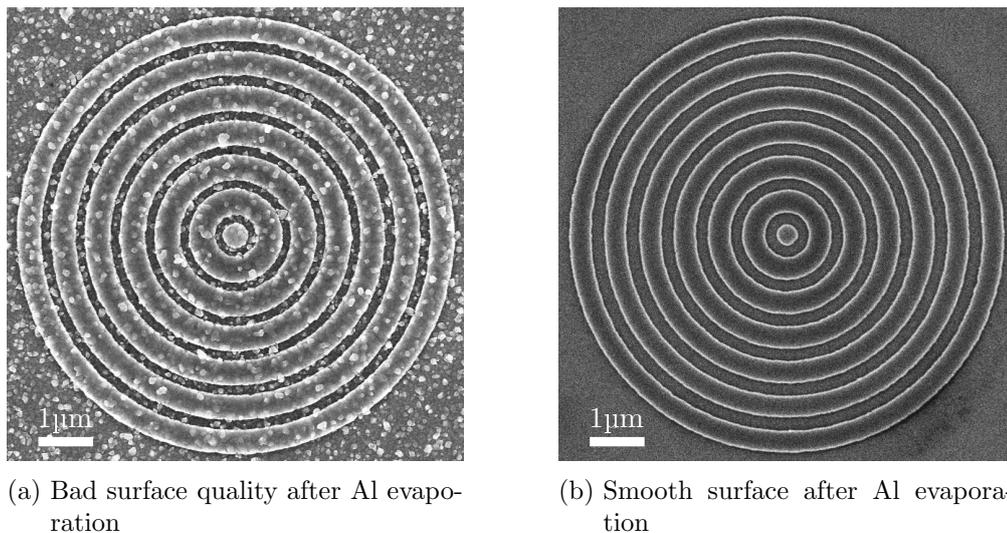
Figure A.2.: Comparison of fabricated aluminium ring structures on an aluminium base film of (a) not optimized and (b) optimized process parameters for the metal evaporation using SEM imaging.

needed to deposit smooth and even surfaces. This proved to be especially critical for the evaporation of aluminium: Figure A.2 compares SEM images of two plasmonic ring structure samples, one with and one without optimized evaporation parameters. Even at first glance, a tremendous difference in surface quality is visible, which influences the plasmonic properties greatly. The process differences between the evaporation tries was the aluminium target in the EBPVD chamber and the current of the heating electron beam. In general, smaller targets like powdered aluminium and slightly lower beam currents are favorable. This example also accentuates the fact that optical checks with a microscope during fabrication, which are often used for a routine and fast check of the fabrication process, are not always sufficient. Instead, high-resolution techniques like SEM imaging or AFM measurements might be necessary.

After depositing material on the PMMA form via evaporation, the unwanted metallic parts have to be removed by dissolving the remaining PMMA layers, which automatically removes the unwanted metal parts. Typically, strong solvents like acetone or *dimethyl sulfoxide* (DMSO) are employed for this task. Increasing the temperature of the solvent helps with the removal. The best results were obtained by heating acetone in a closed container to about 80 °C, which is well above boiling point and requires additional caution. Additionally, mechanical loosening of the sample by means of gentle ultrasonic baths further assist the lift-off process.

Choice of the PMMA Layer Structure

One particularly important aspect when performing electron-beam lithography is to choose an appropriate resist layer structure for the task at hand, which assists the subsequent fabrication steps. Depending on the usage of the created resist structure, different types of resists can be employed.

The most fundamental classification of resist chemicals is their behaviour after exposure to an accelerated electron beam and the development of the resist: For *negative tone* resists, the lithography procedure results in structures, which correspond to the exposed area. Unexposed areas in negative tone resists are diluted and removed from the surface. In contrast, *positive tone* resists form a negative image of the exposed structure, meaning that the exposed parts are removed in the development process. For fabricating structures on the nanoscale, the *resolution* of the resist is of great importance. In this context, resolution means the ability to create small structures within the resist with sharp, well-defined edges. Examples for high-resolution electron-sensitive resists are *hydrogen silsesquioxane* (HSQ), which is a negative tone resist and the already mentioned PMMA, which falls in the positive tone category. Both resists were investigated for their usage in high-resolution e-beam lithography during this thesis. The results of this investigation are described in detail in [131]. In the following, the choice of the PMMA layer structure for the creation of plasmonic bullseye resonators is explained in detail. However, the same effects and their possible solutions can be applied to negative tone resists like HSQ.

When choosing an appropriate resist structure, its interplay with the penetrating electron beam has to be taken into account. This includes the width of the beam and especially the acceleration energy of the electrons. Figure A.3 illustrates this fact by comparing the electron density of a focused electron beam entering a 200 nm thick layer of PMMA on top of a fused silica substrate. The two-dimensional simulations were performed using Monte Carlo techniques simulating 10^6 electron trajectories each and assume an intrinsic beam width in the nanometer range and kinetic energies of 10 keV and 20 keV.

(a) 10 keV (b) 20 keV
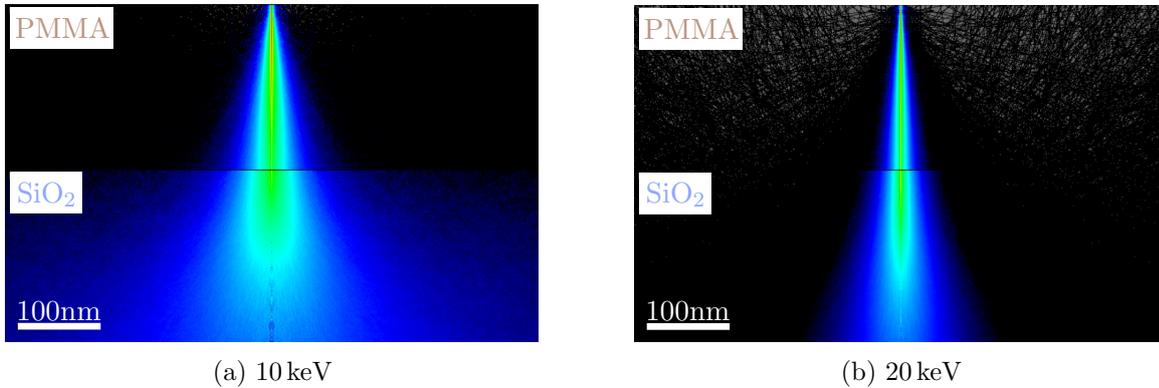
Figure A.3.: Monte Carlo simulations of the electron density for a focused electron beam entering a 200nm layer of PMMA for A.3(a) 10 kV and A.3(b) 20 kV acceleration voltage. For the larger voltage, the forward scattering is much stronger resulting in a much smaller exposed volume and less undercut.

For both acceleration voltages, a cone-like structure is visible. This shape is governed by the amount of secondary electrons created by the penetrating electrons and their scattering behaviour inside the medium. For higher electron energies, scattering in forward directions is much more likely. This results in a much sharper cone for larger acceleration voltages and, therefore, a much smaller effectively exposed area. In this regard, the cone-like resist structure, which is formed by the electron beam and the subsequent development, i.e. the removal of the exposed PMMA areas, is called the *undercut* of the resist [132]. This corresponds to the

minimal geometrical sizes realizable by e-beam lithography: Exposure experiments showed that the minimal feature size for 10 keV and a typical PMMA 950K resist with 170 nm in thickness is in the range of about 80 to 100 nm, for 20 keV it is in the range of 50 to 60 nm. The exact numbers, however, strongly depend on the employed resist and the quality of the electron beam shape.

(a) Low acceleration voltages for the electron beam creates crosstalk between exposed areas

(b) Increasing the acceleration voltage enables smaller exposed volumes

(c) Insufficient undercut of the exposed resist induces crosslinking

(d) Using two PMMA layers with different sensitivity increases the undercut for closely positioned structures.
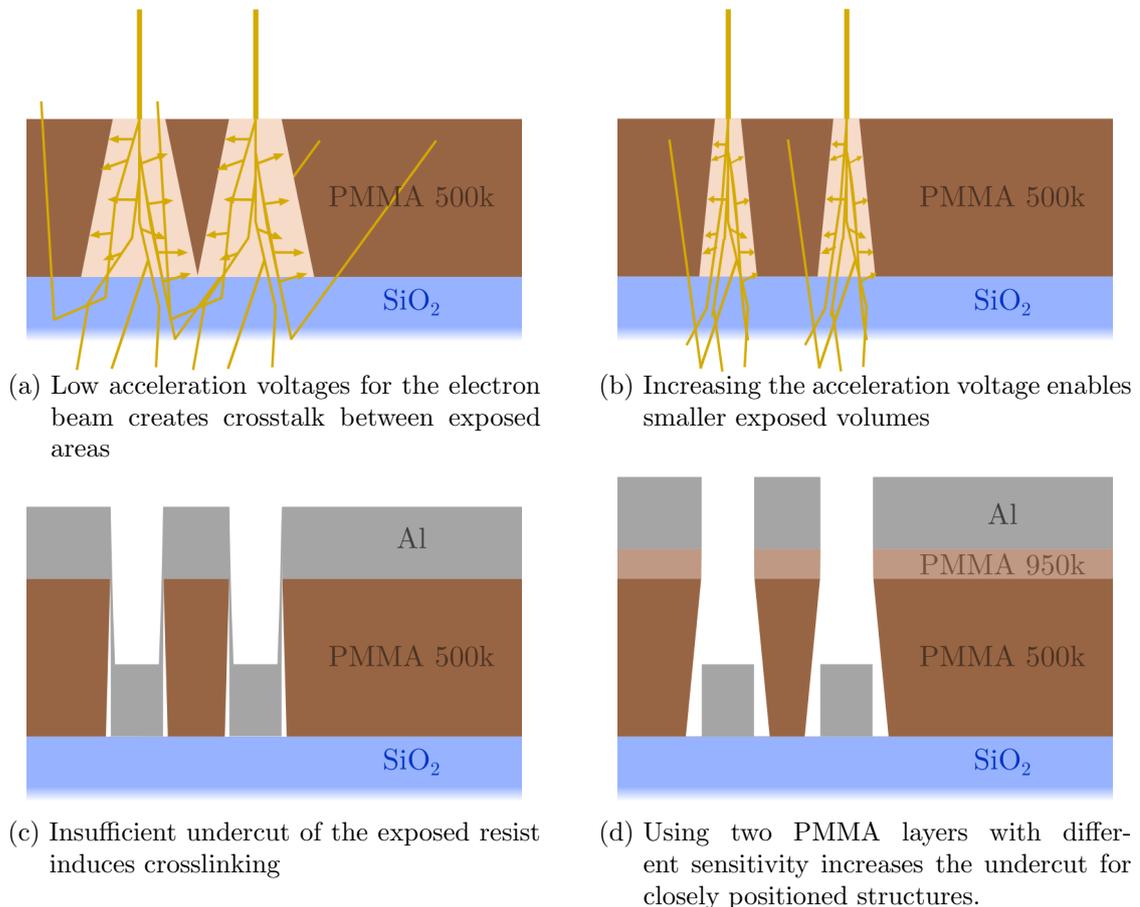
Figure A.4.: Cross-sectional view of typical effects of electron-beam lithography at the nanoscale and their potential solutions. (a) Low acceleration voltages increase the effectively exposed volume and induces crosstalk between exposed areas. (b) and (c) Higher acceleration voltages reduce this effect at the cost of a decreased undercut. (d) The usage of a double-layer approach with different sensitivities increases the undercut and allows for smooth structures in close proximity.

The optimal acceleration voltage in e-beam lithography is dependent on several parameters like the size of the structure to be written or the subsequent steps necessary, e.g. the usage of the resist layer as a negative. Figure A.4 illustrates several cases via a cross-sectional view. For isolated structures, which are much larger than the minimal achievable size of the lithography process, the acceleration voltage can be comparatively low as a larger undercut makes most subsequent fabrication steps easier. However, when using larger resist thicknesses, writing geometries in proximity with each other can lead to the problem of crosstalk between two adjacent exposure areas. Figure A.4(a) illustrates this effect, in which the created undercuts

are in close contact with each other or even overlap. This can be circumvented by increasing the acceleration voltage as depicted in figure A.4(b).

In general, a large undercut is favorable when using the PMMA resist as a negative. Figure A.4(c) illustrates the effect of *crosslinking* when evaporating material on a resist structure with insufficient undercut. As the evaporation is not perfectly anisotropic, for large evaporated films a connection between parts under the resists and above the resist can occur. This can lead to insufficient liftoff results or bad structure edges as the crosslink points are either not removed or pulled off by force, which can break the structure edges.

One possible solution to this fundamental trade-off problem of insufficient undercut and adjacent structures in close proximity is to combine resist layers with different sensitivities with regard to the electron beam. For PMMA, this is easily achievable by choosing the intrinsic average chain length of the material. For example, in the chosen resist structure, PMMA with a length of 950k is combined with PMMA 500k. The latter is by default shorter and thus more susceptible to impinging electrons. With this configuration, both large acceleration voltages can be employed as well as large undercuts for the material deposition, which is illustrated in figure A.4(d). A series of fabrication tests with different film thicknesses and PMMA types was conducted and analyzed by SEM imaging. This revealed an optimum resist structure consisting of a double layer of PMMA 500k 4% and a single layer of PMMA 950k 2%.

A.2. Nanopositioning of Colour Centers in Nanodiamonds

The main goal of nanopositioning for this thesis is to manipulate and control the location of a nanoemitter with high accuracy. This goal can be seen in the context of creating a hybrid system, where the emitter is chosen independently from the surrounding nanostructure. Chapter 4 explains the optical experimental setup for analyzing the response of a photoluminescing system. In the previous sections, the fabrication process for creating nanostructures is presented. In the following, two approaches for combining quantum emitters and created nanostructures are presented. One is based on a spin-coating approach, where the resulting position of nanodiamonds is not predetermined. The other approach, labeled *pick-and-place*, can be described as an attempt to directly manipulate the position of pre-characterized nanodiamonds.

A.2.1. Spin-Coating of Nanodiamonds

Spin-coating of nanodiamonds or any other solid-state quantum emitter, can be characterized as a statistical approach: By applying a liquid solution of nanodiamonds in water or other solvents like ethanol and a subsequent spin-coating step, quantum emitters are distributed over the sample surface in a random manner [133]. Here, the final position of the emitters depends greatly on the topography of surface: Introducing markers or structures with sharp edges and sufficient height like the already described metallic ring resonators greatly increase the chance that nanodiamonds bind to the edges of the structure.

To counteract this effect, the structure topography can be flattened by a covering layer: In case of bullseye resonator structures, an additional PMMA 950k 2% layer was spin-coated on top

of the sample. Due to this layer, the intrinsically sharp features of the structures are smoothed out and create a wavy surface, by which the chance that a spin-coated nanodiamond positions itself in the center of a structure is greatly increased. The chance for a successful placement of a nanodiamond in the structure center can be further increased by increasing the number of resonator sites on the surface. As the fabrication process allows for mass-production of resonators, typical samples employed for the spin-coating of nanodiamonds featured several thousand resonator structures. However, increasing the number of resonators also increases the number of places, one has to investigate for a possibly correctly placed nanoemitter.

In general, for spin-coating of nanodiamonds on PMMA layers, the degree of hydrophilicity of the PMMA layer has to be taken into account. Like most polymers, PMMA is normally highly hydrophobic. Therefore, spin-coating of nanoparticles in a water based solution results in a very low density of nanoparticles on the surface. For this reason, the PMMA layer has to be pre-treated via oxidation. Typically, this is performed either wet-chemically or by using oxygen plasma. In both cases, the pre-treatment leads to the formation of additional carbon-oxygen groups at the PMMA surface, which can greatly increase the hydrophilicity (for more details, see e.g. [134]). Additionally, when treating PMMA with an oxygen plasma, the etching of the PMMA has to be taken into account. For this thesis, a short oxygen plasma etch of 10 to 20 seconds was performed. Longer etching times tended to seriously alter the PMMA surface or removing it altogether. Typical etch rates for PMMA layers can be found in e.g. [135].

During this thesis, several attempts to position nanodiamonds in the center of aluminium bullseye resonators via spin-coating were undertaken. Using the pre-treatment of the PMMA layer with oxygen plasma, this resulted in several resonator sites featuring a fluorescent nanodiamond in its center. One of two main drawbacks of this approach is its inherently statistical nature, which makes searching for a correctly positioned nanodiamond with AFM topography scans tedious. Another drawback is the lack of pre-characterizing nanodiamonds before positioning them on the bullseye surface. This can be a major problem for quantum emitters like colour centers in diamond, which vary greatly in their optical properties.

A.2.2. The Pick-and-Place Procedure

The shortcomings of the spin-coating approach for controlled positioning of nanodiamonds in the center of ring resonators can be circumvented by employing a more direct approach, where a pre-chosen emitter is directly transferred from its original place to the bullseye center and positioned there with high accuracy. The procedure, which was applied for this task during this thesis, is called *pick-and-place*. As the name suggests, the workflow here is to *pick up* a suitable diamond and *place* it on a pre-chosen position on top or in the center of a nanostructure [136].

This transfer of the nanodiamond is performed with the help of an *atomic force microscope* (AFM). In essence, an AFM is a sharp movable tip, whose deflection is recorded as it is directly correlated to both the topography of the sample and the interaction between tip and substrate. While this very simplistic view is sufficient for explaining the pick-and-place procedure, atomic force measurements are employed in a wide variety of experiments and

measurement techniques. A more detailed explanation of the working principle and various different types of possible usages can be found in e.g. [137].

Basic Working Procedure

A schematic overview of the main steps is presented in figure A.5, the basic procedure is also described in detail in [21, 136]. The hybrid experimental setup used for the procedure consists of a confocal photoluminescence setup and an atomic force microscope, which is presented in in-depth in section 4.1. The first part of the pick-and-place procedure is the search for a suitable quantum emitter. Here, both the optical properties and the geometrical parameters, i.e. the size of the emitter, have to be investigated. Once a suitable emitter is found, the pick-up procedure starts. For this thesis, mainly gold-coated silicon cantilevers were used (*Multi75GB-G* from *Budget Sensors*), which needed to be blunted: Intrinsically, such a cantilever tip should be as sharp as possible as the tip size directly corresponds with the lateral resolution of the AFM. Here, however, some contact area between the nanodiamond and the cantilever tip is needed in order to bind the nanodiamond to the cantilever tip adhesively via surface van der Waals forces [138].

The blunting procedure itself incorporates several lithography steps near the pre-chosen nanodiamond. Figure A.6 shows AFM measurements before and after this procedure. The progress on the blunting procedure can be directly monitored by scanning the nearby nanodiamond and observing the worsening of the AFM image resolution: The essential limitation to AFM topography measurements is the diameter or sharpness of the cantilever tip. Worsening of the lateral resolution, therefore, is a direct measure of tip blunting. This resolution deterioration can be directly seen by comparing the atomic force microscope measurements before and after blunting: Comparing the AFM scan in figure A.6(a) to an AFM scan of the same area after the blunting in figure A.6(b) clearly shows the decreased measurement resolution. Additionally, debris from the lithography process can be observed.

The process of picking up a nanodiamond is then a combination of repeatedly pressing on the nanodiamond with the AFM tip and periodic optical checks whether the fluorescing diamond is still present on the surface or binding to the tip. A detailed description about the experimental parameters and the possible measurement schemes for the picking up is given in [139]. Previous experiments employing the pick-and-place procedure of nanodiamonds used small nanocrystals with average sizes of 20 nm to 40 nm hosting single NV centers [21, 46]. Adapting the tested procedure for positioning much larger nanodiamonds with average sizes in the range of 150 nm to 200 nm hosting SiV centers proved to be challenging as the size and, therefore, the mass of the nanocrystal is much larger. Even though the contact area between nanodiamond and AFM tip increases to some degree too, the relative binding strength of large nanocrystals is rather weak.

For this reason, optimum binding had to be ensured. One major parameter for the adhesion is the relative air humidity, which had to be actively controlled to a high degree. Especially in laboratories with air conditioning, this proved to be the crucial step for a successful pick-and-place procedure. To this end, the humidity in experimental setup, which was housed under a flow-box, was controlled by a home-built air humidifier system with a sensor-based
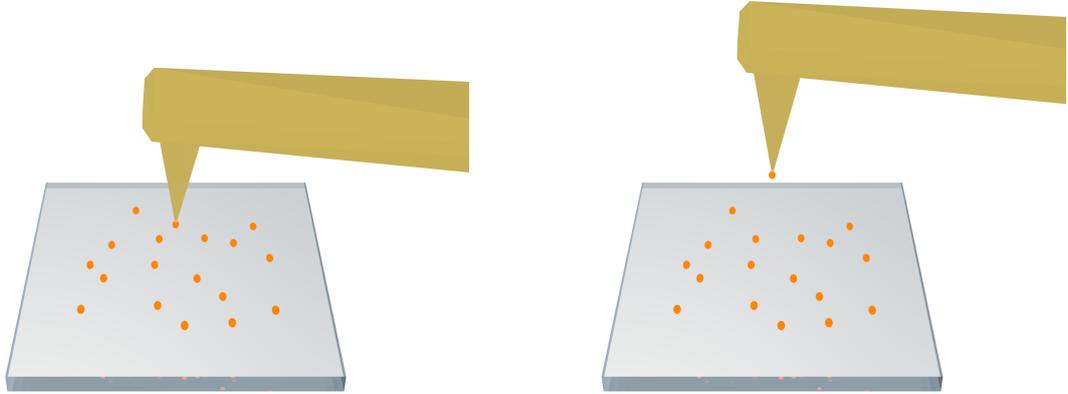
(a) Nanodiamonds on a glass substrate are optically and topographically pre-characterized

(b) After repeatedly pressing on a nanodiamond with a blunted AFM cantilever, a chosen nanodiamond is picked up
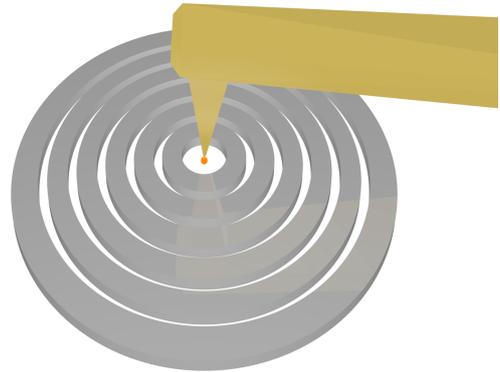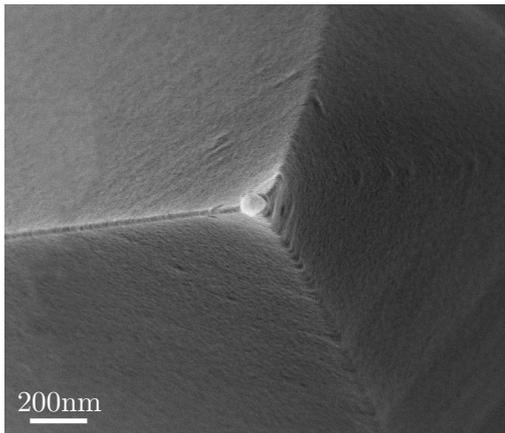
(c) SEM image of a picked-up nanodiamond on a blunted cantilever tip

(d) Deterministic placing of the nanodiamond in the center of a plasmonic bullseye resonator

Figure A.5.: Nanomanipulation of pre-chosen nanodiamonds. (a) Nanodiamonds are optically and topographically pre-characterized using a home-built photoluminescence setup in combination with an atomic force microscope (AFM). (b) After choosing a suitable nanodiamond, the AFM tip is blunted and the nanodiamond is picked up by repeated pressing on the nanodiamond with the flattened AFM tip. (c) SEM image of a picked-up nanodiamond on top of a blunted AFM cantilever tip. (d) Finally, the nanodiamond is deterministically positioned in the center of a plasmonic bullseye resonator

(a) AFM scan before tip blunting

(b) AFM scan after tip blunting
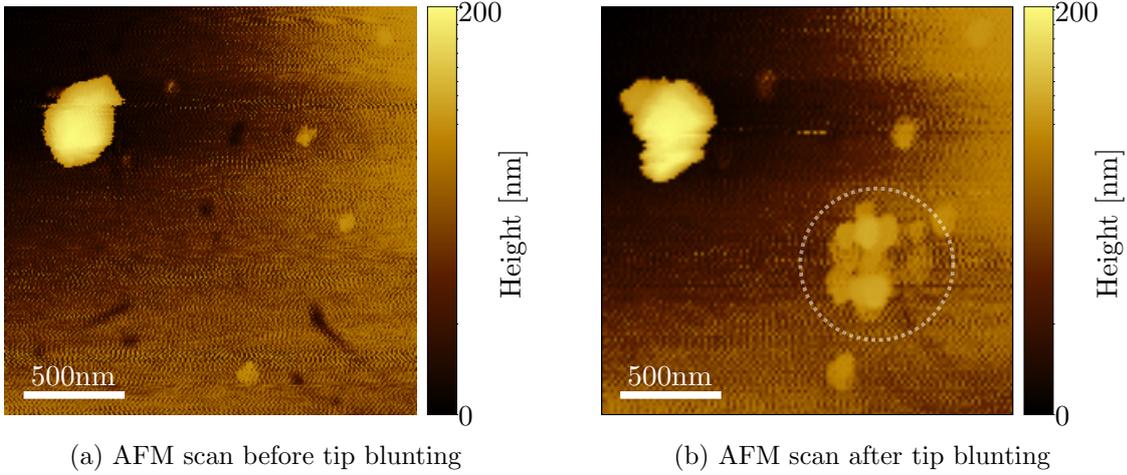
Figure A.6.: AFM images of a nanodiamond (a) before and (b) after blunting of the cantilever tip. In the area in (b) marked with a white circle, debris of the tip scratching procedure is visible. Additionally, due to blunting of the tip a decrease of the image resolution from (a) to (b) can be observed.

feedback loop. With this, the humidity could be controlled within $\pm 2\%$. A series of pick-up tests on nanodiamonds with crystal sizes between $150\,\text{nm}$ and $250\,\text{nm}$ then revealed an optimum relative air humidity of 65%.

Figure A.5(c) shows a nanodiamond being adhesively bonded to an evenly blunted AFM tip. Once a nanodiamond is picked up successfully, the AFM system can be transferred to a nanostructure sample and the nanodiamond can be placed inside the structure. In case of strongly binding surfaces like the oxygen-plasma treated PMMA surface used for this thesis, which is described in the previous section, this can be achieved by simply pressing the nanodiamond on the sample. Here, the positioning accuracy of the AFM tip holding the nanodiamond relative to the sample surface is important. There are different ways to determine the actual position where the nanocrystal should be positioned. For conducting surfaces, measuring the electrostatic force change, which appears when applying a strong voltage potential between tip and surface, allows for contactless positioning [140]. Alternatively, the surface topography can be scanned by a standard dynamic mode AFM measurement with the nanocrystal attached to the cantilever. This approach was chosen for its simplicity and worked quite well assuming that the AFM excitation amplitude is chosen small enough.

After placing the nanodiamond on the surface, additional fine-tuning of the diamond position is possible by pushing the nanoparticle laterally. A theoretical model for the dynamics of this procedure can be found in [141]. When using appropriate tip forces and speeds, which have to be determined by independent tests as they depend heavily on the interaction strength between nanoparticle and surface, the final positioning accuracy is mainly determined by the intrinsic resolution of the AFM system and in the range of 10 to $20\,\text{nm}$.

Possible Errors

Having tested all parameters of the pick-and-place procedure, the success probability for placing a pre-chosen nanodiamond on a nanostructure is reasonable high and can be - due to a lack of large statistics - roughly estimated to be about 20% for the larger nanocrystals employed for this thesis. This means that roughly four out of five tries aren't successful. A detailed investigation of possible pitfalls during the procedure revealed several main potential sources for errors one has to watch out for. They are shortly presented in this section.

As already mentioned in the previous section, the probably most influential parameter for a successful transfer of a nanodiamond is sufficient binding of the nanocrystal to the AFM tip, which is mainly influenced by the relative air humidity. Initially, the pick-and-place procedures were conducted in a laboratory without air conditioning and worked reasonably well. After installing an AC unit, however, the success rate dropped dramatically and precise control of the correct humidity level was necessary.
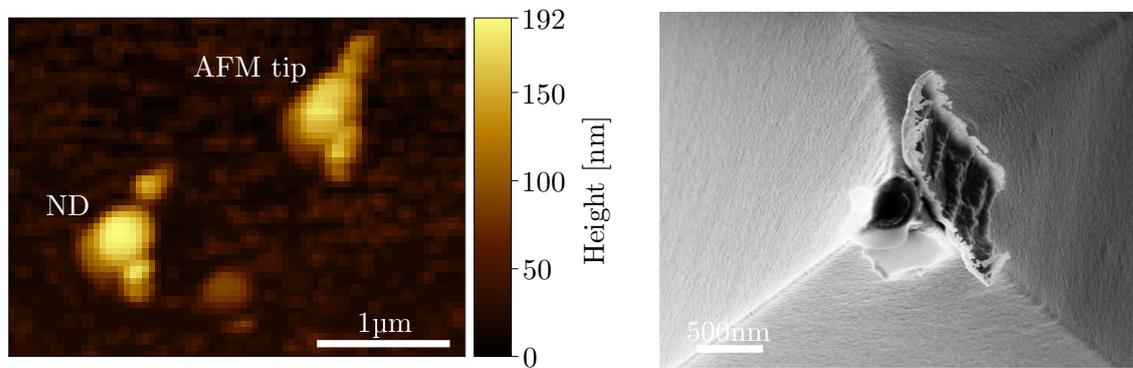
(a) AFM image of a broken-off tip while blunting on the side of a nanodiamond

(b) SEM image of (a) with additional PMMA debris on the tip side
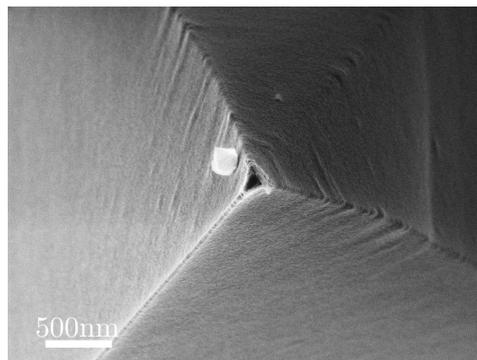
(c) SEM image of a nanodiamond on the side of a tip.

Figure A.7.: Possible errors during the pick-and-place procedure: (a) AFM image of a nanodiamond (ND) and an unevenly broken off AFM tip while blunting. (b) Corresponding SEM image of the crookedly blunted AFM tip from (a) after a placement try. Additional PMMA debris surrounds the blunted region. (c) SEM image of a nanodiamond slipped to the side of a blunted AFM tip.

Additional typical sources of unsuccessful pick-and-place tries, which were frequently encountered, are shown in figure A.7. One is caused by striking differences in the mechanical properties of the gold-coated AFM cantilevers: While they are mass-produced by anisotropic silicon etching and, therefore, nominally identical [142], their hardness at the tip varied greatly. This makes the blunting procedure in the beginning of the picking up phase challenging as too much force on a too brittle cantilever causes uneven or crooked breaking of the tip. Figure A.7(a) illustrates this effect with an AFM image taken after an unsuccessful blunting try: While performing lithography at an empty place next to a pre-chosen nanodiamond, the AFM tip was broken off. The resulting crocked contact surface at the cantilever end can be seen in the SEM image of the tip in figure A.7(b). At this point, the AFM tip cannot be used anymore and has to be replaced, starting a new pick-and-place try.

Another common error occurs while pressing on the nanodiamond with the blunted AFM tip. If the tip does not press on the crystal centrally, chances are that the diamond slips away and binds to the side of the AFM tip. A SEM image of such a case is shown in figure A.7(c). This is dreadful in two respects: On the one hand, the pre-chosen nanodiamond is lost and a new crystal with appropriate dimensions and optical properties has to be chosen. On the other hand, the AFM tip should not be used anymore as there is a chance that the nanodiamond on the side of the tip falls off and places itself in an unfavorable position, for example in one of the concentric grooves of a plasmonic bullseye resonator.

Bibliography

[1] K. Haefner. *Evolution of information processing systems: an interdisciplinary approach for a new understanding of nature and society.* Springer Science & Business Media, 2012.

[2] S. Barnett. *Quantum information*, volume 16. Oxford University Press, 2009.

[3] D. P. DiVincenzo. Quantum Computation. *Science*, 270(5234):255–261, 1995, doi:10.1126/science.270.5234.255.

[4] J. J. Pla, K. Y. Tan, J. P. Dehollain, W. H. Lim, J. J. Morton, F. A. Zwanenburg, D. N. Jamieson, A. S. Dzurak, and A. Morello. High-fidelity readout and control of a nuclear spin qubit in silicon. *Nature*, 496(7445):334–338, 2013, doi:10.1038/nature12011.

[5] M. Anderlini, P. J. Lee, B. L. Brown, J. Sebby-Strabley, W. D. Phillips, and J. V. Porto. Controlled exchange interaction between pairs of neutral atoms in an optical lattice. *Nature*, 448(7152):452–456, 2007, doi:10.1038/nature06011.

[6] J. E. Mooij, T. P. Orlando, L. Levitov, and L. Tian. Josephson Persistent-Current Qubit. *Science*, 285(5430):1036–1039, 1999, doi:10.1126/science.285.5430.1036.

[7] J. M. Martinis, S. Nam, J. Aumentado, and C. Urbina. Rabi Oscillations in a Large Josephson-Junction Qubit. *Physical Review Letters*, 89(11):9–12, 2002, doi:10.1103/PhysRevLett.89.117901.

[8] M. Fox. *Quantum optics: an introduction*, volume 15. OUP Oxford, 2006.

[9] X. Maître, E. Hagley, G. Nogues, C. Wunderlich, P. Goy, M. Brune, J. M. Raimond, and S. Haroche. Quantum memory with a single photon in a cavity. *Physical Review Letters*, 79(4):769–772, 1997, doi:10.1103/PhysRevLett.79.769.

[10] T. Durt. Comment on "pulsed energy-time entangled twin-photon source for quantum communication". *Physical Review Letters*, 86(7):1392, 2001, doi:10.1103/PhysRevLett.86.1392.

[11] B. Huttner, N. Imoto, N. Gisin, and T. Mor. Quantum cryptography with coherent states. *Physical Review A*, 51(3):1863–1869, 1995, doi:10.1103/PhysRevA.51.1863.

[12] H. K. Lo, X. Ma, and K. Chen. Decoy state quantum key distribution. *Physical Review Letters*, 94(23):15–18, 2005, doi:10.1103/PhysRevLett.94.230504.

[13] L. Mandel. Sub-Poissonian photon statistics in resonance fluorescence. *Optics Letters*, 4(7):205, 1979, doi:10.1364/ol.4.000205.

Bibliography

[14] J. F. Clauser. Experimental distinction between the quantum and classical field-theoretic predictions for the photoelectric effect. *Physical Review D*, 9(4):853–860, 1974, doi:10.1103/PhysRevD.9.853.

[15] L. Davidovich. Sub-Poissonian processes in quantum optics. *Reviews of Modern Physics*, 68(1):127–173, 1996, doi:10.1103/RevModPhys.68.127.

[16] A. Ashkin. Trapping of atoms by resonance radiation pressure. *Physical Review Letters*, 40(12):729–732, 1978, doi:10.1103/PhysRevLett.40.729.

[17] P. Michler, A. Kiraz, C. Becher, W. V. Schoenfeld, P. M. Petroff, L. Zhang, E. Hu, and A. Imamoğlu. A quantum dot single-photon turnstile device. *Science*, 290(5500):2282–2285, 2000, doi:10.1126/science.290.5500.2282.

[18] B. Lounis and W. E. Moerner. Single photons on demand from a single molecule at room temperature The generation of non-classical states of light. *Nature*, 407(28):491–493, 2000, doi:10.1038/35035032.

[19] C. Kurtsiefer, S. Mayer, P. Zarda, and H. Weinfurter. Stable solid-state source of single photons. *Physical Review Letters*, 85(2):290–293, 2000, doi:10.1103/PhysRevLett.85.290.

[20] S. Strauf, P. Michler, M. Klude, D. Hommel, G. Bacher, and A. Forchel. Quantum optical studies on individual acceptor bound excitons in a semiconductor. *Physical Review Letters*, 89(17):177403–177407, 2002, doi:10.1103/PhysRevLett.89.177403.

[21] L. Liebermeister, F. Petersen, A. V. Münchow, D. Burchardt, J. Hermelbracht, T. Tashima, A. W. Schell, O. Benson, T. Meinhardt, A. Krueger, A. Stiebeiner, A. Rauschenbeutel, H. Weinfurter, and M. Weber. Tapered fiber coupling of single photons emitted by a deterministically positioned single nitrogen vacancy center. *Applied Physics Letters*, 104(3), 2014, doi:10.1063/1.4862207.

[22] E. A. J. Marcatili. Slab-coupled waveguides. *Bell System Technical Journal*, 53(4):645–674, 1974, doi:10.1002/j.1538-7305.1974.tb02762.x.

[23] A. W. Snyder and J. Love. *Optical Waveguide Theory*. Springer Science & Business Media, 1st edition, 1983. doi:10.1007/978-1-4613-2813-1.

[24] D. Pines. A collective description of electron interactions: IV. Electron interaction in metals. *Physical Review*, 92(3):626–636, 1953, doi:10.1103/PhysRev.92.626.

[25] S. A. Maier. *Plasmonics: fundamentals and applications*. Springer Science & Business Media, 2007.

[26] M. S. Tame, K. R. McEnery, S. K. Özdemir, J. Lee, S. A. Maier, and M. S. Kim. Quantum plasmonics. *Nature Physics*, 9(6):329–340, 2013, doi:10.1038/nphys2615.

[27] A. Vial, A. S. Grimault, D. Macías, D. Barchiesi, and M. Lamy De La Chapelle. Improved analytical fit of gold dispersion: Application to the modeling of extinction spectra with a finite-difference time-domain method. *Physical Review B - Condensed Matter and Materials Physics*, 71(8):1–7, 2005, doi:10.1103/PhysRevB.71.085416.

[28] W. S. Werner, K. Glantschnig, and C. Ambrosch-Draxl. Optical constants and inelastic electron-scattering data for 17 elemental metals. *Journal of Physical and Chemical Reference Data*, 38(4):1013–1092, 2009, doi:10.1063/1.3243762.

[29] S. K. Gray, G. Davy, S. K. Gray, D. Gerard, and S. K. Gray. Aluminium plasmonics. *Journal of Physics D: Applied Physics*, 48(18), 2015, doi:10.1088/0022-3727/48/18/184001.

[30] K. M. McPeak, S. V. Jayanti, S. J. Kress, S. Meyer, S. Iotti, A. Rossinelli, and D. J. Norris. Plasmonic films can easily be better: Rules and recipes. *ACS Photonics*, 2(3):326–333, 2015, doi:10.1021/ph5004237.

[31] A. Hohenau, A. Drezet, M. Weißenbacher, F. R. Aussenegg, and J. R. Krenn. Effects of damping on surface-plasmon pulse propagation and refraction. *Physical Review B - Condensed Matter and Materials Physics*, 78(15):1–9, 2008, doi:10.1103/PhysRevB.78.155405.

[32] R. A. Serway and J. W. Jewett. *Principles of physics*, volume 1. Saunders College Pub. Fort Worth, TX, 1998.

[33] A. Taflove and S. C. Hagness. *Computational Electrodynamics: The Finite-Difference Time-Domain Method.* Artech House, 3rd edition, 2005.

[34] A. Taflove, A. Oskooi, and S. G. Johnson. *Advances in FDTD Computational Electrodynamics: Photonics and Nanotechnology.* Artech house, 2013.

[35] Z. Zhu and T. Brown. Full-vectorial finite-difference analysis of microstructured optical fibers. *Optics Express*, 10(17):853, 2002, doi:10.1364/oe.10.000853.

[36] S. Johnson and J. Joannopoulos. Block-iterative frequency-domain methods for Maxwell's equations in a planewave basis. *Optics Express*, 8(3):173, 2001, doi:10.1364/oe.8.000173.

[37] J. J. D. Joannopoulos, S. Johnson, J. N. J. Winn, and R. R. D. Meade. *Photonic crystals: molding the flow of light.* Princeton University Press, 2008. doi:10.1063/1.1586781.

[38] D. M. Sullivan. *Electromagnetic simulation using the FDTD method.* John Wiley & Sons, 2013.

[39] A. F. Oskooi, D. Roundy, M. Ibanescu, P. Bermel, J. D. Joannopoulos, and S. G. Johnson. Meep: A flexible free-software package for electromagnetic simulations by the FDTD method. *Computer Physics Communications*, 181(3):687–702, 2010, doi:10.1016/j.cpc.2009.11.008.

[40] T. Liebig, A. Rennings, S. Held, and D. Erni. openEMS – a free and open source equivalent-circuit (EC) FDTD simulation platform supporting cylindrical coordinates suitable for the analysis of traveling wave MRI applications. *International Journal of Numerical, Modelling, Electronic Networks, Devices and Field*, 26(6):680–696, 2013, doi:10.1002/jnm.

[41] Lumerical Inc. Lumerical FDTD Solutions. URL `https://www.lumerical.com/`.

Bibliography

[42] M. Zeitlmair, L. Liebermeister, W. Rosenfeld, and H. Weinfurter. Optimization of Nanodiamond Based Dielectric Single-Photon Sources. In D. Kranzmüller, H. Brüchle, and M. Brehm, editors, *High Performance Computing in Science and Engineering - on the Tier-2 System CoolMUC*, pages 14–15. Leibnitz Supercomputing Centre, Garching/München, 2018.

[43] J. B. Schneider. Understanding the finite-difference time-domain method. *School of electrical engineering and computer science Washington State University*, pages 1–28, 2010.

[44] E. Hecht. *Optik*. Oldenbourg Wissenschaftsverlag, München, 3 edition, 2001.

[45] S. Tanzilli, A. Martin, F. Kaiser, M. P. de Micheli, O. Alibart, and D. B. Ostrowsky. On the genesis and evolution of integrated quantum optics. *Laser and Photonics Reviews*, 6(1):115–143, 2012, doi:10.1002/lpor.201100010.

[46] L. Liebermeister. *Photonic Waveguides Evanescently Coupled with Single NV-centers*. Phd thesis, LMU München, 2015.

[47] T. M. Monro and S. Afshar V. A full vectorial model for pulse propagation in emerging waveguides with subwavelength structures part II: Stimulated Raman Scattering. *Optics Express*, 17(14):11565, 2009, doi:10.1364/oe.17.011565.

[48] G. Agrawal. Nonlinear Fiber Optics. In *Nonlinear Fiber Optics*. Elsevier - Academic Press, 5 edition, 2006. doi:10.1016/B978-0-12-369516-1.X5000-6.

[49] S. Noda, M. Fujita, and T. Asano. Spontaneous-emission control by photonic crystals and nanocavities. *Nature Photonics*, 1(8):449–458, 2007, doi:10.1038/nphoton.2007.141.

[50] M. Aspelmeyer, T. J. Kippenberg, and F. Marquardt. Cavity optomechanics. *Rev. Mod. Phys.*, 86(4):1391–1452, 2014, doi:10.1103/RevModPhys.86.1391.

[51] H. Kaupp, C. Deutsch, H. C. Chang, J. Reichel, T. W. Hänsch, and D. Hunger. Scaling laws of the cavity enhancement for nitrogen-vacancy centers in diamond. *Physical Review A - Atomic, Molecular, and Optical Physics*, 88(5):1–8, 2013, doi:10.1103/PhysRevA.88.053812.

[52] V. R. Almeida, Q. Xu, C. A. Barrios, and M. Lipson. Guiding and confining light in void nanostructure. *Optics Letters*, 29(11):1209–1211, 2004, doi:10.1364/OL.29.001209.

[53] C. A. Barrios, B. Sánchez, K. B. Gylfason, A. Griol, H. Sohlström, M. Holgado, and R. Casquel. Demonstration of slot-waveguide structures on silicon nitride/silicon oxide platform. *Optics express*, 15(11):6846–6856, 2007, doi:10.1364/OE.15.006846.

[54] A. H. Yang, S. D. Moore, B. S. Schmidt, M. Klug, M. Lipson, and D. Erickson. Optical manipulation of nanoparticles and biomolecules in sub-wavelength slot waveguides. *Nature*, 457(7225):71–75, 2009, doi:10.1038/nature07593.

[55] K. K. Lee, D. R. Lim, L. C. Kimerling, J. Shin, and F. Cerrina. Fabrication of ultralow-loss Si/SiO(2) waveguides by roughness reduction. *Optics letters*, 26(23):1888–1890, 2001, doi:10.1364/OL.26.001888.

[56] F. Grillot, L. Vivien, S. Laval, D. Pascal, and E. Cassan. Size influence on the propagation loss induced by sidewall roughness in ultrasmall SOI waveguides. *IEEE Photonics Technology Letters*, 16(7):1661–1663, 2004, doi:10.1109/LPT.2004.828497.

[57] M. Goeppel. *Studien über Transmissionsverhalten und Propagationsverluste bei dielektrischen Ta_2O_5-Wellenleitern.* Bachelor thesis, Ludwig-Maximilians-Universität München, 2015.

[58] M. Lichtenegger. *Simulation and Charakterisierung von dielektrischen Ta_2O_5-Wellenleitern.* Bachelor thesis, Ludwig-Maximilians-Universität München, 2016.

[59] N.-N. Feng, R. Sun, L. C. Kimerling, and J. Michel. Lossless strip-to-slot waveguide transformer. *Optics Letters*, 32(10):1250, 2007, doi:10.1364/ol.32.001250.

[60] A. Sipahigil, R. E. Evans, D. D. Sukachev, M. J. Burek, J. Borregaard, M. K. Bhaskar, C. T. Nguyen, J. L. Pacheco, H. A. Atikian, C. Meuwly, R. M. Camacho, F. Jelezko, E. Bielejec, H. Park, M. Lončar, and M. D. Lukin. An integrated diamond nanophotonics platform for quantum-optical networks. *Science*, 354(6314):847–850, 2016, doi:10.1126/science.aah6875.

[61] D. Cadeddu, J. Teissier, F. R. Braakman, N. Gregersen, P. Stepanov, J. M. Gérard, J. Claudon, R. J. Warburton, M. Poggio, and M. Munsch. A fiber-coupled quantum-dot on a photonic tip. *Applied Physics Letters*, 108(1), 2016, doi:10.1063/1.4939264.

[62] L. Vivien and L. Pavesi. Handbook of Silicon Photonics. In *Handbook of Silicon Photonics*, chapter Chapter 3:, page 851. CRC Press, 2013. doi:10.1201/b14668-4.

[63] S. Carroll and D. Goodstein. Defining the scientific method. *Nature Methods*, 6(4):237, 2009, doi:10.1038/nmeth0409-237.

[64] J. Engelhardt and W. Knebel. Konfokale Laserscanning-Mikroskopie. *Physik in unserer Zeit*, 24(2):70–78, 1993, doi:10.1002/piuz.19930240207.

[65] J. L. M. Thurner. *Durchstimmbarer Puls- und Dauerstrichlaser zur resonanten Anregung von NV-Zentren.* Bachelor thesis, Ludwig-Maximilians-Universität München, 2014.

[66] R. Hanbury Brown and R. Q. Twiss. A test of a new type of stellar interferometer on Sirius. *Nature*, 178(4541):1046–1048, 1956, doi:10.1038/1781046a0.

[67] H. J. Kimble, M. Dagenais, and L. Mandel. Photon antibunching in resonance fluorescence. *Physical Review Letters*, 39(11):691–695, 1977, doi:10.1103/PhysRevLett.39.691.

[68] C. Kurtsiefer, P. Zarda, S. Mayer, and H. Weinfurter. The breakdown flash of silicon avalanche photodiodes-back door for eavesdropper attacks? *Journal of Modern Optics*, 48(13):2039–2047, 2001, doi:10.1080/09500340108240905.

[69] J. A. Kurvits, M. Jiang, and R. Zia. Comparative analysis of imaging configurations and objectives for Fourier microscopy. *Journal of the Optical Society of America A*, 32(11):2082–2092, 2015, doi:10.1364/JOSAA.32.002082.

[70] S. Cova, M. Ghioni, A. Lacaita, C. Samori, and F. Zappa. Avalanche photodiodes and quenching circuits for single-photon detection. *Applied Optics*, 35(12):1956, 1996, doi:10.1364/ao.35.001956.

Bibliography

[71] R. G. W. Brown and M. Daniels. Characterization of silicon avalanche photodiodes for photon correlation measurements 1: Passive Quenching. *Applied Optics*, 28(21):4616, 1989, doi:10.1364/ao.28.004616.

[72] A. Golubev. Exponentially Modified Peak Functions in Biomedical Sciences and Related Disciplines. *Computational and Mathematical Methods in Medicine*, 2017, doi:10.1155/2017/7925106.

[73] M. Aßmann, F. Veit, J.-S. Tempel, T. Berstermann, H. Stolz, M. van der Poel, J. M. Hvam, and M. Bayer. Measuring the dynamics of second-order photon correlation functions inside a pulse with picosecond time resolution. *Optics Express*, 18(19):20229, 2010, doi:10.1364/oe.18.020229.

[74] S. Khasminskaya, F. Pyatkov, K. Słowik, S. Ferrari, O. Kahl, V. Kovalyuk, P. Rath, A. Vetter, F. Hennrich, M. M. Kappes, G. Gol'tsman, A. Korneev, C. Rockstuhl, R. Krupke, and W. H. P. Pernice. Fully integrated quantum photonic circuit with an electrically driven light source. *Nature Photonics*, 2(12):0–2, 2016, doi:10.1038/nphoton.2016.178.

[75] M. D. Eisaman, J. Fan, A. Migdall, and S. V. Polyakov. Invited Review Article: Single-photon sources and detectors. *Review of Scientific Instruments*, 82(7), 2011, doi:10.1063/1.3610677.

[76] I. Aharonovich, A. D. Greentree, and S. Prawer. Diamond photonics. *Nature Photonics*, 5(7):397–405, 2011, doi:10.1038/nphoton.2011.54.

[77] L. S. Pan and D. R. Kania. *Diamond: electronic properties and applications*. Springer Science & Business Media, 2013.

[78] A. M. Zaitsev. *Optical properties of diamond: a data handbook*. Springer Science & Business Media, 2013.

[79] L. C. Bassett, F. J. Heremans, C. G. Yale, B. B. Buckley, and D. D. Awschalom. Electrical tuning of single nitrogen-vacancy center optical transitions enhanced by photoinduced fields. *Physical Review Letters*, 107(26), 2011, doi:10.1103/PhysRevLett.107.266403.

[80] J. Wolters, N. Sadzak, A. W. Schell, T. Schröder, and O. Benson. Measurement of the Ultrafast Spectral Diffusion of the Optical Transition of Nitrogen Vacancy Centers in Nano-Size Diamond Using Correlation Interferometry. *Phys. Rev. Lett.*, 110(2):27401, 2013, doi:10.1103/PhysRevLett.110.027401.

[81] P. Siyushev, H. Pinto, M. Vörös, A. Gali, F. Jelezko, and J. Wrachtrup. Optically controlled switching of the charge state of a single nitrogen-vacancy center in diamond at cryogenic temperatures. *Physical Review Letters*, 110(16):1–5, 2013, doi:10.1103/PhysRevLett.110.167402.

[82] K. Beha, a. Batalov, N. B. Manson, R. Bratschitsch, and a. Leitenstorfer. Optimum photoluminescence excitation and recharging cycle of single nitrogen-vacancy centers in ultrapure diamond. *Physical Review Letters*, 109(9):97404, 2012, doi:10.1103/PhysRevLett.109.097404.

[83] M. W. Doherty, N. B. Manson, P. Delaney, F. Jelezko, J. J. J. J. Wrachtrup, and L. C. L. Hollenberg. The nitrogen-vacancy colour centre in diamond. *Physics Reports*, 528(1):1–45, 2013, doi:10.1016/j.physrep.2013.02.001.

[84] M. Berthel, O. Mollet, G. Dantelle, T. Gacoin, S. Huant, and A. Drezet. Photophysics of single nitrogen-vacancy centers in diamond nanocrystals. *Physical Review B - Condensed Matter and Materials Physics*, 91(3):1–13, 2015, doi:10.1103/PhysRevB.91.035308.

[85] N. B. Manson, J. P. Harrison, and M. J. Sellars. Nitrogen-vacancy center in diamond: Model of the electronic structure and associated dynamics. *Physical Review B - Condensed Matter and Materials Physics*, 74(10):1–13, 2006, doi:10.1103/PhysRevB.74.104303.

[86] N. Bar-Gill, L. M. Pham, A. Jarmola, D. Budker, and R. L. Walsworth. Solid-state electronic spin coherence time approaching one second. *Nature Communications*, 4, 2013, doi:10.1038/ncomms2771.

[87] T. Gaebel, M. Domhan, C. Wittmann, I. Popa, F. Jelezko, J. Rabeau, a. Greentree, S. Prawer, E. Trajkov, P. R. Hemmer, and J. Wrachtrup. Photochromism in single nitrogen-vacancy defect in diamond. *Applied Physics B: Lasers and Optics*, 82(2 SPEC. ISS.):243–246, 2006, doi:10.1007/s00340-005-2056-2.

[88] A. Batalov, V. Jacques, F. Kaiser, P. Siyushev, P. Neumann, L. J. Rogers, R. L. McMurtrie, N. B. Manson, F. Jelezko, and J. Wrachtrup. Low Temperature Studies of the Excited-State Structure of Negatively Charged Nitrogen-Vacancy Color Centers in Diamond. *Physical Review Letters*, 102(19):1–4, 2009, doi:10.1103/PhysRevLett.102.195506.

[89] B. Grotz, M. V. Hauf, M. Dankerl, B. Naydenov, S. Pezzagna, J. Meijer, F. Jelezko, J. Wrachtrup, M. Stutzmann, F. Reinhard, and J. A. Garrido. Charge state manipulation of qubits in diamond. *Nature Communications*, 3, 2012, doi:10.1038/ncomms1729.

[90] P. Ji, R. Balili, J. Beaumariage, S. Mukherjee, D. Snoke, and M. V. Dutt. Multiple-photon excitation of nitrogen vacancy centers in diamond. *Physical Review B*, 97(13):1–6, 2018, doi:10.1103/PhysRevB.97.134112.

[91] N. Aslam, G. Waldherr, P. Neumann, F. Jelezko, and J. Wrachtrup. Photo-induced ionization dynamics of the nitrogen vacancy defect in diamond investigated by single-shot charge state detection. *New Journal of Physics*, 15, 2013, doi:10.1088/1367-2630/15/1/013064.

[92] N. Nagl. *Resonante Anregung von NV-Zentren und Bestimmung von Glasfaserfluoreszenzen*. Bachelor thesis, Ludwig-Maximilians-Universität München, 2015.

[93] J. P. Goss, R. Jones, S. J. Breuer, P. R. Briddon, and S. Öberg. The twelve-line 1.682 eV luminescence center in diamond and the vacancy-silicon complex. *Physical Review Letters*, 77(14):3041–3044, 1996, doi:10.1103/PhysRevLett.77.3041.

[94] A. Sipahigil, K. D. Jahnke, L. J. Rogers, A. S. Zibrov, F. Jelezko, and M. D. Lukin. Indistinguishable photons from separated silicon vacancy centers in diamond. *Physical Review Letters*, 113(11):113602–113607, 2014, doi:10.1103/PhysRevLett.113.113602.

[95] C. Wang, C. Kurtsiefer, H. Weinfurter, and B. Burchard. Single photon emission from SiV centres in diamond produced by ion implantation. *Journal of Physics B: Atomic, Molecular and Optical Physics*, 39(1):37, 2006, doi:10.1088/0953-4075/39/1/005.

[96] L. J. Rogers, K. D. Jahnke, T. Teraji, L. Marseglia, C. Müller, B. Naydenov, H. Schauffert, C. Kranz, J. Isoya, L. P. McGuinness, and F. Jelezko. Multiple intrinsically identical single-photon emitters in the solid state. *Nature Communications*, 5:1–2, 2014, doi:10.1038/ncomms5739.

[97] U. F. S. D'Haenens-Johansson, a. M. Edmonds, B. L. Green, M. E. Newton, G. Davies, P. M. Martineau, R. U. a. Khan, and D. J. Twitchen. Optical properties of the neutral silicon split-vacancy center in diamond. *Physical Review B*, 84(24):245208, 2011, doi:10.1103/PhysRevB.84.245208.

[98] E. Neu, D. Steinmetz, J. Riedrich-Möller, S. Gsell, M. Fischer, M. Schreck, and C. Becher. Single photon emission from silicon-vacancy colour centres in chemical vapour deposition nano-diamonds on iridium. *New Journal of Physics*, 13, 2011, doi:10.1088/1367-2630/13/2/025012.

[99] E. Neu, F. Guldner, C. Arend, Y. Liang, S. Ghodbane, H. Sternschulte, D. Steinmüller-Nethl, a. Krueger, and C. Becher. Low temperature investigations and surface treatments of colloidal narrowband fluorescent nanodiamonds. *Journal of Applied Physics*, 113(20):203507, 2013, doi:10.1063/1.4807398.

[100] J. Benedikter, H. Kaupp, T. Hümmer, Y. Liang, A. Bommer, C. Becher, A. Krueger, J. M. Smith, T. W. Hänsch, and D. Hunger. Cavity-Enhanced Single-Photon Source Based on the Silicon-Vacancy Center in Diamond. *Physical Review Applied*, 7(2):1–12, 2017, doi:10.1103/PhysRevApplied.7.024031.

[101] F. Böhm. *Tieftemperaturuntersuchungen von Silizium-Fehlstellen-Farbzentren in Diamant-Nanokristallen.* Master thesis, Ludwig-Maximilians-Universtität München, 2015.

[102] L. Worthmann. *Spektroskopische Tieftemperaturuntersuchungen von Siliziumfehlstellen in Diamant.* Diplomarbeit, Ludwig-Maximilians-Universität München, 2015.

[103] E. Neu, C. Hepp, M. Hauschild, S. Gsell, M. Fischer, H. Sternschulte, D. Steinmüller-Nethl, M. Schreck, and C. Becher. Low-temperature investigations of single silicon vacancy colour centres in diamond. *New Journal of Physics*, 15(4):43005, 2013, doi:10.1088/1367-2630/15/4/043005.

[104] V. Hizhnyakov and P. Reineker. Optical dephasing in defect-rich crystals. *Journal of Chemical Physics*, 111(17):8131–8135, 1999, doi:10.1063/1.480147.

[105] G. V. Naik, V. M. Shalaev, and A. Boltasseva. Alternative plasmonic materials: Beyond gold and silver. *Advanced Materials*, 25(24):3264–3294, 2013, doi:10.1002/adma.201205076.

[106] A. Mooradian. Photoluminescence of Metals. *Physical Review Letters*, 22:185–187, 1967, doi:10.1103/PhysRevLett.22.185.

[107] A. Lalisse, G. Tessier, J. J. Plain, and G. Baffou. Quantifying the Efficiency of Plasmonic Materials for Near-Field Enhancement and Photothermal Conversion. *Journal of Physical Chemistry C*, 119(45):25518–25528, 2015, doi:10.1021/acs.jpcc.5b09294.

[108] H. J. Lezec, A. Degiron, E. Devaux, R. A. Linke, L. Martin-Moreno, F. J. Garcia-Vidal, and T. W. Ebbesen. Beaming light from a subwavelength aperture. *Science*, 297(5582):820–822, 2002, doi:10.1126/science.1071895.

[109] J. M. Yi, A. Cuche, E. Devaux, C. Genet, and T. W. Ebbesen. Beaming Visible Light with a Plasmonic Aperture Antenna. *ACS Photonics*, 1(4):365–370, 2014, doi:10.1021/ph400146n.

[110] A. Laskin and J. P. Cowin. Automated single-particle SEM/EDX analysis of submicrometer particles down to 0.1 μm. *Analytical Chemistry*, 73(5):1023–1029, 2001, doi:10.1021/ac0009604.

[111] S. J. Byrnes. Multilayer optical calculations. *ArXiv*, 16.03(02720):1–20, 2016. URL http://arxiv.org/abs/1603.02720.

[112] A. B. Djuris, J. M. Elazar, M. L. Majewski, a. D. Rakic, and a. B. Djurisic. Optical properties of metallic films for vertical-cavity optoelectronic devices. *Applied optics*, 37(22):5271–83, 1998, doi:10.1364/ao.37.005271.

[113] E. M. Purcell, H. C. Torrey, and R. Pound. Resonance Absorption by Nuclear Magnetic Moments in a Solid. *Phys. Rev*, 69(681), 1946, doi:0.1103/PhysRev.69.37.

[114] K. H. Drexhage. IV interaction of light with monomolecular dye layers. In *Progress in optics*, volume 12, pages 163–232. Elsevier, 1974. doi:10.1016/S0079-6638(08)70266-X.

[115] T. Feichtner, S. Christiansen, and B. Hecht. Mode Matching for Optical Antennas. *Physical Review Letters*, 119(21):1–6, 2017, doi:10.1103/PhysRevLett.119.217401.

[116] A. M. Smith. Polarization and magnetooptic properties of single-mode optical fiber. *Applied Optics*, 17(1):52, 1978, doi:10.1364/ao.17.000052.

[117] N. Somaschi, V. Giesz, L. De Santis, J. C. Loredo, M. P. Almeida, G. Hornecker, S. L. Portalupi, T. Grange, C. Antón, J. Demory, C. Gómez, I. Sagnes, N. D. Lanzillotti-Kimura, A. Lemaítre, A. Auffeves, A. G. White, L. Lanco, and P. Senellart. Near-optimal single-photon sources in the solid state. *Nature Photonics*, 10(5):340–345, 2016, doi:10.1038/nphoton.2016.23.

[118] J. Cui, Y. E. Panfil, S. Koley, D. Shamalia, N. Waiskopf, S. Remennik, I. Popov, M. Oded, and U. Banin. Colloidal quantum dot molecules manifesting quantum coupling at room temperature. *Nature Communications*, 10(1), 2019, doi:10.1038/s41467-019-13349-1.

[119] I. Aharonovich, D. Englund, and M. Toth. Solid-state single-photon emitters. *Nature Photonics*, 10(10):631–641, 2016, doi:10.1038/nphoton.2016.186.

[120] C. R. Benson, L. Kacenauskaite, K. L. VanDenburgh, W. Zhao, B. Qiao, T. Sadhukhan, M. Pink, J. Chen, S. Borgi, C. H. Chen, B. J. Davis, Y. C. Simon, K. Raghavachari, B. W. Laursen, and A. H. Flood. Plug-and-Play Optical Materials from Fluorescent Dyes and Macrocycles. *Chem*, 6(8):1978–1997, 2020, doi:10.1016/j.chempr.2020.06.029.

Bibliography

[121] A. Imamo, A. Imamoglu, D. D. Awschalom, G. Burkard, D. P. DiVincenzo, D. Loss, M. Sherwin, and A. Small. Quantum information processing using quantum dot spins and cavity QED. *Physical Review Letters*, 83(20):4204–4207, 1999, doi:10.1103/PhysRevLett.83.4204.

[122] A. Högele, S. Seidl, M. Kroner, K. Karrai, R. J. Warburton, B. D. Gerardot, and P. M. Petroff. Voltage-controlled optics of a quantum dot. *Physical Review Letters*, 93(21):19–22, 2004, doi:10.1103/PhysRevLett.93.217401.

[123] C. AB. Comsol Multiphysics. URL `www.comsol.com`.

[124] P. Tamarat, T. Gaebel, J. R. Rabeau, M. Khan, A. D. Greentree, H. Wilson, L. C. Hollenberg, S. Prawer, P. Hemmer, F. Jelezko, and J. Wrachtrup. Stark shift control of single optical centers in diamond. *Physical Review Letters*, 97(8):1–4, 2006, doi:10.1103/PhysRevLett.97.083002.

[125] H. Bernien, L. Childress, L. Robledo, M. Markham, D. Twitchen, and R. Hanson. Two-photon quantum interference from separate nitrogen vacancy centers in diamond. *Physical Review Letters*, 108(4):1–5, 2012, doi:10.1103/PhysRevLett.108.043604.

[126] M. Stepanova and S. Dew (eds.), M. A. Mohammad, M. Muhammad, and S. K. Dew. *Nanofabrication: Techniques and Principles*. Springer, 2012. doi:10.1007/978-3-7091-0424-8.

[127] G. Hlawacek, V. Veligura, R. V. Gastel, and B. Poelsema. Helium Ion Microscopy. *Journal of Vacuum Science & Technology B*, 32(2):020801, 2014, doi:10.1116/1.4863676.

[128] M. Horák, K. Bukvišová, V. Švarc, J. Jaskowiec, V. Křápek, and T. Šikola. Comparative study of plasmonic antennas fabricated by electron beam and focused ion beam lithography. *Scientific Reports*, 8(1):1–8, 2018, doi:10.1038/s41598-018-28037-1.

[129] A. S. Gangnaik, Y. M. Georgiev, and J. D. Holmes. New Generation Electron Beam Resists: A Review. *Chemistry of Materials*, 29(5):1898–1917, 2017, doi:10.1021/acs.chemmater.6b03483.

[130] G. H. Bernstein, D. A. Hill, and W. P. Liu. New high-contrast developers for poly(methyl methacrylate) resist. *Journal of Applied Physics*, 71(8):4066–4075, 1992, doi:10.1063/1.350831.

[131] P. Fischer. *Dielektrische Slot-Wellenleiter zur effizienten Kopplung von Diamant-Farbzentren*. Master thesis, Ludwig-Maximilians-Universität München, 2015.

[132] M. Hatzakis. PMMA Copolymers As High Sensitivity Electron Resists. *Journal of vacuum science & technology*, 16(6):1984–1988, 1979, doi:10.1116/1.570372.

[133] Y. K. Hong, H. Kim, G. Lee, W. Kim, J. I. Park, J. Cheon, and J. Y. Koo. Controlled two-dimensional distribution of nanoparticles by spin-coating method. *Applied Physics Letters*, 80(5):844–846, 2002, doi:10.1063/1.1445811.

[134] K. E. Schmalenberg, H. M. Buettner, and K. E. Uhrich. Microcontact printing of proteins on oxygen plasma-activated poly(methyl methacrylate). *Biomaterials*, 25(10):1851–1857, 2004, doi:10.1016/j.biomaterials.2003.08.048.

[135] H.-U. Poll, M. Zeuner, and J. Meichsner. Oxidative decomposition of polymethyl-methacrylate (PMMA) in plasma etching. *Plasma Sources Science and Technology*, 4(3):406–415, 1995, doi:10.1088/0963-0252/4/3/010.

[136] A. W. Schell, G. Kewes, T. Schröder, J. Wolters, T. Aichele, and O. Benson. A scanning probe-based pick-and-place procedure for assembly of integrated quantum optical hybrid devices. *Review of Scientific Instruments*, 82(7), 2011, doi:10.1063/1.3615629.

[137] P. Eaton and P. West. *Atomic force microscopy*. Oxford University Press, 2010.

[138] F. W. Delrio, M. P. De Boer, J. A. Knapp, E. D. Reedy, P. J. Clews, and M. L. Dunn. The role of van der Waals forces in adhesion of micromachined surfaces. *Nature Materials*, 4(8):629–634, 2005, doi:10.1038/nmat1431.

[139] A. von Münchow. *Das Rasterkraftmikroskop als Werkzeug zur Nanomanipulation von fluoreszierenden Nanodiamantkristallen*. Bachelor thesis, Ludwig-Maximilians-Universität München, 2013.

[140] N. Nikolay, N. Sadzak, A. Dohms, B. Lubotzky, H. Abudayyeh, R. Rapaport, and O. Benson. Accurate placement of single nanoparticles on opaque conductive structures. *Applied Physics Letters*, 113(11), 2018, doi:10.1063/1.5049082.

[141] A. Tafazzoli and M. Sitti. Dynamic behaviour and simulation of nanoparticle sliding during nanoprobe-based positioning. *Proceedings of IMECE'04 2004 ASME International Mechanical Engineering Congress*, pages 1–8, 2004, doi:10.1115/IMECE2004-62470.

[142] S. Akamine, R. C. Barrett, and C. F. Quate. Improved atomic force microscope images using microcantilevers with sharp tips. *Applied Physics Letters*, 57(3):316–318, 1990, doi:10.1063/1.103677.

Science is not only a disciple of reason, but also one of romance and passion.

(Stephen Hawking)

Danksagung

Zum Schluss der Arbeit soll natürlich auch jenen gedankt werden, die an deren Entstehung mitgewirkt haben, sei es direkt als Kollegin oder Kollege in der Arbeitsgruppe oder indirekt durch Motivation oder Freizeitgestaltung während der Promotionszeit.

Zuallererst danke ich Harald Weinfurter für die Möglichkeit, das Projekt in seiner Arbeitsgruppe durchzuführen und für die Unterstützung während dieser. Auch für die große Freiheit, eigene Ideen umsetzen zu können, sei gedankt. Dank geht auch an Markus Weber, der zu Beginn der Arbeit das Projekt leitete und mich mit seiner unkonventionellen Art in die Welt der Diamanten und Wellenleiter einführte. An dieser Stelle möchte ich mich auch besonders bei Lars Liebermeister bedanken, der als Vorgänger am Diamantprojekt arbeitete und so bereits viele Ansätze und Bausteine auch für diese Arbeit entwickelte und realisierte.

Essentiell für das Gelingen einer Promotion ist der Austausch mit anderen Personen innerhalb der Gruppe, wodurch andere Blickwinkel auf Fragestellungen, seien es physikalische oder anderweitige, geworfen werden können und generell das Arbeiten mit Leben gefüllt wird. Aus dem Atom-Experiment waren dies insbesondere Wenjamin Rosenfeld, Norbert Ortegel, Daniel Burchardt, Kai Redeker, Robert Garthoff, Tim van Leent, Wei Zhang, die QKD-Leute Markus Rau, Gwenaelle Vest, Peter Freiwang, Leonhard Mayr, Rengaraj Aparajithan, Adomas Baliuka, die Garchinger Christian Schwemmer, Lukas Knips, Jan Dziewior, Jasmin Meinecke und - außer Konkurrenz laufend - Daniel Schlenk. Hinzu kommen die Masterstudenten Florian Böhm, Peter Fischer, Lukas Worthmann sowie die Bachelorstudenten Johannes Thurner, Nathalie Nagl, Maximilian Göppel, Michael Lichtenegger, Florian Fertig und Nils Hellerhoff, die im Laufe der Jahre mit viel Eifer und Einsatz am Diamantprojekt mitgewirkt haben.

Besonders bedanken möchte ich mich bei Philipp Altpeter für seinen großen Einsatz und seine fachliche Kompetenz in allen Fabrikationsfragen, ohne die die vorliegende Arbeit in dieser Form nicht möglich gewesen wäre. Dank auch an Peter Weiser für seine steten Bemühungen, die Fabrikationsanlagen in Garching trotz hoher Auslastung am Laufen zu halten. Für alle administrativen und sonstigen Arbeiten, die oftmals sehr offensiv angegangen werden, danke ich Gabriele Gschwendtner. Weiterhin möchte ich Nicole Schmidt und Anton Scheich für die Unterstützung am Lehrstuhl danken.

Ein Dank geht auch an alle (ehemaligen) Kommilitonen an der TUM, die schnell zu Freunden wurden, insbesondere Nico, Peter, Andreas, Matthias, Tobi und Franz. Auch wenn wir uns im Laufe der Jahre verstreut haben, hatte uns doch das Interesse an Physik erst zusammengebracht.

Für die stete Unterstützung während der Studien- und Promotionszeit bedanke ich mich herzlichst bei meiner Familie und bei Johanna, die mit viel Verständnis vor allem die Schreibzeit so viel einfacher und schöner gemacht hat.

Final sei noch gesagt: Die Promotionszeit ist eine ganz besondere Zeit, die erst mit den richtigen Leuten Spaß macht. Dafür Danke!